Effects of Dopant Additions on the High Temperature Oxidation Behavior of Nickel-based Alumina-forming Alloys

by

Talia L. Barth

A dissertation submitted in partial fulfillment
of the requirements for the degree of
Doctor of Philosophy
(Materials Science and Engineering)
in the University of Michigan
2020

Doctoral Committee:

Professor Emmanuelle Marquis, Chair
Assistant Professor John Heron
Professor Krishna Garikipati
Professor Alan Taub

Talia L. Barth

tlbarth@umich.edu

ORCID iD: 0000-0001-8266-7447

ACKNOWLEDGEMENTS

I would like to first offer my heartfelt thanks to my advisor, Professor Emmanuelle Marquis, without whom this work would not have been possible. Her exceptional mentorship has had an immense impact on my development as a researcher and a person, and her support and guidance along my journey have been invaluable.

I would also like to express my appreciation for the rest of my committee, Professor Alan Taub, Assistant Professor John Heron, and Professor Krishna Garikipati for providing valuable advice and support for the completion of this work.

I am grateful to the staff at the Michigan Center for Materials Characterization (MC)2, especially to Allen Hunter, Bobby Kerns, Haiping Sun, and Nancy Muyanja whose training enabled me to work confidently on the characterization instruments essential to this dissertation, and were always eager to lend their expertise with data collection and analysis.

My colleagues in the Marquis group over the years were also important to this work and to my professional and personal development. I would like to thank Kevin Fisher, Ellen Solomon, Elaina Reese, and Peng-Wei Chu for getting me up to speed in the lab and for being there as mentors and friends in my first years as a grad student. Many thanks also to Li-Jen Yu and Kathleen Chou, whose support and friendship were invaluable as we pursued our Ph.Ds together.

Finally, a very special thanks to my friends and family, whose support enabled me to push through the toughest challenges over the years. To all of the friends I’ve connected with playing ultimate, I am so glad to be a part of such an amazing community, and feel lucky to have

met some of my best friends here in Michigan. My parents, Kathleen and Matthew Barth, have given me endless encouragement and support in all that I choose to do, and for that I am forever grateful. I would also like to thank my brother, Trevor, whose friendship means the world to me. Lastly, I must thank Eric, who remained a constant source of positivity and was there for me during the most difficult parts of the last couple years. I feel very lucky to have you in my life. For all of these people, and more who influenced me along the way, thank you.

TABLE OF CONTENTS

LIST OF TABLES

LIST OF FIGURES

LIST OF APPENDICES

ABSTRACT

Nickel-based alloys continue to play a crucial role for high temperature applications due to their excellent mechanical properties. Despite their high strength, toughness, and creep resistance, these alloys are vulnerable to aggressive oxidation and corrosion upon exposure to air at high temperature, limiting their application space. To promote oxidation resistance, nickel is typically alloyed with aluminum, which enables the formation of a stable, continuous layer of Al_2O_3 on the alloy surface. A protective Al_2O_3 layer should develop quickly and then grow slowly at temperature to effectively limit metal loss. Minor alloying elements additions are well-known to reduce Al_2O_3 scale growth rate. Even small reductions in the growth rate can make a substantial difference in extending the lifetime of a high temperature component. Yet many of the mechanisms by which dopants reduce oxidation rate remain unclear.

To develop accurate predictive models of oxidation rate and design highly oxidation resistant alloys for a range of applications, an understanding of the fundamental effects of dopants on oxidation is critical. The current work aims to elucidate the mechanisms by which common dopants, known to improve oxidation resistance of commercial alloys, modify α-Al_2O_3 growth. Model NiAl and NiCrAl alloys doped with Ti, Y, and Si were oxidized at temperatures from 950-1200 °C, and high-resolution characterization techniques were used to probe the resulting alumina scale microstructure and chemistry. In particular, the effects of minor alloying additions on alumina scale development in the early stages of oxidation and Al/O transport through an established alumina scale after longer exposures were investigated.

During the early stages of alumina scale development, metastable Al_2O_3 phases form first and grow quickly before transforming to α-Al_2O_3 via a nucleation and growth process. Y additions did not significantly change the transformation rate, while Si and Ti additions were found to accelerate the overall transformation to α-Al_2O_3 on NiAl by different mechanisms. The addition of Ti decreased the incubation time for nucleation of α-Al_2O_3, while Si additions accelerated the metastable to α-Al_2O_3 transformation rate. These findings can inform the development of alloys that quickly form protective α-Al_2O_3 even at moderate (~800-1000 °C) temperatures, where rapid metastable Al_2O_3 growth can quickly degrade thin-walled components.

Once a fully α-Al_2O_3 scale is formed, dopants affect the transport of Al and O along the α-Al_2O_3 grain boundaries, thus altering the α-Al_2O_3 growth rate. Ti, Y, and Si had different impacts on the individual magnitudes of Al and O fluxes through the scale, resulting in different oxidation rates. Differences in Al and O fluxes can also affect the evolution of α-Al_2O_3 scale microstructure, that can then impact other aspects of scale growth such as stress development. Accordingly, the new knowledge gained from this work can be used to design alloys that not only have very slow oxidation rates, but develop more adherent scales and longer lifetimes.

Through its systematic approach, this work examined specific aspects of the complex oxidation process and clarified the mechanisms by which different dopant elements can affect scale growth. This new information can be used for targeted alloy design and modelling of scale growth processes.

CHAPTER 1:

Introduction

1.1 Background and Motivation

The environmental degradation of metals is a widespread and costly problem that affects many different sectors. Structural metals used in transportation and energy applications are often subject to extreme environmental conditions that can negate the properties for which they were selected. Nickel-based alloys, for example, are used for their superior mechanical properties even at temperatures exceeding 800 °C [1]. Despite their excellent strength and creep resistance at elevated temperatures, nickel alloys are vulnerable to environmental attack. Rapid oxidation may occur as components are heated in air, and can quickly degrade the alloy [2]. To protect against rapid degradation, nickel is typically alloyed with aluminum, which promotes the formation of a slow-growing protective Al_2O_3 layer, or “scale”, on the alloy surface [3]. Al_2O_3 grows much more slowly than other reaction products such as nickel oxide [4], thus dramatically reducing the loss of metal over time. It is also critical that the protective alumina layer be adherent to the underlying alloy, since repeated breaking off of the oxide, or “spalling”, can lead to depletion and degradation of the alloy [5]. Even marginal reductions of the oxidation rate and increases in scale adherence can significantly prolong the useful lifetime of a nickel-based component at high temperature.

A well-known means of improving the oxidation behavior of Al_2O_3 scales is through the addition of minor alloying elements. Termed the “reactive element (RE) effect”, adding small amounts of elements such as Y, Zr, and Hf, among others, both reduces Al_2O_3 scale growth rate and increases adherence. Thus, the RE effect has been the subject of extensive study over the past 60 years or so, and several reviews are available to encompass much of this work [6-9].

Despite the abundance of research, many open questions remain as to the mechanisms by which dopant elements produce such beneficial effects on oxidation behavior. Oxidation is a complex process, often involving multiple phases, transport processes, and interactions with impurities. Dopant additions can affect many separate aspects of scale growth. In addition, the numerous element additions present in commercial alloys such as nickel superalloys make it difficult to isolate the effects of individual elements. Though prior work has shed some light on how dopant additions alter oxidation behavior, the community is still far from being able to develop accurate predictive models of oxidation behavior of various alloys. Specifically, further mechanistic understanding of the effects of alloy composition on oxide formation, growth, and adherence is needed for the design of extremely oxidation resistant alloys and lifetime prediction of protective scales. Both of which are critical for industrial applications.

This work aims to clarify some of the mechanisms by which different dopant elements affect the development and growth behavior of alumina scales on nickel-based alloys. Model alloys with additions of one or two dopant elements were used to isolate the effects of individual elements on oxidation. A focus was placed on testing dopant effects on two central aspects of alumina scale growth: transient scale development and steady-state scale transport. Multiple characterization techniques were used to probe alumina microstructure and chemistry from the macro to atomic scale in order to investigate the mechanisms of dopant effects on oxidation.

1.2 Thesis Structure

Following this introduction, Chapter 2 provides a review of various aspects of high temperature oxidation related to alumina scales, including transient oxidation, steady-state oxidation, stress development, and dopant effects on each of these areas. Open questions remaining in the field are also addressed. Chapter 3 focuses on clarifying the role of Ti, Si, and Y additions in the transient stage of oxidation, specifically on the alumina phase transformations that take place as the alumina scale develops on NiAl alloys. Chapter 4 examines the effects of Ti and Y additions on transport through the alumina scale during steady-state oxidation of NiAl. Chapter 5 explores the effect of Ti-doping on oxidation of a more complex NiCrAl alloy, which forms a multi-phase oxide scale. Finally, Chapter 6 presents the main conclusions of this work, as well as recommendations for future research.

CHAPTER 2:

Literature Review

2.1 Overview

The key characteristics of a protective surface oxide are its stability, growth rate, and adherence to the underlying alloy. The oxide phase should be highly stable, enabling a dense, continuous layer to form on the alloy surface. Once formed, the oxide scale should grow slowly, minimizing the reaction of the metal with its environment. Stress-induced spallation may also occur, thus understanding stress development in the scale and its adherence to the alloy surface is of importance. To develop practical strategies for oxidation protection, the fundamental parameters governing oxide stability, growth rate, and adherence must be considered.

This review aims to summarize our existing understanding of the effects of dopant elements on various aspects of alumina scale development and growth on Ni-alloys, while taking into account the key characteristics of protective scales. Prior literature demonstrates that dopant additions affect many of the different aspects of oxidation, including the early stages of scale formation, steady-state scale microstructure and transport, and stress development. Commercial high temperature alloys are typically Fe- or Ni-based, and may have dozens of alloying additions that lead to multi-phase oxide scales. This presents a challenge when describing the effects of a single minor alloying element. To consider the relevant mechanisms for dopant effects on alumina development and growth, this work focuses on the oxidation of NiAl alloys, which readily form a single layer of protective alumina rather than a multi-phase scale, in air at temperatures typically encountered in industrial settings, ranging from 900-1200 °C. Finally, knowledge gaps will be discussed and will give context for the research questions addressed in this dissertation.

2.1.1 Oxide Phase Stability

Generally, the oxide phases that form on a metal surface are governed by their thermodynamic stability. The standard free energy of formation of the oxide phase (ΔG°) is a measure of the driving force for the reaction between metal and oxygen to occur. It is linked to the partial pressure of gaseous oxygen, by

$$\Delta G^{\circ} = RTlnp_{O_2} \tag{1}$$

Negative values of ΔG° indicate that a reaction can proceed spontaneously, and the more negative the value, the higher the driving force for the reaction [10]. Because ΔG° depends on both temperature and oxygen partial pressure, values of ΔG° for metal oxidation reactions are plotted against temperature in so-called "Ellingham diagrams" [11] (**Figure 2.1**). Ellingham diagrams provide a comparison of the relative stabilities of various oxides, and express the oxygen partial pressure at which the metal and oxide coexist at equilibrium. When a dense oxide scale on the alloy surface is able to establish a gradient of oxygen pressure, a multi-phase layered scale may develop, with the most stable oxides forming closest to the metal where the oxygen partial pressure is lowest and the least stable oxides forming closer to the surface where oxygen partial pressure is highest. For Al-containing alloys, Al_2O_3 is one of the most stable metal oxides, with a low value of ΔG° (**Figure 2.1**). When Al is not present in an alloy, other stable oxides, such as Cr_2O_3 or SiO_2, may also form a protective scale on the alloy surface.

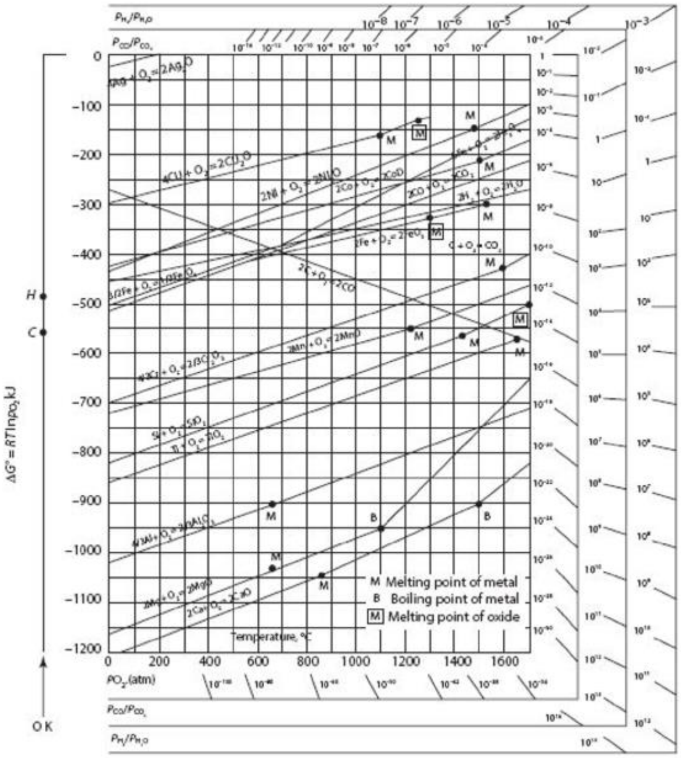

Figure 2.1: An Ellingham diagram showing the relative stability of selected oxide phases. Republished with permission of Taylor & Francis Group LLC – Books, from [12]; permission conveyed through Copyright Clearance Center, Inc.

2.1.2 Oxide Growth Rate

In addition to being highly stable oxide phases, Al_2O_3, Cr_2O_3, and SiO_2 have slow growth rates compared to many other oxides, minimizing degradation of the alloy. A comparison of the oxidation rate constants for several common oxide phases is shown in **Figure 2.2** [4]**.** SiO_2 and Cr_2O_3, though slow-growing and thermodynamically stable, tend to be limited to lower temperature use. SiO_2 reduces to SiO, which is highly volatile [13], and also may react with the metal to form detrimental molten phases [14, 15]. Cr_2O_3 is useful in corrosion protection, and is a common element in stainless steels as well as coatings that form multi-layered scales, but can be volatile at temperatures above 1000 °C as the scale oxidizes to form CrO_3 [16, 17]. Al_2O_3 is one of the most stable oxides even at high temperature, and has one of the slowest growth rates, thus limiting alloy degradation when formed as a continuous layer even in the presence of other oxides.

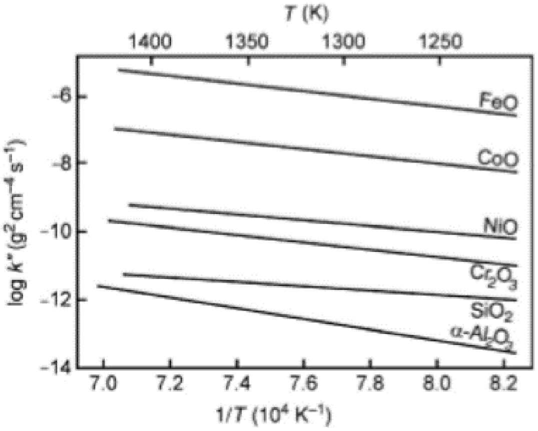

Figure 2.2: Arrhenius diagram for the parabolic growth rate constants of several common oxide phases [4]. Reproduced with permission of Cambridge University Press through PLSclear.

The growth rate of an oxide scale is typically controlled by the diffusion of oxygen and/or metal ions through the scale. The rate is limited by the faster of the diffusing species, and can described using parabolic kinetics:

$$x^2 = 2k_pt \tag{2}$$

where x is the scale thickness, k_p is the parabolic rate constant, and t is the oxidation time. This parabolic rate law holds true for steady-state oxide growth assuming that the oxide scale is compact (no large pores and well-adhered to the metal), the scale-gas and scale-metal interface are at thermodynamic equilibrium, and the flux of ions/ electrons is constant throughout the scale (i.e. the oxide is close to stoichiometric). Details of its derivation can be found elsewhere [4, 18].

Oxidation may deviate from parabolic kinetics when diffusion through the scale is not the rate-limiting step. For example, the oxidation rate exhibits a linear dependence with time when interface processes are slow relative to the diffusion through the scale. This may occur in a dilute gas at high temperature, when oxygen adsorption at the surface is slow compared to diffusion through the scale, or when the oxide is highly porous or cracked and oxygen reaches the metal through gas transfer [18]. Linear oxidation kinetics may occur at high temperature when the oxide layer is very thin, such as in the initial stages of oxidation [19]. Sub-parabolic or cubic kinetics have been observed in some cases on scales which have short-circuit diffusion paths such as grain boundaries [20].

For most dense oxide scales, parabolic kinetics are a fitting description, and the parabolic rate constant is commonly used as a way of comparing the high temperature oxidation behavior of different alloys and oxide phases (**Figure 2.2**). Typical experiments to measure the oxidation rate constant involve recording the weight gain of a sample over time at a given temperature while exposed to air. The sample weight increases over time as a consequence of oxygen reacting with the metal to form a surface oxide. If one assumes that there is no dissolution of oxygen into the metal, no loss of the oxide to form volatile species, and all spalled oxide is included in the measurements, then the recorded weight gain is directly proportional to oxide thickness. Thus, the parabolic rate constant is usually calculated from the weight gain data over time. This is commonly done by plotting the weight gain (normalized to the metal surface area) against the (oxidation time)$^{1/2}$, and the slope of the fitted line is taken as the parabolic rate constant, k_p [21].

2.1.3 Oxide Stress Development and Adherence

Mechanical aspects of scale growth are also important for maintaining the protective scale on the alloy surface. Stresses may be generated in protective scales due to growth processes during isothermal oxidation, and due to thermal mismatch of the oxide and metal when the scale goes through significant temperature variation [4], commonly encountered during industrial heating and cooling cycles. These stresses may exceed the fracture strength of the oxide or the interfacial strength, leading to cracking and decohesion from the metal [22]. Repeated spallation enhances metal loss as a new oxide scale must form each time, and can deplete the metal of the primary oxidizing element, such as Al in the case of Al_2O_3 scales [5]. Thus, mitigating stress generation, enabling stress relief mechanisms, and high scale-alloy interface cohesion are important for maintaining an intact protective scale on the alloy surface.

In summary, the stability, growth rate, and mechanical aspects of oxides can be useful for qualitative predictions of steady-state oxidation behavior, but do not provide a complete picture of oxidation behavior. In many cases, kinetic processes involved in oxide formation and microstructure evolution also play a significant role. Using these principles as a framework for considering the protective properties of an oxide scale, further aspects of scale development and growth are now discussed.

2.2 Transient Oxidation of Alumina-forming Alloys

2.2.1 Alumina Metastable Phases and Transformation to α-Al_2O_3

At the earliest stages of oxidation, the oxide phases that first form are not always the most thermodynamically stable. These transient oxide phases can be highly dependent on alloy composition and oxidation conditions. Often, phases that form initially are those with compositions close to the base alloy. On NiCrAl alloys, for example, NiO and $Ni(Cr,Al)_2O_4$ tend to form first, before a continuous layer of Al_2O_3 or Cr_2O_3 eventually develops at the scale-alloy interface [3, 23, 24]. For alumina-forming alloys, several alumina polymorphs, most commonly γ-Al_2O_3 and θ-Al_2O_3, have been observed to form during oxidation at temperatures ranging from 600-1200 °C before transforming into the stable α-Al_2O_3 [25-30].

The metastable Al_2O_3 phases are stoichiometrically similar to α-Al_2O_3, but have different crystal structures, densities, and growth mechanisms than α-Al_2O_3. Many of the metastable Al_2O_3 phase crystal structures have been characterized in detail in the context of ceramics processing and catalysts, and a comprehensive review from Levin *et al.* [31] is available. In general, the metastable Al_2O_3 structures are similar to α-Al_2O_3 in that they exhibit a close-packed oxygen sublattice with aluminum cations in the interstitial sites. However, the oxygen sublattice symmetry, as well as the distribution and degree of ordering of the Al cations in the octahedral and tetrahedral interstitial sites of the oxygen lattice, differentiate the various alumina phases. γ-Al_2O_3 consists of a FCC packed oxygen sublattice and can be described as a defect spinel structure with Al cation vacancies [31-33]. Diffuse TEM diffraction spots suggested that the cation sublattice of γ-Al_2O_3 is highly disordered [34, 35]. Reports of the cation site occupancy of γ-Al_2O_3 varied, with different studies measuring anywhere from 40-75% of cations in the octahedral interstitial sites of the oxygen sublattice [32, 35-37]. The θ-Al_2O_3 phase exhibits a FCC packed oxygen sublattice with monoclinic symmetry [31, 36]. The Al cations in θ-Al_2O_3 are distributed evenly between the octahedral and tetrahedral interstitial sites, with 50% in octahedral sites [36]. Finally, the stable α-Al_2O_3 phase has a hexagonal close packed oxygen sublattice with trigonal symmetry (**Figure 2.3**) [31, 38]. All Al cations in α-Al_2O_3 are in the octahedral interstitial sites, with 2/3 of the octahedral sites filled.

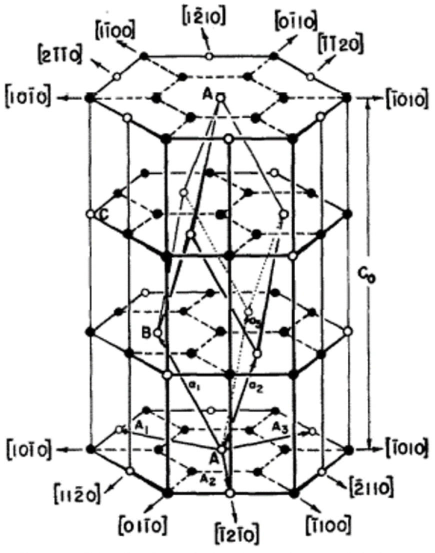

Figure 2.3: Structural representations of aluminum and oxygen ions in α-Al_2O_3. Filled circles represent Al ions while open circles represent Al vacancies on the hexagonal lattice. The rhombohedral unit cell is shown within the hexagonal cell, with corresponding hexagonal cell directions. Reprinted from [38], with permission from Elsevier.

The transition to α-Al_2O_3 may proceed through several intermediate metastable phases. During the synthesis of α-Al_2O_3 from heating a gel or powder precursor (commonly boehmite), typical phase transition sequences were reported to progress from γ → δ → θ → α [31]. It is generally agreed that the transition from the cubic γ-Al_2O_3 to θ-Al_2O_3 (including additional intermediate phases such as δ in some cases) occurs by cation redistribution, while the close-packed oxygen sublattice is nearly unaffected [31, 35, 39-41]. In electron diffraction patterns of the different alumina phases, reflections resulting from the oxygen sublattice remained approximately unchanged during the phase transformations, while changes occurred in the reflections that were associated with the cation sublattice [39]. The Al ions gradually transition from distributions across both octahedral and tetrahedral sites to increasing occupation of the octahedral sites [41, 42]. Thus, lattice rearrangement of Al ions takes place during the metastable phase transitions [41]. To transform from the metastable phases to α-Al_2O_3, both Al and O rearrangement must take place.

The rearrangement of Al and O during the transition from γ and θ to α-Al_2O_3 has been suggested to occur through two possible mechanisms, either a diffusion-less "synchro-shear" process or a nucleation and growth process. In the "synchro-shear" case, oxygen layers concurrently shear to transition from cubic to hexagonal packing, and aluminum ions located near the sheared layer rearrange by jumping into octahedral sites [43, 44]. Alternatively, the transformation to α-Al_2O_3 has been reported to take place by a classical nucleation and growth mechanism [45, 46]. It was suggested that α-Al_2O_3 nucleates in regions rich in anionic/cationic vacancies, and grows as vacancies continue to diffuse to the transformation front and go through an annihilation reaction, leading to structural rearrangement [47]. Bagwell *et al.* [48] critically discussed evidence in support of both the synchro-shear and nucleation/diffusion mechanisms and concluded that diffusional nucleation is more likely to occur. In their view, the common observation that seeding transition alumina with α-Al_2O_3 particles accelerates the transformation to α-Al_2O_3 [45, 49, 50] provides evidence that heterogeneous nucleation and subsequent diffusion is taking place during the transformation. The crystal structures and transformation mechanisms documented in bulk Al_2O_3 provide a basis for discussing alumina transformation in the context of thermally grown alumina scales.

2.2.2 Metastable Alumina Formation during Thermal Oxidation of NiAl

During thermal oxidation of β-NiAl alloys, which form exclusive alumina scales, a layer of sub-microcrystalline metastable alumina tends to form in the earliest stages of oxidation. Of the various metastable alumina phases, both γ-Al_2O_3 [25-27] and θ-Al_2O_3 [26-30, 51, 52] have been reported to form at short oxidation times. Hindam *et al.* [53] observed a thin layer of γ-Al_2O_3 after 5 minutes of oxidation at 1000 °C, as did Yang *et al.* [25], who identified a layer of

γ-Al_2O_3 after 50 hours of oxidation at 950 °C. θ-Al_2O_3 was observed by Doychak *et al.* [54] to form after 10 hours of oxidation at 800 °C, and after 6 minutes at 1100 °C. After oxidation for 100 hours at various temperatures, Rybicki *et al.* [30] identified a layer of θ-Al_2O_3 by XRD at 800 °C and 900 °C. Rommerskirchen *et al.* [52] observed the θ-Al_2O_3 phase up to 40 hours of oxidation at 950 °C and up to 5 hours at 1000 °C. The θ-α transformation can be usefully visualized on a time-temperature transformation (TTT) plot [51], highlighting the thermally activated process by which θ-Al_2O_3 takes longer to transform completely to the α phase at the lower temperatures (**Figure 2.4**). Regardless of the exact phase, it has been widely reported that metastable alumina layers form at lower temperatures, short oxidation times, and tend to grow with a blade/ platelet surface morphology (**Figure 2.5**) [27, 28, 30, 54, 55]. Epitaxial relationships between the transition alumina layer and NiAl alloy have also been reported. The classical Bain relationship has been observed between β-NiAl and γ-Al_2O_3, with [100] NiAl parallel to [110] γ-Al_2O_3 [25]. Doychak *et al.* [54] also observed the Bain orientation relationship between θ-Al_2O_3 and the metal on (001) single-crystal β-NiAl, but found several other orientation relationships on different NiAl substrate orientations. The metastable alumina layers grow by outward aluminum transport [51, 56, 57] and with significantly faster oxidation kinetics than α-Al_2O_3; the oxidation rate constants of γ and θ alumina are about two orders of magnitude larger than that of α-Al_2O_3 (**Figure 2.6**) [27, 30]. It is thought that the rapid outward diffusion of aluminum leads to the blade/platelet morphology commonly associated with the metastable alumina phases [54].

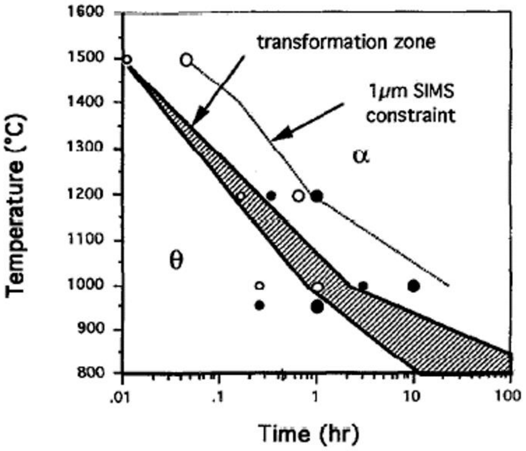

Figure 2.4: Approximate time-temperature dependence of the θ- to α-Al_2O_3 transformation on β-NiAl. The filled area represents the existence of both θ- and α-Al_2O_3. Reprinted from [51], with permission from Elsevier.

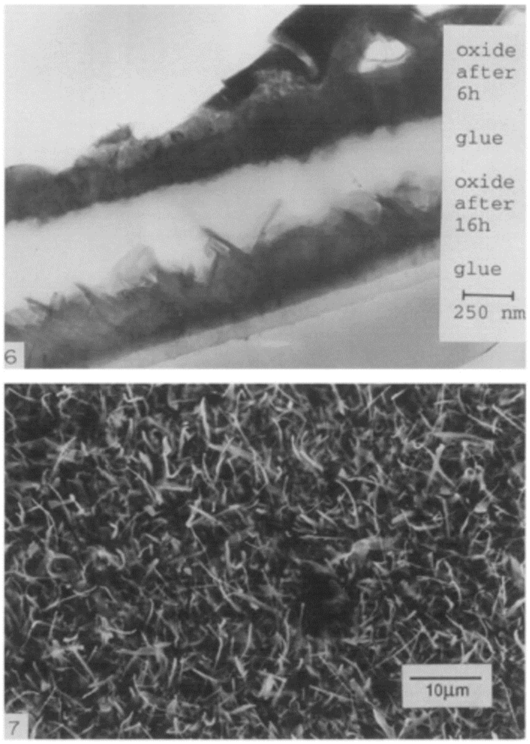

Figure 2.5: a) TEM image of a cross section of the oxide layers on Ni-50Al after oxidation at 1173K for 6h (upper layer) and 16h (lower layer). B) SEM image of the oxide surface on Ni-50Al after oxidation at 1223K for 60h showing whisker morphology. Reprinted from [27], with permission from Elsevier.

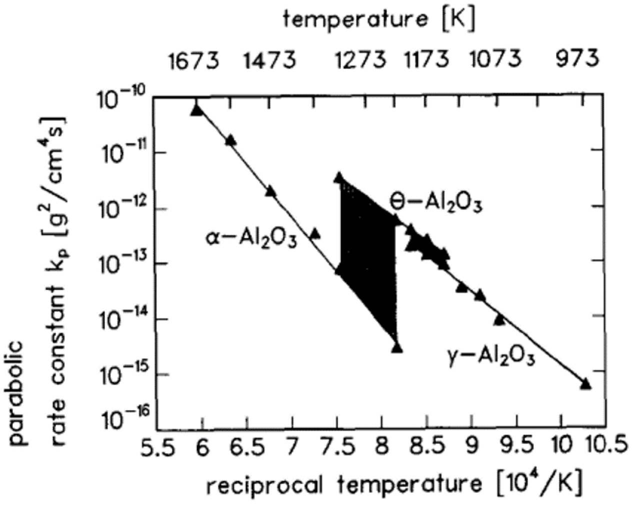

Figure 2.6: Arrhenius plot of the parabolic rate constants for the oxidation of NiAl at various temperatures. The different rates correspond to different phases of Al_2O_3. The shaded region represents temperatures for which both θ and α-Al_2O_3 were present. Reprinted from [27], with permission from Elsevier.

At higher temperatures and longer oxidation times, the metastable alumina layer eventually transforms into the stable, slow-growing α-Al_2O_3 phase, which is associated with a significant reduction in the oxidation kinetics (**Figure 2.7**) [27, 30, 58]. Though early studies [27, 59], concluded that α-Al_2O_3 nucleates at the scale-gas surface, the planar TEM technique used was such that the electron beam went through the thickness of the oxide, making it difficult to identify where different oxide phases were located in depth. Using a cross-section imaging approach instead, Doychak *et al.* [60] confirmed that α-Al_2O_3 nucleated at the free surface. Contradicting these results, later studies identified α-Al_2O_3 nucleation sites at the scale-alloy interface. Yang *et al.* [55], using cross-section TEM imaging, found that while the metastable alumina layer exhibited an epitaxial relationship with the NiAl metal, new α-Al_2O_3 grains nucleated at the scale-alloy interface with random orientation (**Figure 2.8**). However, it is possible that the TEM image was not representative of all nucleation events, so nucleation at other locations such as the free surface could not be discounted. Hou *et al.* [61], using fracture sections and synchrotron X-ray diffraction, found that θ-Al_2O_3 formed multiple layers in the initial stages of oxidation, and that α-Al_2O_3 was found only in the layer near the scale-alloy interface (**Figure 2.9**). Based on this result, it was concluded that α-Al_2O_3 nucleated at the scale-alloy interface, yet it is still not clear if α-Al_2O_3 nucleated at the alloy or some other region in this layer. Often citing Yang *et al.* [55] and Hou *et al.* [61], subsequent studies generally assumed that α-Al_2O_3 first nucleates at the scale-alloy interface.

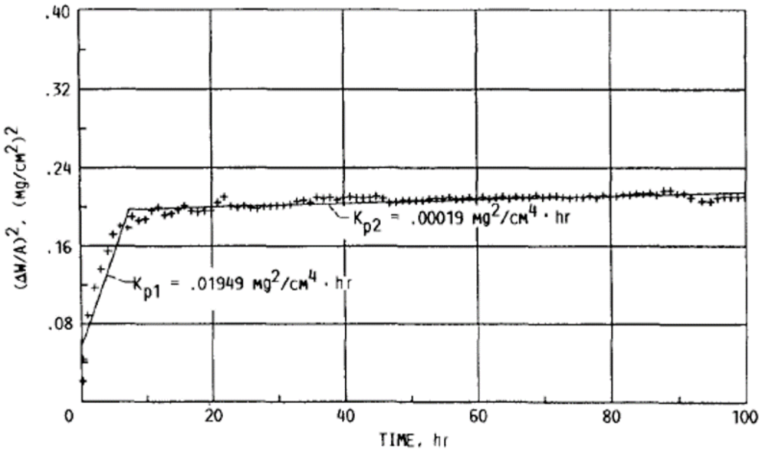

Figure 2.7: (Weight gain)^2 versus time plot showing the transition in oxidation kinetics for a NiAl+Zr alloy at 1000 °C. Reprinted by permission from Springer Nature: Oxidation of Metals [30].

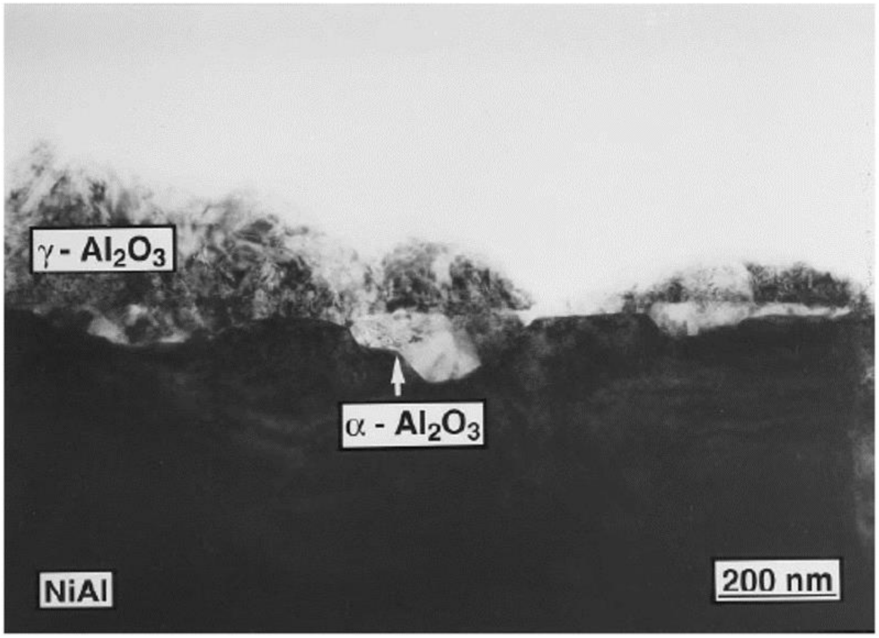

Figure 2.8: Cross-sectional TEM image of the oxide scale on NiAl after 50h of oxidation at 950 °C. Randomly oriented α-Al_2O_3 grains were observed at the oxide-NiAl interface. Reprinted from [55], with permission from Elsevier.

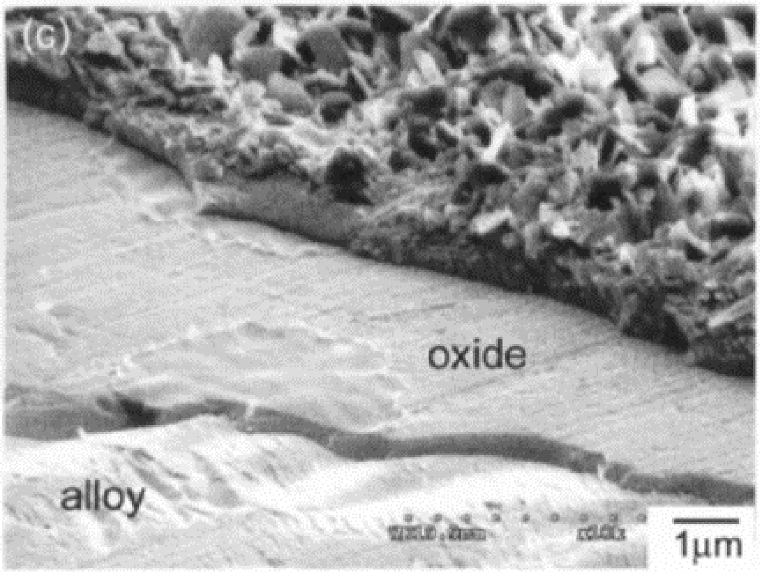

Figure 2.9: SEM image of a fractured Al2O3 scale cross-section. The scale consists mostly of multi-layered θ-Al_2O_3, and α-Al_2O_3 patches can be seen in the inner oxide layer. Reprinted from [61].

Once nucleated, the α-Al_2O_3 grows laterally through the metastable layer, forming circular “patches” or “islands” (**Figure 2.10**) [30]. The α-Al_2O_3 patches continue to grow laterally until they impinge, covering the entire surface [27, 30, 58]. Since the metastable alumina has a lower density than the α-Al_2O_3 phase (about 3.6 and 4 g/cm^3 respectively [31]), a volume shrinkage of about 8% takes place during phase transformation. Consequently, radial cracks form at the center of the α-Al_2O_3 patches [28, 30, 58, 59, 62], due to tensile stress generated by the volume shrinkage [28, 61]. Lipkin *et al.* [29] measured the evolution of α-Al_2O_3 patch radii on (111) single crystal NiAl at 1100 °C using photoluminescence in conjunction with SEM images, and found that the lateral growth rate of α-Al_2O_3 had a logarithmic dependence on oxidation time (**Figure 2.11**). The authors speculated that logarithmic kinetics, instead of the expected linear growth kinetics for an interface-controlled transformation, likely arose from interface pinning due to voids formed from volume change at the transformation front.

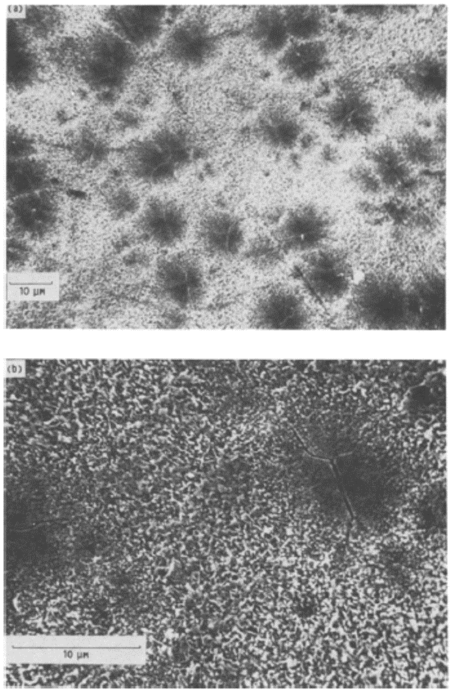

Figure 2.10: SEM images of circular patches of α-Al_2O_3 in a layer of θ-Al_2O_3. a) Low-magnification overview. b) Higher magnification showing cracks in the α-Al_2O_3 patches. Reprinted by permission from Springer Nature: [30].

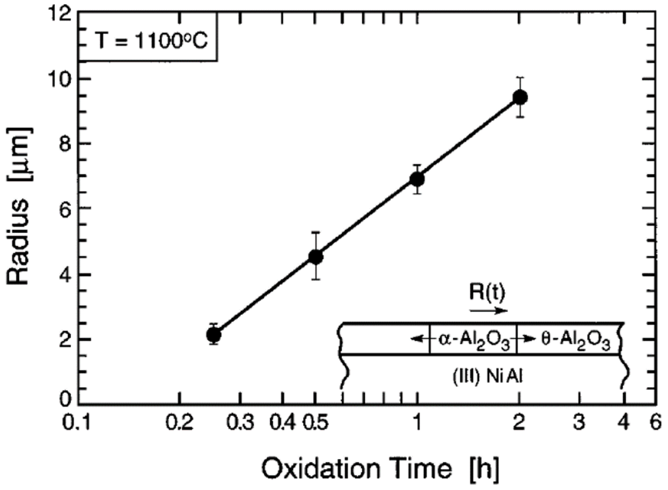

Figure 2.11: Average radius of α-Al_2O_3 patches on (111) NiAl as a function of oxidation time at 1100 °C. The θ- to α-Al_2O_3 transformation followed logarithmic kinetics. Reprinted from [29], with the permission of AIP publishing.

Eventually, the patches impinge upon each other and α-Al_2O_3 covers the entire surface, at which point the transition to slower growth kinetics takes place. After transformation, when the fast upward cation diffusion associated with the metastable phases is reduced, the blade and whisker-like morphology smooths out as surface diffusion takes place [59]. Using photoluminescence spectroscopy to identify the different alumina phases, Tolpygo *et al.* [28] demonstrated that metastable alumina forms with a whisker morphology, and then transforms to α-Al_2O_3 faster than surface smoothing takes place; the whiskers themselves likely transform into the α phase. The whiskers continue to grow until they transform into α, resulting in thinner smoother surface topology in the regions of the scale that transform first. An important point is that the presence of a whisker/blade morphology on the oxide surface is not a reliable indicator of the presence of metastable alumina [28].

Several factors are thought to influence the nucleation density of α-Al_2O_3, including surface finish and substrate orientation. Preferential nucleation of α-Al_2O_3 patches has been observed to occur on surface defects such as polishing scratches (**Figure 2.12**) [61, 63]. Tolpygo *et al.* [28] demonstrated that rougher substrate surfaces promote a faster transformation from θ to α-Al_2O_3, most likely by increasing the nucleation density of α-Al_2O_3. In the corresponding fully-transformed microstructures, the ridge spacing of α-Al_2O_3 on the rougher substrate surface is smaller than that on the smoother substrate (**Figure 2.13**) [28]. The α-Al_2O_3 patch density also seems to depend on substrate orientation [61], though it is unclear why this may occur. Variations of ridge spacing [53, 59] on α-Al_2O_3 scales formed on different orientations in polycrystalline NiAl (**Figure 2.14**) are likely due to differences in α-Al_2O_3 patch density during transient oxidation.

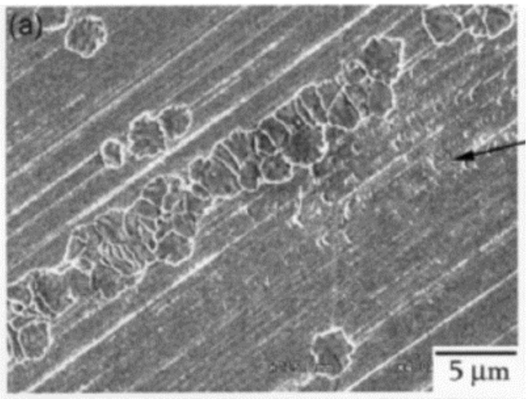

Figure 2.12: SEM images showing the alloy surface after scale removal showing remnants of α-Al_2O_3 patches still adhered to the surface. α-Al_2O_3 preferentially nucleated on polishing scratches. Reprinted from [61].

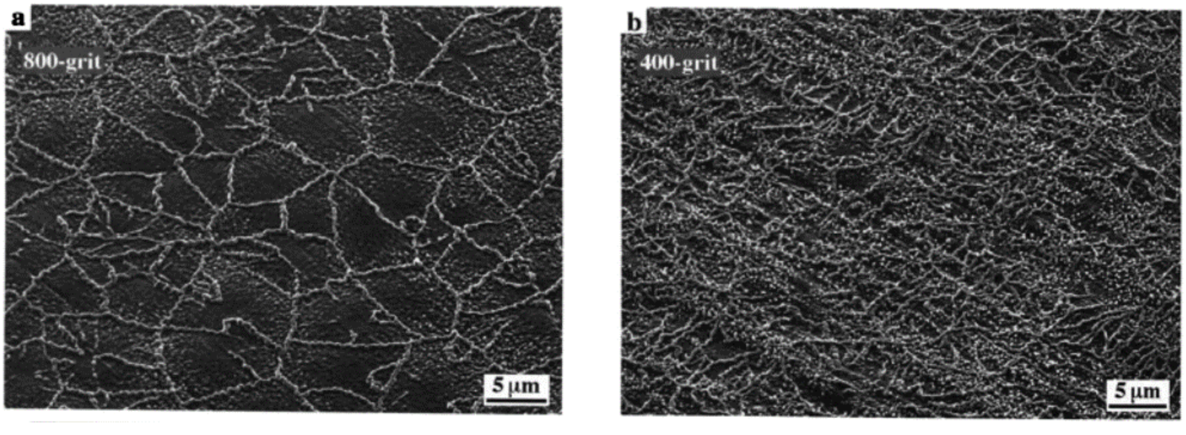

Figure 2.13: SEM surface images of α-Al_2O_3 after oxidation for 1h at 1200 °C on NiAl with a) 800-grit surface finish and b) 400-grit surface finish. Reprinted from [28].

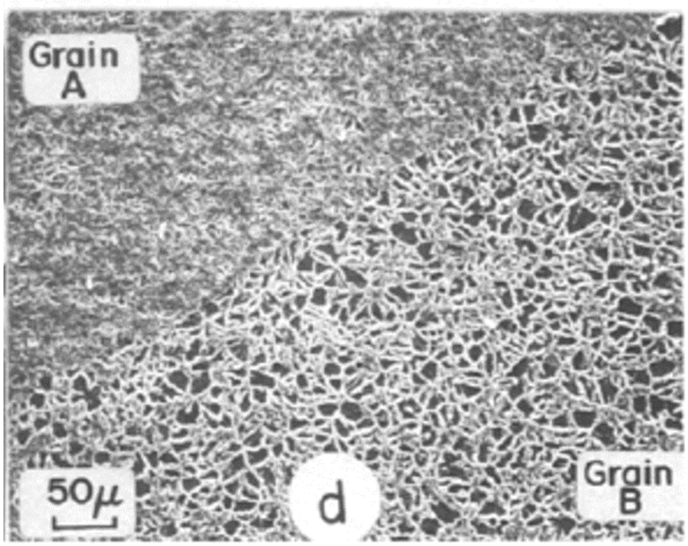

Figure 2.14: SEM surface image of α-Al_2O_3 on Ni-32Al (wt%) after 30min at 1473 K in the vicinity of a NiAl grain boundary. Republished with permission of IOP Publishing, Ltd, from [53]; permission conveyed through Copyright Clearance Center, Inc.

Several authors suggested that the microstructure of the steady-state α-Al_2O_3 scale may depend on the transient stage metastable to α-Al_2O_3 transformation [28, 63, 64]. In particular, the nucleation density of the α-Al_2O_3 patches may determine the grain size of the fully-transformed α-Al_2O_3, thus influencing the oxidation kinetics as oxidation takes place by grain boundary diffusion. Though no direct connection between α-Al_2O_3 nucleation density in the transient stage and oxidation kinetics in the steady-state stage of oxidation exists in the present literature, there is evidence that different orientations of NiAl have different oxidation rates [54, 65, 66] and oxide thicknesses [67].

2.2.3 Dopant Effects on Alumina Transformation

Dopant effects on the transformation from the various metastable alumina phases to α-Al_2O_3 have been widely reported. Burtin *et al.* [68] studied the transformation kinetics of bulk transition γ-Al_2O_3 doped with various cations using XRD to measure the extent of the transformation to α-Al_2O_3 at regular time intervals, finding that additions of In, Ga, Al, and Mg accelerated the transformation (in increasing order), and Zr, Ca, Th, and La inhibited the transformation to α-Al_2O_3 (**Figure 2.15**). The authors suggested that both the ionic radius and the valence of each dopant play a role in the alumina transformation kinetics. They created an empirical diagram based on the ion radius and valence, finding that larger and higher valence ions tended to inhibit the alumina transformation, while smaller and lower valence ions accelerated the transformation to α-Al_2O_3. Beyond ion size and valence, others have suggested that dopants may occupy particular sites in the metastable Al_2O_3 phase that affect the transformation to α-Al_2O_3. Using XRD and reflectance spectra, Tsuchida *et al.* [69] and Bye *et al.* [70] found that additions of Fe ions accelerated the transformation of metastable alumina to α-Al_2O_3, while additions of Cr ions tended to delay the transformation. It was suggested that Cr^{6+} ions sit in tetrahedral positions of the θ-Al_2O_3 phase and strongly bond to oxygen, delaying the transformation to α-Al_2O_3 where Al and substituted Cr ions would occupy only octahedral positions.

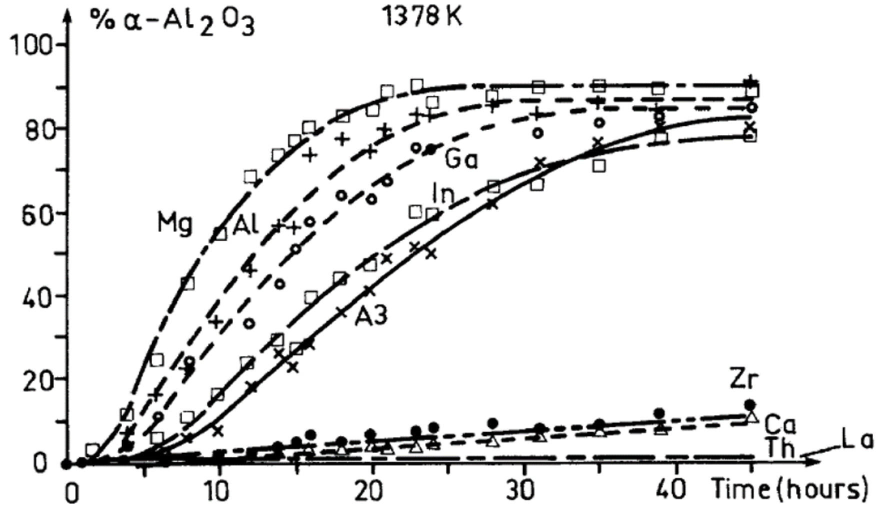

Figure 2.15: Percent conversion to α-Al_2O_3 over time of γ-Al_2O_3 doped with various elements. Reprinted from [68], with permission from Elsevier.

Several studies investigated the effect of dopants in alumina-forming alloys on the θ to α alumina phase transformation during high temperature oxidation in air. Using XRD, Pint *et al.* [71] showed that dispersions Y_2O_3, ZrO_2, La_2O_3, and HfO_2 slowed, while dispersions of Al_2O_3 and TiO_2 accelerated the θ to α-Al_2O_3 phase transformation in scales grown on NiAl alloys. The surface morphologies of the resulting scales were consistent with the transformation speed. Whisker morphology and patches on the Y, Zr, La, and Hf-doped alloys likely resulted from local regions of metastable Al_2O_3 that had not yet transformed, or at least recently transformed (i.e. extensive surface diffusion has not occurred). In contrast, dense ridges observed on the Al_2O_3 and Ti-doped alloys indicated that the complete transformation to α-Al_2O_3 occurred earlier. It is also important to note that oxide dispersions generally resulted in faster alumina phase transitions than dopants added by alloying or ion implantation, which may be partially caused by increasing the number of nucleation sites for α-Al_2O_3. Pint *et al.* suggested that these results were consistent with the model of Burtin *et al.* [68] in that Ti, with a smaller ionic radius, accelerated the alumina transformation while Y and La were the most effective inhibitors and had the largest ionic radii. Pint *et al.* also suggested that the large Y and La ions could inhibit the transformation by distorting the cubic lattice of the metastable alumina structure, making a diffusion-less shear type transformation more difficult. Several studies noted that the addition of Cr seems to accelerate the transformation to α-Al_2O_3 [27, 72, 73]. One possible mechanism is the formation of Cr_2O_3 acting as a template layer for α-Al_2O_3 due to the similar structure of the two phases, promoting the nucleation of α-Al_2O_3 [27, 72].

Much research on transient oxidation has focused on the effect of doping NiAl with yttrium, which is widely used as a dopant in commercial alloys to increase scale adherence and lower scale growth rate [74]. Jedlinski and Borchardt [75] found that the ridge structure was suppressed on the Y-doped alloy, and instead the surface was covered by blade-like grains, suggesting that Y-doping delayed the alumina metastable-stable transformation. They also found that alumina on the Y-doped NiAl was dominated by outward growth, consistent with the growth mechanism of metastable alumina [51]. Rommerskirchen *et al.* [52] found that Y and Ce delayed, while Hf accelerated the transformation, but did not discuss possible mechanisms. Choi *et al.* [62], detected some θ-Al_2O_3 in the scale grown on Y-implanted NiAl, but detected only α-Al_2O_3 in the un-doped scale after the same oxidation time. Similar blade/whisker morphology was observed on the Y-doped alloy as in the studies described previously due to the inhibition of the alumina transformation. They suggested that Y is incorporated in the metastable θ-Al_2O_3 and potentially slows the transport of Al cations, which would inhibit the transformation to α-Al_2O_3. Jedlinski [76] outlined several mechanisms by which Y may affect the phase transformation of thermally grown alumina during transient oxidation. They proposed that Y may provide heterogenous nucleation sites for α-Al_2O_3, accelerating the transformation. Alternatively, they suggested that the large Y ion occupies the octahedral site in the metastable alumina phase and delays the transformation to α-Al_2O_3 by decreasing the number of anion vacancies, which are likely involved in the transformation to α-Al_2O_3 [68]. In summary, though the exact mechanism is not established, it is accepted that Y delays the transformation from metastable- to α-Al_2O_3.

2.3 Steady-State Oxidation of NiAl

2.3.1 Alumina Microstructure and Oxidation Kinetics

After the scale has completely transformed to α-Al_2O_3, a network of ridges forms on the surface of the oxide (**Figure 2.16**), a well-documented feature of alumina scales grown on NiAl alloys [27, 28, 30, 53, 59, 71, 77]. Ridged networks on the alumina surface are not unique to NiAl, and are thought to form when the α-Al_2O_3 nuclei density is low [30]. Thus, alloys with higher rates of α-Al_2O_3 nucleation, such as NiCrAl and FeCrAl, do not exhibit surface ridges [78, 79]. Doychak *et al.* [58, 59] provided detailed characterization of the structure of the fully-transformed alumina scale formed on NiAl. Each α-Al_2O_3 patch consists of radial, slightly misoriented sub-grains (up to ~7°). The patches are thinner at their centers, where the metastable alumina first transformed to α, and radial cracks are present. The grain boundaries created by α-Al_2O_3 impingement and cracking provide fast diffusion pathways for upward aluminum diffusion. Consequently, protruding ridges form both at the impingement sites of α-Al_2O_3 patches and along the radial cracks at the center of each patch. Smaller ridges form on the sub-grain boundaries within the α alumina patch. Protruding oxide have also been observed on the underside of spalled oxide and at the scale-alloy interface in cross-section (**Figure 2.17**), along with imprints of the ridge on the exposed metal after spalling [28, 53], indicating that oxygen diffusion downward along the same grain boundaries also plays an important role. The ridges continue to grow during oxidation, and eventually overgrow and impinge on the oxide surface [28, 30], resulting in a thicker scale with equiaxed grains. The alumina continues to thicken over time via concurrent outward aluminum and inward oxygen diffusion along grain boundaries [80].

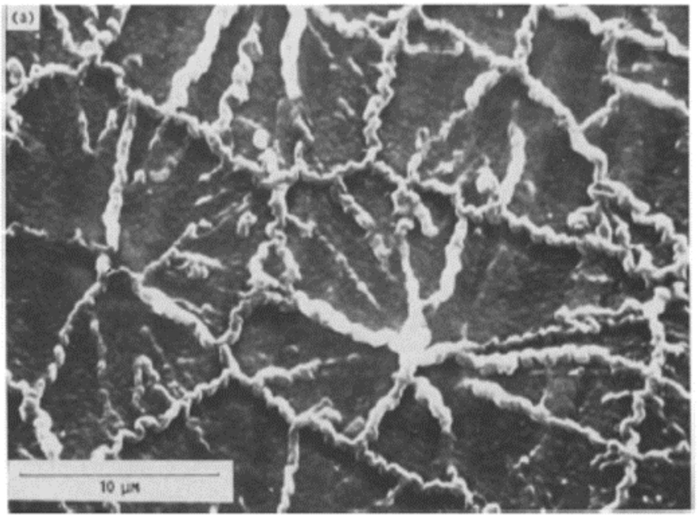

Figure 2.16: SEM image of α-Al_2O_3 on NiAl+Zr after 100h of oxidation at 1100 °C. Reprinted by permission from Springer Nature: [30].

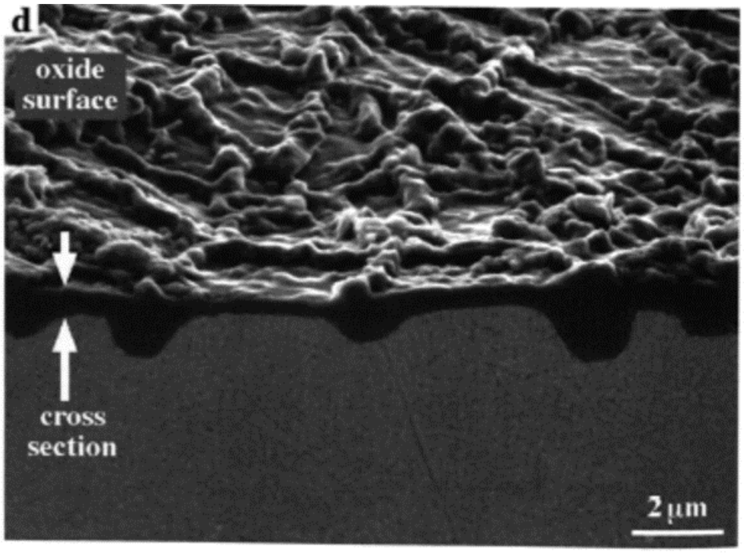

Figure 2.17: Polished cross-section SEM image of α-Al_2O_3 on NiAl after 1h of oxidation at 1200 °C. Thicker oxide protrusions are present at the grain boundaries, with thinner oxide between. Reprinted from [28].

As oxidation of NiAl proceeds, large, faceted voids are often observed at the scale alloy interface (**Figure 2.18**) [53, 77, 81-85]. These void facets align crystallographically with the NiAl metal, possibly due to preferred growth along low-energy (110) planes in β-NiAl [77].

Void density varies with substrate orientation, possibly due to differences in the dislocation density or alumina-metal interface structure between different metal orientations [84]. Despite the large interfacial cavities, the alumina directly above the voids was observed to have the same thickness as the alumina still in contact with the NiAl metal [53, 77, 82], indicating that Al is still supplied to the growing scale. It has been suggested that Al vapor transport is feasible at temperatures above 1000 °C [53], consistent with observations of facets and spiral steps seen along the void faces [53, 77]. At lower temperatures, surface and interface diffusion may play a role in transporting aluminum and maintaining a constant scale thickness. Though they do not seem to have a significant effect on oxidation kinetics, the voids can be detrimental to scale adherence.

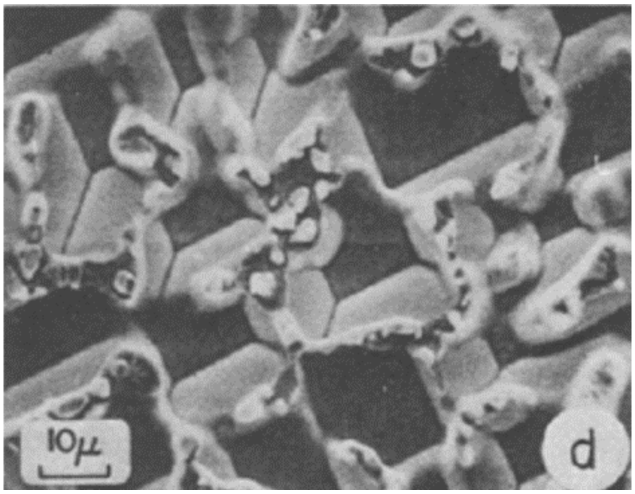

Figure 2.18: Faceted voids at the oxide-metal interface revealed by scale spalling on a Ni-32 (wt%) alloy oxidized for 15 days at 1473 K. Republished with permission of IOP Publishing, Ltd, from [53]; permission conveyed through Copyright Clearance Center, Inc.

The origin of the interfacial voids is of great interest due to their association with scale spallation and component lifetime reduction [81]. The voids are thought to form due to the coalescence of vacancies at the scale-metal interface [85-87]. Vacancies may be produced in this region in the transient stage of oxidation when metastable alumina phases form by rapid outward

Al diffusion. As Al diffuses upward into the oxide, vacancies are left behind in the metal and the diffusion of Al from the bulk alloy to the interface is not fast enough to fill these vacancies. Alternatively, vacancies can accumulate by a Kirkendall effect. As aluminum is selectively oxidized, nickel is enriched in the alloy near the scale-alloy interface, and then, driven by concentration gradient, diffuses back into the alloy and leaves vacancies behind. Consistent with this mechanism, the flux of nickel into the alloy exceeds the flux of aluminum from the alloy to the growing scale, as confirmed by the work of Brumm and Grabke [81]. They found that NiAl alloys with excess aluminum relative to nickel had far fewer voids than alloys with lower Al content. The authors suggested that this was due to the changes in relative diffusivities of Al and Ni with varied NiAl composition. In NiAl with up to 50 at% aluminum, D_{Ni}/D_{Al} is roughly 3, and the flux of Ni away from the interface exceeds the flux of Al to the interface. But as the Al concentration surpasses 50 at%, D_{Ni}/D_{Al} approaches 1. Thus, the flux of Ni away and Al to the oxide-metal interface is about equal, and large interfacial voids are less likely to form. In further support of this hypothesis, Gleeson *et al.* [88] demonstrated that Pt additions increase the diffusivity of Al in NiAl alloys, and Pt-modified NiAl alloys typically form fewer interfacial voids [89, 90]. It was proposed also that sulfur, present as an impurity in most alloys, plays a significant role in stabilizing interfacial voids and reducing scale adherence [91-94]. Several studies have detected sulfur on the surface of voids underneath spalled portions of alumina scales using Auger spectroscopy and at the scale-alloy interface [91, 93]. Sulfur may also lower the surface energy of the metal, stabilizing the large voids and weakening the scale-alloy interface [95]. Cyclic oxidation of alloys with varied amounts of sulfur demonstrated that scale spallation increased with sulfur content [92]. After prolonged oxidation, Svensson *et al.* [85] observed that some of the large interfacial voids formed during oxidation of NiAl “healed” with new oxide

(**Figure 2.19**). They proposed that this was due not only to the inward growth of Al_2O_3 to fill the voids, but also because oxygen may be able to reach the void surfaces in some cases through microcracks in the scale and form new oxide with the metal.

Figure 2.19: TEM image of an alumina scale grown on Ni-47Al-5Pt showing interfacial voids. Some voids are partially filled with Al_2O_3 that has grown from the metal surface (white arrows). Reprinted by permission from Springer Nature: [85].

After long oxidation times, alumina scales typically exhibit microstructures consisting of two distinct layers. The region near the surface of the scale exhibits smaller, equiaxed grains, while the region near the scale-alloy interface tends to have elongated columnar grains (**Figure 2.20**). This dual-layered microstructure has been widely observed on both FeCrAl- [96-101] and NiAl-based [53, 102-104] alloys and is thought to form due to concurrent upward Al and inward O diffusion through the scale. Mennicke *et al.* [98] correlated the dual-layered microstructure with secondary ion mass spectrometry (SIMS) profiles through a scale oxidized using isotopic tracers, finding that scales with the dual equiaxed and columnar layers exhibited both inward and outward growth of new oxide, while profiles through the scale with almost entirely columnar grains showed that new oxide formed almost exclusively at the oxide-metal interface. Clarke *et* *al.* [99] describes the development of the dual-layered structure (**Figure 2.21**), suggesting that the upper equiaxed layer of grains arises as new oxide forms at the surface of the scale above the scale grain boundaries, commonly observed as ridge networks of new surface oxide. With increasing oxidation time, the new oxide above the boundaries grows and eventually impinges upon new oxide growing from adjacent boundaries, creating additional impingement boundaries. With further oxidation, oxide continues to form above these new impingement boundaries which are transport pathways for Al upward through the scale. Thus, measurements of the relative thicknesses of the equiaxed and columnar layers are thought to be a reasonable estimation of the relative transport of Al upward and O inward along the grain boundaries.

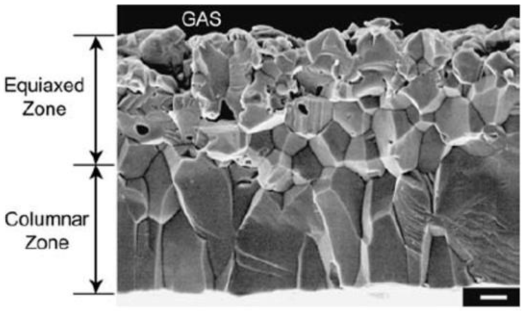

Figure 2.20: SEM image of a fracture section of an alumina scale grown on FeCrAlZr after 22.5h of oxidation at 1300 °C. Marker bar is 1 µm. Reprinted by permission from Springer Nature: [99].

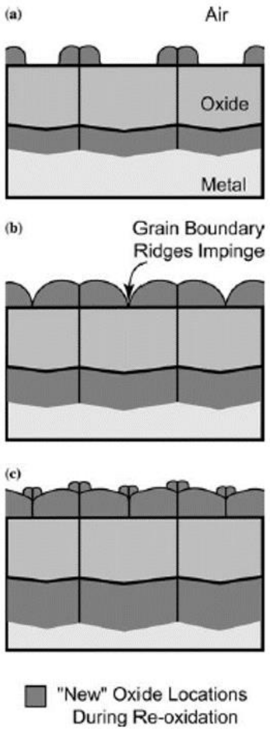

Figure 2.21: Schematic of alumina in cross-section demonstrating idealized growth over time. New oxide develops above grain boundaries in (a) and eventually impinge in (b). New oxide continues to develop where previous ridges impinged to create new grain boundaries in (c). Reprinted by permission from Springer Nature: [99].

The alumina scale tends to have a texture independent of substrate orientation. Naumenko *et al.* [100] found that the alumina scale on a FeCrAlY alloy, which was dominated by columnar grains, had a preferred crystallographic orientation with the [0001] direction parallel to the growth direction and normal to the scale/metal interface (**Figure 2.22**). The authors suggested that the preferred orientation with growth direction arises from competitive grain growth. Al-Badairy *et al.* [101] found that alumina scales formed on FeCrAl alloys developed a fibre texture that was not dependent on substrate orientation, with the <1011> direction perpendicular to the metal surface. They proposed that small equiaxed grains with random orientations initially grow at the metal surface, followed by competitive growth of these grains into the metal with increasing oxidation time. Blachere *et al.* [105] found that thinner scales on both FeCrAl and FeCrAlY exhibited no preferred orientation, despite the columnar morphology. White *et al.* [106] performed TKD on an alumina scale formed on a NiAl+Zr alloy, noting a slight [0001] texture. However, the authors also pointed out that the small sample size of the TKD data may not be representative of the entire sample. Karadge *et al.* [107] studied thermally grown alumina on NiAl+Pt and NiCrAl bond coats, finding in that on the NiAl+Pt coating the alumina exhibited a significant basal texture, with the c-axis perpendicular to the metal surface, while on the NiCrAlY coating no significant texture was observed.

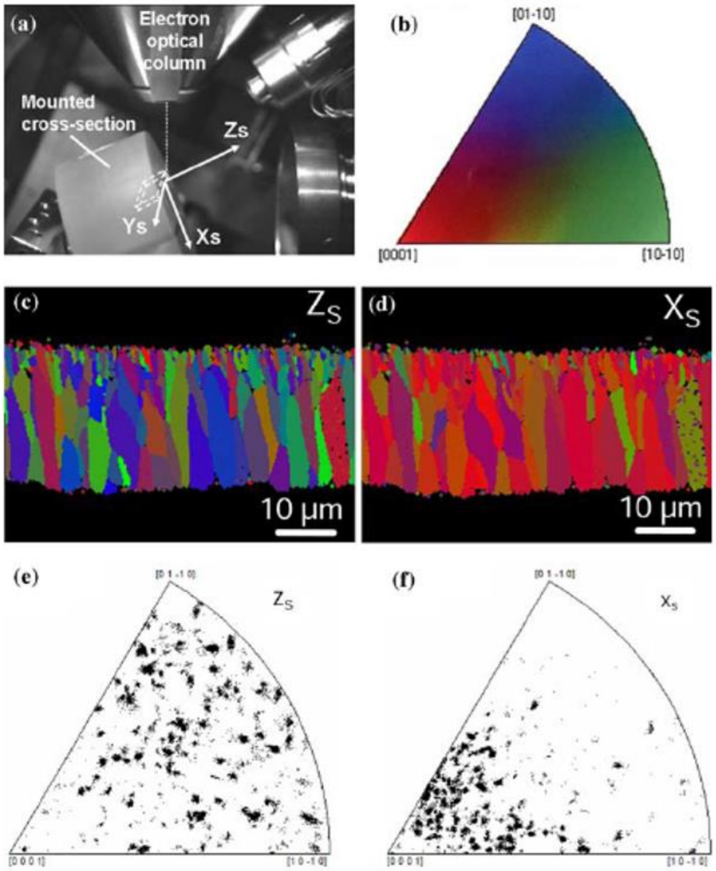

Figure 2.22: EBSD mapping of alumina formed on FeCrAlY after 2000h of oxidation at 1200 °C. a) schematic of analysis set-up. b) Crystallographic orientation legend. c) and d) EBSD orientation maps and e) and f) inverse pole figures for the Z_s and X_s directions, respectively. Reprinted by permission from Springer Nature: [100].

The scale grain size is also an important consideration. Since transport occurs along grain boundaries, alumina growth rate is inversely dependent on scale grain size [108, 109]. During oxidation at high temperature, diffusion-mediated processes may take place. Grain growth, for example, is well-known to occur in bulk polycrystalline α-Al_2O_3 [110-112]. However, there are few studies in the current literature that address thermally activated grain growth in growing alumina scales. One study by Choquet *et al.* [113] found that grain growth in alumina scales on NiCoCrAl alloys was extremely slow compared to bulk alumina. Rather than thermally activated grain growth, others suggested that grain size on alumina scales evolve due to their intrinsic scale growth mechanisms [20, 100]. Naumenko *et al.* [100] found a linear relationship between the average alumina grain size and the distance from the scale-gas interface on a FeCrAlY alloy (**Figure 2.23**). This grain size relationship did not change for different oxidation temperatures, and the authors suggested that grain size evolved due to the competitive inward growth of the columnar alumina grains. Currently, the mechanisms controlling the evolution of alumina grain size during oxidation are not understood, but grain size is known to have a significant effect on oxidation rate.

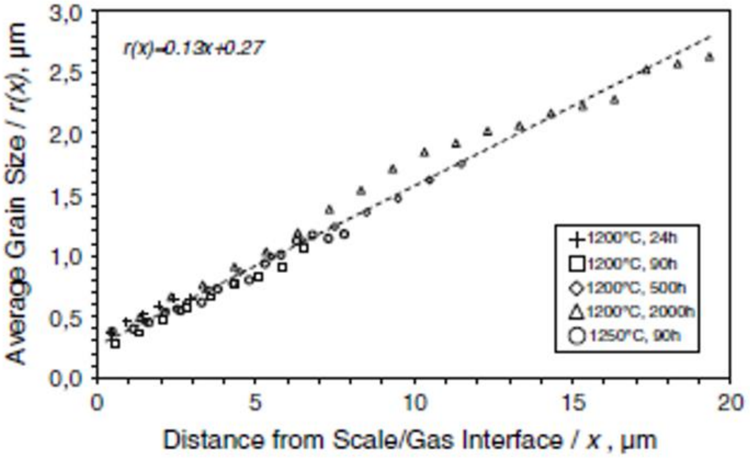

Figure 2.23: Average alumina grain size as a function of distance from the scale surface, as determined from SEM/EBSD images of the scale on FeCrAlY formed after different times at 1200 °C and 1250 °C. Reprinted by permission from Springer Nature: [100].

Alumina scales are thought to deviate from parabolic kinetics due to the evolution of grain size with scale thickness. Oxidation kinetics are classically assumed to be parabolic after the initial period of transient oxidation. However, the oxidation kinetics of alumina tend to be lower than predicted by parabolic kinetics as oxidation progresses. Instead, the alumina growth kinetics can be described as “sub-parabolic” [20, 114] and fit with reasonable accuracy using a power law relationship $\Delta x = kt^n$ where n~0.32-0.36 (instead of 0.5 as for parabolic kinetics). This sub-parabolic behavior at longer oxidation times has been attributed to the fact that grain size through the thickness of the scale changes as oxidation progresses [20, 100, 108]. Specifically, the density of transport pathways decreases with increasing grain size as the scale thickens and consequently the oxidation rate slows over time. Models of alumina scaling kinetics were developed by considering the variation of grain size with oxidation time [100, 108, 109, 115]. Oxide thickness at longer times was more accurately predicted by taking increasing grain size into account instead of assuming classical parabolic behavior, or even a constant n for the power law dependence.

2.3.2The Reactive Element Effect

The beneficial effect of small amounts of dopant elements such as Y, Zr, Ce, and Hf on high temperature oxide scale growth is well known and has been extensively studied in the past 60 years or so. Several reviews [7-9, 116] of the so-called “reactive element effect” present a fairly robust picture of how dopant elements affect oxidation, particularly in alumina scales, and what mechanisms may be at play. The reactive element effect has been well-documented across several different alloy systems, oxidation conditions, and types of dopant elements, and can be summarized with the following major observations:

- reduction in oxidation rate
- improved scale adhesion; reduced spallation

The mechanisms by which reactive element additions are thought to lead to these beneficial effects are now described.

2.3.3 Alumina Growth Mechanisms

Dopants are believed to affect the transport of Al and/or O through the alumina scale, consequently affecting the scale growth mechanism. A commonly used method to investigate the growth mechanisms of oxide scales, i.e. where the formation of new oxide is taking place, is the use of 2-step isotopic tracer experiments. This technique is thought to be a more accurate way to trace the oxide growth mechanism than marker experiments, which were commonly used in early studies and found to be problematic [57]. Samples are first oxidized in one oxygen isotope (e.g. $^{16}O_2$) and subsequently oxidized in a different oxygen isotope (e.g. $^{18}O_2$). After this 2-step process, secondary ion mass spectroscopy (SIMS) or nuclear reaction analysis/ proton activation are used to ascertain the location of the two different isotopes with respect to the oxide scale. The profile of the isotope used in the 2nd stage of oxidation indicates where new oxide formed, providing insight into the primary transport mechanisms taking place. Overviews of the theoretical profiles one may expect for the different possible transport mechanisms (**Figure 2.24**) may be compared with experimental profiles [117, 118].

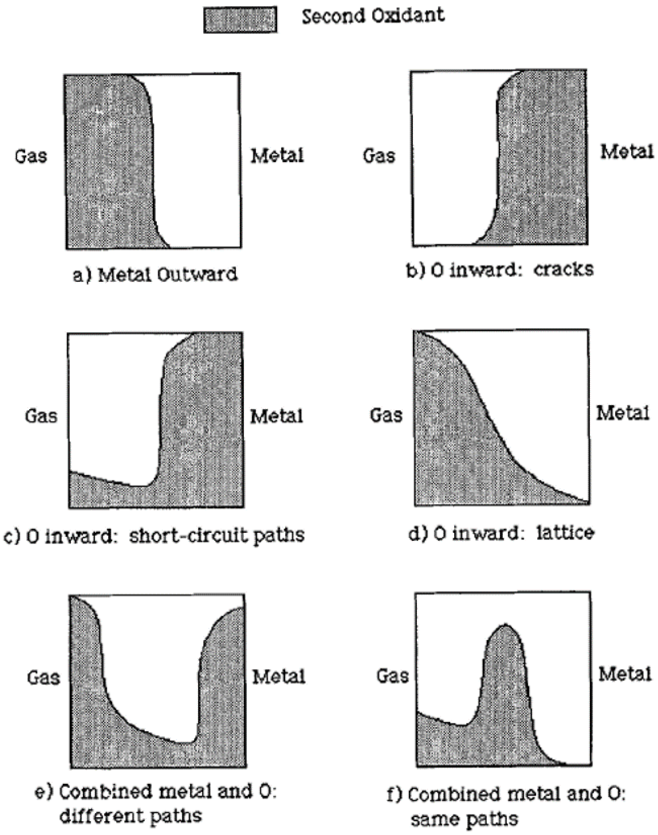

Figure 2.24: Theoretical sputter depth profiles for 2-stage tracer oxidation experiments. The shaded area refers to the location of the second oxidant (usually ^{18}O). Reprinted by permission from Springer Nature: [118].

Using isotopic tracer experiments, numerous studies [56, 57, 98, 117-125] attempted to clarify the growth mechanisms of alumina during the oxidation of both Fe- and Ni-based alloys. Pint *et al.* [118] studied NiAl and FeCrAl alloys, un-doped and doped with Zr or Y, and found that the un-doped alloys formed new oxide at both the scale-gas and scale-metal interface, indicating a mixed growth mechanism with simultaneous Al and O transport. With the addition of either Zr or Y, new oxide appeared mainly at the scale-metal interface, indicating that the dopants changed the growth mechanism to mostly inward growth via O transport. Mennicke *et al.* [98] clearly demonstrated that additions of Y to a FeCrAl alloy leads to the formation of new oxide almost exclusively at the oxide-scale interface. This change in the scale growth mechanism is also indirectly apparent in the change in microstructure from a dual-layered oxide with both equiaxed grains near the surface and columnar grains further down, to almost all columnar grains (**Figure 2.25**). Prescott *et al.* [122] studied NiAl alloys using SIMS images, rather than average sputter profiles, to show the distribution of ^{18}O throughout the scale. SIMS images of the scale surface confirmed that new oxide formed above grain boundaries, and not in any significant amount in the bulk grains between the boundaries. SIMS images of tapered cross-sections of the alumina demonstrated that new oxide formed at both the scale-gas interface and the scale-metal interface. Additionally, ^{18}O was detected in localized regions within the middle of the scale, which the authors suggested arose from oxygen transport along the grain boundaries. Using a similar technique, Schumann *et al.* [123] showed that in comparison to the un-doped NiAl alloys [122], NiAl doped with Zr or with Y both reduced the formation of new oxide at the outer surface of the scale. SIMS maps of cross-sections of the Zr-doped sample revealed that most of the ^{18}O signal was distributed at the scale-metal interface as well as in localized channels (presumably grain boundaries) near the scale surface. On the Y-doped sample, the ^{18}O signal was concentrated at the scale-alloy interface, indicating that while both Zr and Y reduce upward Al transport, Y seems to be more effective. Generally, the reduction in outward alumina growth was observed on a wide variety of alumina-forming alloys with various dopant additions. However, some inconsistencies arise when factors such as the phase of alumina and microstructure of the scale are not considered. For example, Young *et al.* [119] found that doping NiAl alloys with Y seemed to increase the formation of new oxide at the scale-gas surface and suppress growth at the scale-metal interface, in contradiction to the studies describing the transition to mostly inward growth with dopant additions. However, it was later clarified that this was likely due to the presence of metastable alumina phases, which tend to exhibit rapid outward growth [51]. In this case, the metastable alumina may have persisted longer due to the Y addition, giving the misleading result that Y changes the growth mechanism of α-Al_2O_3 to mostly outward growth by Al transport during steady-state oxidation.

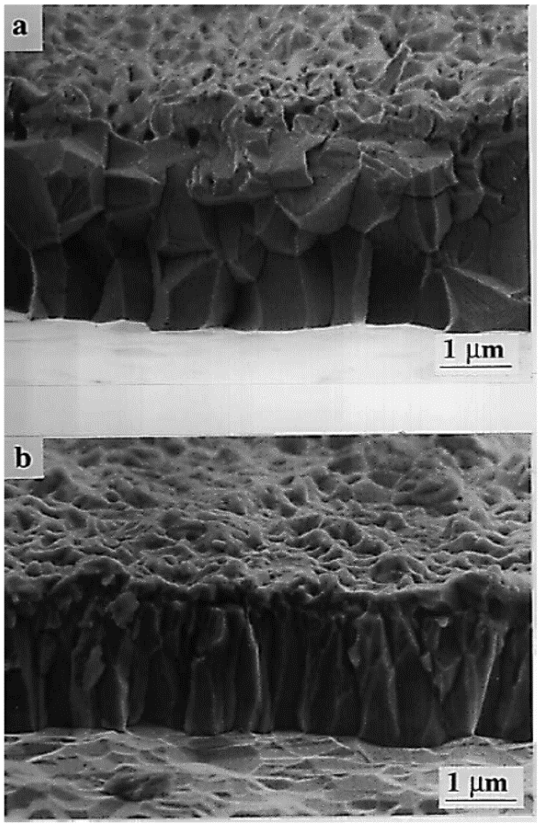

Figure 2.25: SEM images of fracture sections of alumina scales grown on a) FeCrAl and b)FeCrAl+Y after 5h of oxidation at 1200 °C. Reprinted by permission from Springer Nature: [98].

Jedlinski *et al.* [124] discussed several factors related to SIMS analysis that should be considered when designing tracer experiments and interpreting the results for assessing oxide growth mechanisms. They emphasized that the sputtering process during the collection of SIMS data can be highly non-uniform due to the scale morphology (for example, the surface oxide ridges observed on NiAl), leading to inaccurate concentration-depth profiles. They also stressed the importance of understanding the oxide microstructure before choosing the SIMS analysis conditions, such as resolution. Despite some of the pitfalls of the interpretations of SIMS data, the numerous studies assessing the growth mechanism of alumina during thermal oxidation are fairly consistent, and agree that the addition of small amounts of dopant elements changes the scale growth mechanism of alumina scales from a mixture of outward cation diffusion and inward anion diffusion to primarily inward oxygen diffusion, though there is evidence that some outward Al diffusion still takes place. Nychka *et al.* [99] demonstrated that significant Al transport along the grain boundaries still took place on doped samples through an experiment in which they first oxidized several FeCrAl-based alloys to form an alumina scale, then removed the upper equiaxed layer of the scale by mechanical polishing to prepare a flat surface, and then re-oxidized the samples to form new oxide (**Figure 2.26**). They observed new oxide formed above the scale grain boundaries, and used AFM to measure the volume of new oxide and calculate the flux of aluminum upward along the grain boundaries. By comparing the aluminum flux on several commercial alloys with different dopants as well as no dopant addition, they found that dopants reduced the upward flux of aluminum through the scale. The authors also found that differences in both dopant element and its form in the alloy (oxide dispersion versus alloyed or implanted) elicited varied effects on the relative magnitudes of inward oxygen and outward aluminum diffusion.

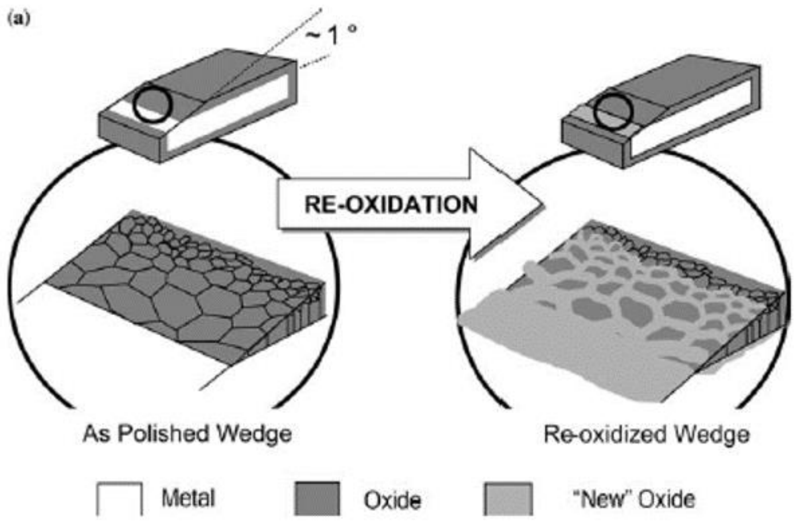

Figure 2.26: Schematic of the re-oxidation experiment showing the growth of new oxide ridges above scale grain boundaries. Reprinted by permission from Springer Nature: [99].

2.3.4 Al/O Transport and Dopant Segregation

Though it is clear that dopant elements affect Al/O transport through alumina scales, it remains difficult to pinpoint the mechanisms. With advancements in characterization techniques such as TEM/STEM and APT, dopant element additions are readily observed to segregate to the grain boundaries and interfaces throughout the alumina scale during oxidation (**Figure 2.27**) [97, 98, 123, 126-128]. The driving force for this segregation is thought to be the low solubility of the dopant additions in Al_2O_3, and the misfit strain caused by their relatively larger ion size compared to Al [97]. Numerous hypotheses have been put forward to explain how dopants on the grain boundaries affect Al and O transport.

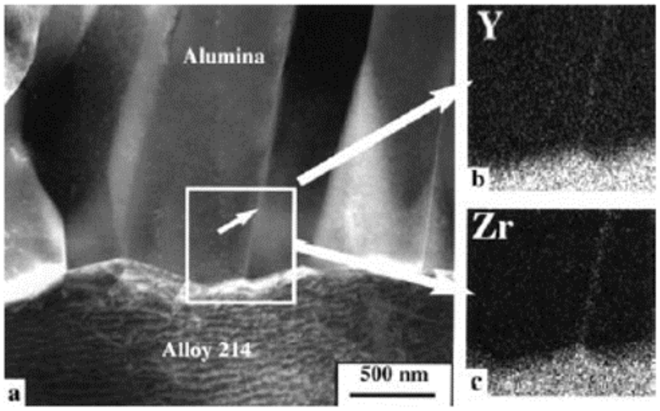

Figure 2.27: a) STEM dark field image of the alumina-metal interface of a Fe-based alloy oxidized for 100 1h cycles at 1100 °C. X-ray maps showing b)Y and c) Zr segregation along the alumina grain boundaries. Reprinted from [129].

Dopants have been found to segregate to grain boundaries in bulk polycrystalline α-Al_2O_3 and affect Al and O transport, and mechanisms suggested to explain this effect may offer insight into the dopant effect on transport through thermally grown α-Al_2O_3 scales. Several studies using oxygen isotope tracers found that Y additions segregated to grain boundaries and reduced the oxygen grain boundary diffusivity in bulk polycrystalline α-Al_2O_3 [130-132]. Oxygen grain boundary diffusivity seems to vary among individual grain boundaries [133-135], thus it was proposed early on that segregated dopants alter the grain boundary structure. However, Y does not appear to change the grain boundary structure [131, 136], so must have some other effect on the electronic structure, bonding, or defect concentration at the grain boundary. It was suggested that Y may reduce O diffusion by a “site-blocking” mechanism, in which the large Y ions reduce the effective grain boundary area [130-132]. Another proposed mechanism is that Y^{3+} ions, which are isovalent with Al^{3+}, occupy cation sites at the grain boundary and block the segregation of aliovalent impurities such as Si^{4+} that may otherwise occupy cation sites and increase defect concentrations [131]. Others propose that Y increases the metal-oxide bonding strength, inhibiting diffusion [136, 137].

Concerning Al grain boundary diffusion, far fewer studies are available due to the experimental difficulty in using Al isotopes. As an alternative, creep studies can provide clues as to how dopants affect grain boundary diffusion. In bulk polycrystalline α-Al_2O_3, dopants such as Y, Zr, and La segregate to grain boundaries and reduce the creep rate of Al_2O_3 [138, 139]. Creep of Al_2O_3 is thought to be limited by the diffusion of Al cations along the grain boundaries, with the assumption that oxygen grain boundary diffusion is much faster than that of aluminum [140]. Thus it was suggested that dopants reduce creep rate by inhibiting Al diffusion on the grain boundaries [138, 139]. However, a later study measured Al grain boundary diffusion directly using a ^{26}Al isotope in un-doped and Y-doped α-Al_2O_3, and found that the Y addition had no effect on Al tracer diffusion [141]. These authors also measured the diffusion of Al to be 3-4 orders of magnitude faster than the diffusion of oxygen along the grain boundaries. Considering these two results, the authors suggested that the assumption that creep in Al_2O_3 is rate-limited by the diffusion of Al cations may be wrong. Despite the observation that Y additions do not affect Al grain boundary diffusivity in bulk Al_2O_3, Y additions do seem to decrease Al transport in thermally grown Al_2O_3 scales.

Though bulk ceramic studies can provide some insight about grain boundary transport and the effects of dopants in alumina, key differences between bulk alumina and thermally grown alumina scales may lead to different transport behavior. Oxidation experiments are typically performed at lower temperatures (800-1200 °C) than bulk ceramic studies (1400-1800 °C), which may affect transport mechanisms. In addition, thermally grown scales are subject to a steep oxygen potential gradient, with the exposed scale surface at a high oxygen partial pressure, and the inner scale-alloy interface at a much lower oxygen partial pressure according to thermodynamic equilibrium. As a result of this gradient, not only do the dopants segregate to the interfaces, but they actively diffuse toward the surface of the scale during oxidation, as described by Pint (**Figure 2.28**) [128]. Pint argued that the larger dopant elements diffuse more slowly than the smaller Al cations upward along the grain boundary, inhibiting the upward diffusion of Al and resulting in the observed change in oxide growth mechanism and a reduction in overall oxidation rate. In a subsequent study, Pint *et al.* [142] suggested that the oxygen potential gradient throughout the scale is likely the driving force for the upward diffusion of dopants, and large, oxygen-active elements with slow upward diffusion rates seem to be the most effective in slowing Al diffusion. The "site-blocking" mechanism, with larger ions being more effective diffusion inhibitors, has been proposed by several authors in the context of alumina scales [97, 99, 143]. However, there is not a strong correlation between ion size and the effectiveness of a dopant in reducing oxidation rate [144]. For example, doping with Hf results in significantly reduced oxidation rate compared to larger ions such as Y [129, 144, 145]. Another consideration for thermally grown alumina scales is their electronic structure. Reactions at the scale surface and scale-alloy interface involve electronic defects, i.e. electrons and holes, and the availability of these defects can affect the creation of Al/O vacancies and consequently Al/O diffusion [146]. Heuer *et al*. [134, 146] proposed that dopant elements may alter the donor and acceptor states at grain boundaries and as a result affect Al/O diffusivity.

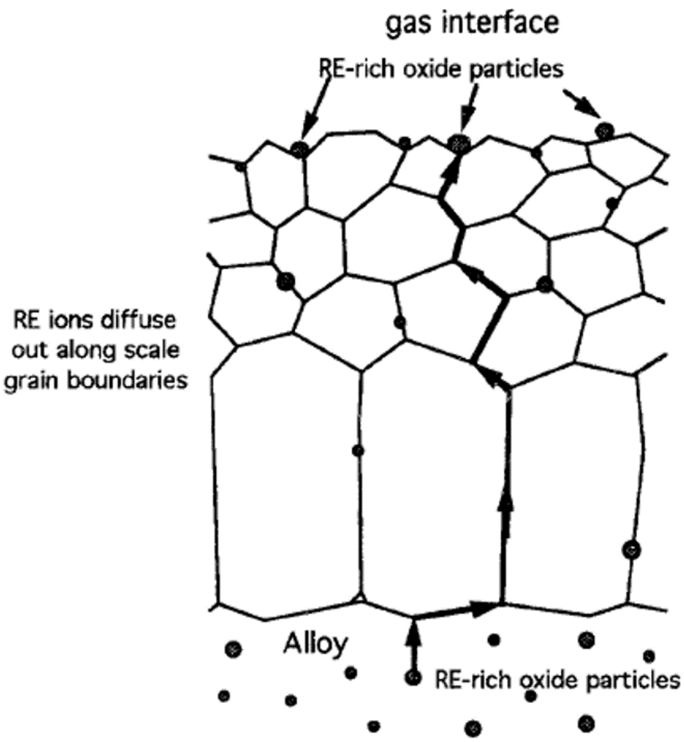

Figure 2.28: Schematic of outward reactive element diffusion during high-temperature oxidation. Ions diffuse outward from the metal along scale grain boundaries and become enriched at the scale-gas interface. Reprinted by permission from Springer Nature: [128].

A variety of other mechanisms for dopant effects on Al/O transport in the context of thermally grown alumina scales have been proposed. Point defects at grain boundaries such as aliovalent dopant ions have been suggested to alter defect concentrations such as Al and O vacancies and thus influence Al/O transport in the grain boundary region [147, 148]. However, it is difficult to determine the mechanism of the dopant effect on Al/O transport because the diffusing species is not currently known. Tautschnig *et al*. [147] modeled the grain boundary diffusion of ionic and electronic defects along scale grain boundaries and found that Al cation vacancies and holes were the dominant defects in scales under the steep oxygen potential gradient typical for oxidation experiments.

2.3.5 Dopant Optimization and Co-Doping

Though “reactive element” effects have been observed with a variety of dopant elements and base alloys, one challenge in comparing their effectiveness is dopant concentration in the alloy. Studies that attempt to optimize oxidation resistance by screening for dopant type and experimenting with many possible dopant elements tend to add the same amount of dopant to the base alloy and compare the results to the un-doped alloy [71, 143]. However, it appears that the maximum benefit in reducing oxidation kinetics and spallation can be achieved by an “optimal” dopant concentration [144], and this concentration can be different depending on the specific dopant element and alloy composition. Having too little dopant shows little to no improvement in oxidation resistance, presumably due to inadequate segregation along the grain boundaries. On the other hand, having too much of a dopant, or “over-doping”, can lead to accelerated scale growth and spallation [144]. It is thought that over-doping occurs when the dopant concentration is high enough to form oxides within the scale that can act as points of high stress and result in scale spallation, and also may increase the oxidation rate by providing fast diffusion paths for oxygen. Gheno *et al.* [149] used thermodynamic modeling to predict the optimal Hf addition for oxidation resistance of a NiCrAl alloy on the basis of limiting the formation of Hf-oxides. In comparison with oxidation experiments on alloys with varied Hf levels, their model predicted with reasonable accuracy the amount of Hf required before internal Hf-oxides formed, and seems to be a promising approach for optimizing dopant levels.

Adding multiple dopants also may result in a synergistic response in improving oxidation resistance (**Figure 2.29**) [129, 150-152]. Additions of Y+Hf to Fe-based alloys not only reduced oxide growth rate, but also considerably improved the scale adhesion, which is critical for protective scale lifetime [129, 150]. It was noted that the level of Y used in this co-doped alloy was not normally effective when added alone [97], and the base NiCrAl alloy doped with only Hf or Y spalled much more quickly than the alloy with both Y and Hf. Pint [129] suggested that with two dopant elements, the oxide scale grain boundaries are still effectively doped to exhibit the typical reactive element effect benefits, but the alloy has low enough concentrations of each individual dopant element that they will not form detrimental internal oxides that can increase oxidation kinetics and spalling. To further explore the mechanisms behind the co-doping effect, Pint used TEM-EDS line profiles to quantify the segregation of dopant elements along the oxide scale grain boundaries for both single-doped and co-doped alloys. For the single-doped alloys, the measured grain boundary segregation correlated slightly with lower growth rate constants. However, for the co-doped alloys, no such pattern was observed; the co-doped alloys exhibited both low segregation levels and low oxide growth rates. Co-doping did not increase the total amount of grain boundary segregation, and Pint speculated that the benefits of co-doping may be related instead to limiting the formation of internal RE-oxides. It was also suggested that dopants of different sizes and/or charges may segregate to different sites on the alumina grain boundaries, and consequently slow boundary diffusion more effectively than a single-doped alloy [129]. Alternatively, Guo *et al.* [104] and Wei *et al.* [153] proposed that co-doped elements may form ionic clusters on alumina grain boundaries that suppress outward Al diffusion physically and chemically.

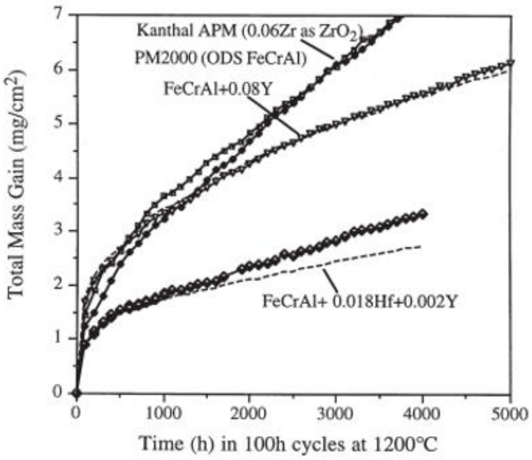

Figure 2.29: Mass gain versus oxidation time for various FeCrAl alloys during 100h cycles at 1200 °C. Reprinted from [129].

2.3.6 Stress Development in Alumina Scales

Much work has focused on the mechanical aspects of oxide scale formation. Stresses develop in the scale during oxidation and can lead to spallation. Thus, understanding how stresses evolve in the growing oxide scale is critical for developing predictive lifetime models. Several types of elastic and inelastic stresses may develop during oxidation. Thermal stresses arise during cooling due to the difference in thermal expansion coefficients between the oxide and the metal substrate. Compressive growth stresses develop during oxidation at high temperature, as evidenced by scale buckling often observed during thermal oxidation [154, 155], and by the lengthening of the metal during oxidation [156, 157]. In an effort to relate stress development, spallation, and scale growth processes, several authors have measured the evolution of stress in alumina scales at different stages of development.

Alumina scales on Ni-based alloys initially experience tensile stresses, before compressive stresses build up over time and eventually level off [61, 158, 159]. Hou *et al.* [61] used synchrotron for *in situ* measurements during oxidation of NiAl alloys and concurrently monitored the intensities of the metastable and α-Al_2O_3 phases (**Figure 2.30**). The initial high tensile stresses corresponded to the transient oxidation stage when metastable θ-Al_2O_3 was still present in the scale. Hou *et al.* proposed that initially compressive stresses develop as θ-Al_2O_3 forms, due to the epitaxial relationship of θ-Al_2O_3 with the NiAl substrate. Then, as α-Al_2O_3 patches nucleate they are put under high tension due to the volume shrinkage from θ- to α-Al_2O_3. Others confirmed that tensile stresses develop during the transient oxidation stage as α-Al_2O_3 patches nucleate and grow through metastable alumina [28, 159]. Once the entire scale transforms to α-Al_2O_3, compressive stresses build as typically observed during oxide growth [61, 154-157, 160]. Most authors agree that the compressive stresses likely develop as a result of new oxide formation within the scale as aluminum and oxygen counter-diffuse along the grain boundaries, as first proposed by Rhines and Wolf [156]. From observations of peak broadening in the photoluminescence spectra, Lipkin *et al.* proposed that a strain gradient was present through the thickness of the scale, possibly due to non-uniform oxide formation [159]. However, no direct experimental evidence shows new oxide growth within alumina scales.

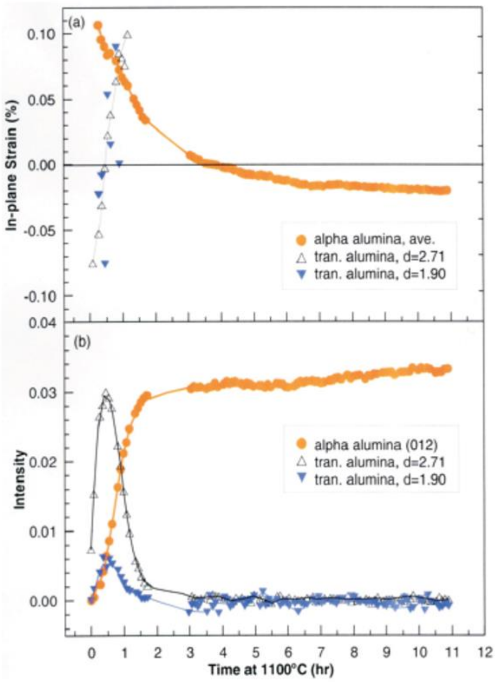

Figure 2.30: a) Stress and b) Al_2O_3 phase intensity as a function of time for alumina grown on Ni-55Al oxidized at 1100 °C. Reprinted from [61].

Stress relief processes are activated when the compressive stress reaches a critical value. Tolpygo *et al.* [157] found that compressive growth stresses built up to a maximum of about -1.2 GPa before decreasing with continued oxidation (**Figure 2.31**). The authors discuss two opposing processes affecting stress development during oxidation: the generation of compressive growth stresses due to oxide formation within the scale, and the relaxation of those stresses by creep in the oxide and metal. Likewise, Reddy *et al.* [161] proposed that plastic deformation or diffusional creep may relieve stress at oxidation temperatures >1000 °C, but found that for oxidation at lower temperature stresses may continue to build. In summary, the current consensus surrounding stress development in alumina scales on Ni-based alloys is as follows. During transient oxidation as alumina goes through phase transformation, the scale is under tension. As the steady-state α-Al_2O_3 scale is established and grows, compressive stress in the oxide builds up. The compressive stress eventually levels off as stress relaxation in the scale occurs.

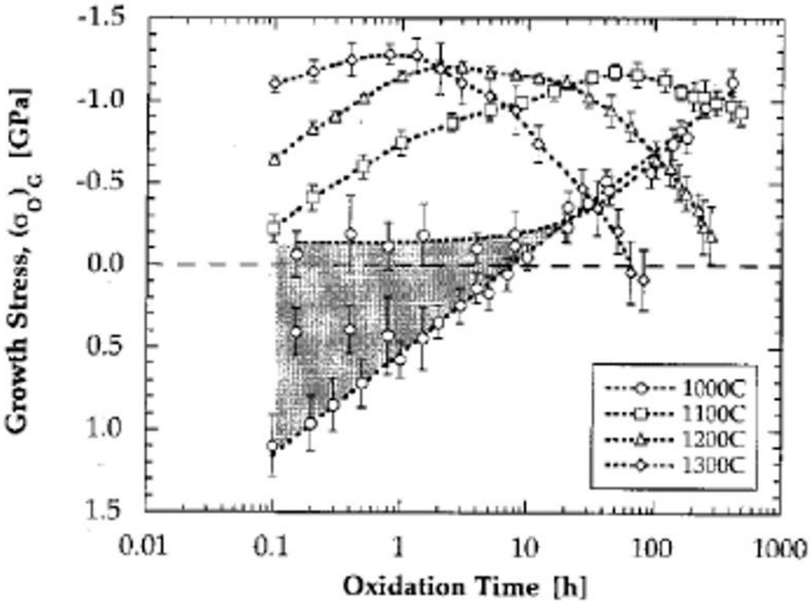

Figure 2.31: Growth stress as a function of time for alumina grown on FeCrAl at various temperatures. Reprinted by permission from Springer Nature: [157].

The scale microstructure is thought to play a significant role in stress development. Scales with long, columnar boundaries will in theory develop higher compressive stresses with the formation of new oxide on the boundaries, as compared to shorter and/or more parallel boundaries, since the oxide is constrained laterally but not vertically [162]. FeCrAl alloys, for example, tend to have thicker scales with long columnar grains and exhibit higher compressive stresses than those on NiAl alloys [163]. In contrast, scales on NiAl are often thinner and consist of more equiaxed grains than scales on FeCrAl alloys at the same oxidation time [158].

Various dopants are known to affect stress development in a growing alumina scale. Additions of yttrium to FeCrAl-based alloys prevent the wrinkling of alumina scales [74] thought to be due to lateral growth of the oxide. Golightly *et al.* [74] postulated that additions of

Y to the alloy prevented formation of oxide on the grain boundaries within the alumina scale by inhibiting outward aluminum diffusion. Consequently, the Y-containing alloy would not exhibit the highly convoluted scale observed on the un-doped alloy. Christensen *et al.* [164] showed that residual compressive stresses on both FeCrAl and NiCrAl-based alloys actually increased with the addition of Y. Likewise, Sarioglu *et al.* [163] observed that doping FeCrAl alloys with Y increased the *in situ* compressive growth stress (-1.7 GPa) in comparison to the un-doped alloy (-1 GPa). The authors suggested that yttrium additions segregate to the scale grain boundaries and reduce new oxide formation at the grain boundaries by limiting upward Al diffusion. They speculated that although reduced boundary oxide formation would normally lead to smaller compressive stresses, Y also inhibits the scale relaxation processes such as creep, allowing the build-up of compressive stress in comparison to the un-doped alloy. Studies on the creep of polycrystalline bulk alumina suggest that Y reduces the diffusional creep rate [139, 165, 166]. Other dopant elements seem to have similar effects. Renusch *et al.* [72] studied FeCrAl alloys with additions of Zr or Hf, finding that residual strain was higher for the scales with dopant additions, indicating Zr and Hf may diminish scale relaxation mechanisms such as creep. Veal *et al.* [167] found that NiAl alloys doped with Zr sustained tensile growth strains even after alumina transformation. In comparison, the un-doped NiAl alloy exhibited high tensile strains during transient oxidation before transitioning to compressive strains in the steady state. The authors suggested that while compressive stresses are typically generated from oxide formation along the grain boundaries after the combination of migrating Al and O ions, tensile stresses may develop from the combination of migrating Al and O *vacancies*. They propose that the addition of a reactive element such as Zr may slow the outward diffusion of Al and thus the formation of oxide along the grain boundaries, allowing the vacancy combination to dominate and leading to the observed tensile stresses.

2.4 Summary of Major Findings, Research Gaps, and Motivation for this Dissertation

The body of work reviewed here on the oxidation behavior of alumina-forming alloys and the effects of dopants illustrates the complexity of high temperature oxide scale growth. Though much progress has been made in understanding some of the mechanisms by which dopants affect oxidation, significant knowledge gaps remain.

In the transient stage of oxidation, metastable Al_2O_3 initially forms on the surface of the alloy before transforming to the stable α-Al_2O_3. The metastable Al_2O_3 phases have faster oxidation kinetics compared to those of α-Al_2O_3 and consequently can quickly degrade the metal and reduce component lifetime due to their fast growth rate. The metastable alumina phases transform to the stable, slow-growing α-Al_2O_3 phase through a nucleation and growth process. It is thought that α-Al_2O_3 nucleates at the oxide-metal interface, and grows radially through the metastable Al_2O_3 layer, forming circular patches. The α-Al_2O_3 patches continue to grow and impinge on one another until the entire Al_2O_3 layer has transformed to α-Al_2O_3. After the transformation is complete, a transition to slower oxidation kinetics occurs. Different dopant elements can have varied effects on the rate of transformation to α-Al_2O_3 and the length of the transient stage of oxidation. Elements such as Mg, Ti, and Si are thought to accelerate, while Y, La, and Hf are thought to slow the transformation to α-Al_2O_3. Ion size and valence are suggested to play a role in how a particular element affects the transformation rate, but further work would be needed to establish the exact mechanism.

There are many unknowns surrounding Al_2O_3 transformations during thermal oxidation. Though often assumed to be at the oxide-metal interface, the nucleation sites of α-Al_2O_3 have not been clearly identified. Although the total length of transient oxidation has been compared for several dopant elements, mechanisms of possible dopant effects remain speculative. Most studies employed bulk measurements of alumina phase evolution, revealing little in terms of microstructural changes and dynamics of the alumina nucleation and growth behavior. For example, the lateral growth rate of α-Al_2O_3 patches through the metastable alumina layer have not been systematically measured and therefore how alloy composition affects α-Al_2O_3 lateral growth rate is not known. It also has been suggested that the transient stage of oxidation may affect steady-state oxidation kinetics by establishing the Al_2O_3 scale grain size. However, no direct link between transient stage behavior and steady-state scale microstructure currently exists.

During steady-state oxidation after the metastable phases transformed, the α-Al_2O_3 scale grows by Al and O diffusion along the scale grain boundaries and new oxide forms at the surface and scale-alloy interface, respectively. Consequently, a dual-layered microstructure develops, with smaller equiaxed grains near the scale surface, and longer columnar grains near the scale-alloy interface. Compressive stress is thought to develop as new oxide forms at the grain boundaries, and as this stress builds up, stress relaxation mechanisms such as creep are activated. Segregation of dopant elements to grain boundaries has been linked to reduced transport of aluminum and oxygen through the scale. Dopants are thought to reduce new oxide formation at the grain boundaries by reducing transport of aluminum and oxygen, thus reducing the build-up of compressive stress. It was also proposed that dopants affect stress relief processes such as creep in the oxide scale, as they are known to influence creep properties in bulk aluminum oxide.

Numerous studies on steady-state oxidation have laid a framework for understanding dopant effects on oxidation behavior, yet many open questions remain. Dopants present on the scale grain boundaries are thought to reduce Al transport. However, the effects of different dopant elements on upward Al and inward O transport have not been quantified, and the mechanisms by which dopants may alter grain boundary transport are not currently understood. Co-doping with combinations of certain elements has demonstrated a beneficial effect on oxide scale growth via reduced oxidation rate. However, the synergistic effect of adding multiple elements is not understood at present. In addition, it is unclear how scale texture and grain boundary misorientation may affect grain boundary transport. Many aspects of how stress is generated in the oxides scale also remain speculative. Most studies speculate that compressive stresses are generated due to new oxide formation along grain boundaries within the growing Al_2O_3 scale, yet this has not been explicitly shown experimentally. It is also thought that stress relaxation such as creep occurs during oxidation, but this is difficult to demonstrate and measure. The presence of dopants on the grain boundaries potentially affects both stress generation and relief in the oxide scale, but neither process is well understood or characterized.

The current work focuses on elucidating some of the above-mentioned dopant effects, verifying the following hypotheses:

- Prior observations found that Ti and Si accelerate, while Y slows the θ- to α-Al_2O_3 transformation during transient oxidation. We propose that the dopants produce these effects by changing the nucleation and lateral growth rate of α-Al_2O_3 to varying degrees.
- We hypothesize that co-doping with Ti+Y and Si+Y has mild effects on θ- to α-Al_2O_3 transformation due to the conflicting accelerating and retarding effects of Ti/Si and Y. Furthermore, we suggest that co-doping accelerates or slows the transformation

depending on the dominance of the individual dopant effects on the nucleation and lateral growth rate of α-Al_2O_3.

- Previous studies suggest that dopants may be more soluble in the relatively “open” structure of metastable Al_2O_3 phases. Thus, we hypothesize that Ti, Y, and Si will be present in higher concentrations in θ-Al_2O_3 compared to α-Al_2O_3, and will segregate to the θ- to α-Al_2O_3 transformation front as the α-Al_2O_3 patches grow and these dopants are rejected from the α-Al_2O_3 phase
- Considering the nucleation/growth aspect of alumina transformation, we hypothesize that the grain size of the steady-state α-Al_2O_3 scale correlates with the nucleation rate of α-Al_2O_3 patches in the transient stage of oxidation.
- Prior studies found that alumina scales on Y-doped alloys tend to exhibit reduced outward growth and scale kinetics. In addition, Y was found to reduce O grain boundary diffusion in bulk polycrystalline alumina. We hypothesize that doping NiAl with Y reduces both Al and O grain boundary transport through the alumina scale during steady-state oxidation, contributing to observed reductions in oxidation rate for Y-containing alloys.
- Previous studies suggested that Ti additions do not have a significant effect on alumina growth kinetics, but may have an effect on O grain boundary diffusion in bulk ceramics. Thus, we propose that Ti will have little effect on Al grain boundary transport during oxidation, but may slightly affect O transport, with no significant effect on scale growth kinetics.

- Co-doping with Ti+Y results in reduced oxidation kinetics, with a greater effect than Ti or Y alone. Therefore, we hypothesize that Ti+Y has a synergistic effect on grain boundary transport, reducing Al and/or O transport to a greater degree than Y or Ti alone.
- Reports of the effect of Si additions on alumina oxidation rate are mixed in the literature, with some suggesting Si accelerates [97, 152] and others suggesting Si slows the kinetics [168-170]. Furthermore, Si is often present as an impurity in bulk Al2O3 and is thought to accelerate grain boundary diffusion [97, 131, 132]. Thus, we hypothesize that Si will accelerate the oxidation rate of α-Al_2O_3 by increasing Al/O grain boundary transport.
- If the above hypotheses are valid for doping with Y and Si alone, we hypothesize that co-doping with Si+Y will result in further reduced alumina kinetics due to a greater reduction in Al/O transport than doping with Si or Y alone.

Model β-NiAl alloys doped with Y, Ti, Si, and combinations of Ti+Y and Si+Y were used to test the above hypotheses. β-NiAl alloys were chosen because they form exclusive Al_2O_3 scales and tend to have longer periods of transient oxidation, simplifying microstructural characterization and Al_2O_3 phase identification. Ch. 3 of this dissertation focuses on clarifying the microstructural changes of the Al_2O_3 scale in the transient stage of oxidation and the effects of Ti-, Y-, and Si-additions. To compare the effects of the different dopant elements on the θ- to α-Al_2O_3 transformation rate, Al_2O_3 scales oxidized from 1-50 hours were characterized using SEM and TEM. Particular attention was placed on measuring each dopant's effect on the nucleation and lateral growth of α-Al_2O_3. The chemical distribution of Ti, Y, and Si with respect to the θ-Al_2O_3 and α-Al_2O_3 phases was also characterized to clarify the mechanisms by which the dopants may affect the nucleation and lateral growth of α-Al_2O_3. Ch. 4 focuses on comparing the effects of dopants on the transport of Al and O along the Al_2O_3 grain boundaries during steady-state oxidation. Outward Al transport was compared for the different dopant elements by measuring the volume of new oxide formed above grain boundaries at the scale surface for each alloy. Inward O transport through the Al_2O_3 scale was investigated for each of the alloys using oxygen isotopic tracer experiments and high-resolution SIMS imaging.

The current work contributes to scientific understanding in the field of high temperature oxidation in addition to providing technological implications. An understanding of the fundamental science behind Al_2O_3 phase transformation during oxidation is needed to enable the design of alloys that can quickly form a protective α-Al_2O_3 layer over a range of temperatures. Elucidating the relationship between transient stage oxidation, steady-state scale microstructure, and steady-state kinetics would enable the development of more accurate predictive models of oxidation kinetics and component lifetime, of great importance for components in industrial settings. Using the knowledge from the current experimental work, more sophisticated models of scale transport and oxidation rate will enable considerably faster development of oxidation-resistant alloys used in a variety of conditions.

CHAPTER 3:

Effects of Minor Alloying Elements on Alumina Transformation During the Transient Oxidation of β-NiAl

3.1 Introduction

Nickel-based alloys are widely used for high temperature structural applications due to their excellent mechanical properties even at temperatures exceeding 800 °C [1, 171]. However, they are also vulnerable to degradation by rapid oxidation at normal use temperatures [172]. To protect against high temperature oxidation, nickel is often alloyed with aluminum to promote the formation of a protective aluminum oxide (α-Al_2O_3) surface layer. The α-Al_2O_3 phase is preferred because the α-Al_2O_3 layer thickens slowly, thus limiting the loss of metal over time [4]. However, the establishment of a continuous protective α-Al_2O_3 layer is not an instantaneous process. For oxidation at temperature ranging from 600-1150 °C, metastable polymorphs of Al_2O_3 often first form during a transient oxidation stage, before transforming into the thermodynamically stable α-Al_2O_3 phase [58]. In comparison to the α-Al_2O_3 phase, the metastable alumina phases have faster growth rates [27], making them less desirable as protective oxides than the α phase. Thus, quantifying Al_2O_3 transformation kinetics and understanding the factors affecting Al_2O_3 transformation rate are of great interest.

β-NiAl forms an exclusive alumina scale during oxidation and provides a relevant example of how the metastable to stable alumina phase transformations take place during the initial stages of Al_2O_3 scale development. During the early stages of oxidation, metastable γ-

Al_2O_3 or θ-Al_2O_3 form a uniform, epitaxial layer on the NiAl substrate, with a whisker or blade-like surface morphology indicative of rapid outward growth [54]. α-Al_2O_3 is thought to nucleate at the oxide-metal interface [55, 61]. The α-Al_2O_3 grains then rapidly grow through the thickness of the metastable Al_2O_3 layer, and expand laterally through the metastable alumina layer, resulting in circular “patches” visible on the oxide surface [27, 28, 30]. Due to the volume shrinkage that accompanies the phase transformation, radial cracks are often observed at the centers of the α-Al_2O_3 patches [28, 30, 58, 62]. Upon further oxidation, the patches continue to grow laterally until they impinge upon one another and the alumina layer is transformed entirely to α-Al_2O_3. The complete transformation to α-Al_2O_3 coincides with a drastic decrease in the oxidation kinetics [30] as the oxidation rate becomes limited by transport along the α-Al_2O_3 grain boundaries [23]. The length of the transient stage depends on a number of factors, including oxidation temperature, surface finish, and alloy composition [6].

Different alloying additions have been found to affect the rate of the alumina transformation to a fully α-Al_2O_3 scale during thermal oxidation. Additions of Y delay the alumina transformation [52, 62, 71, 173], while Ti additions accelerate the transformation and reduce the length of the transient oxidation stage [71, 174, 175]. Similarly, Si additions are thought to accelerate the transformation to α-Al_2O_3 [168, 169]. The overall rate of transformation is a convolution of the nucleation and lateral growth rates of α-Al_2O_3 patches, and whether dopants affect one or both mechanisms remains unknown. Yet, such mechanistic understanding is needed for the design of alloys that rapidly form protective α-Al_2O_3 layers over a range of temperatures [176] and models of alumina oxidation kinetics that account for transient oxidation [177, 178].

To clarify the role of dopants on the transient stage of NiAl oxidation, we characterized the microstructures of the Al_2O_3 scales on a series of oxidized β-NiAl samples that were un-doped or doped with additions of Ti, Y, Si, Ti+Y, and Si+Y. The goal of this study is to determine which aspects of the transient stage of alumina development on NiAl these dopants affect.

3.2 Experimental Details

A single-phase β-NiAl alloy was selected with additions of Ti, Y, and Si to understand the effects of different "reactive" elements, and additional alloys containing combinations of Ti+Y and Si+Y to ascertain any effect of co-doping. Six alloys with nominal compositions listed in **Table 3-1** were obtained from the Ames Laboratory Material Preparation Center, where they were arc-melted and cast into cylindrical rods. The as-received alloys were sectioned, homogenized at 1200 °C in argon gas for at least 20 hours, and subsequently quenched in water. Prior to oxidation, samples were ground with SiC paper using successively finer grit steps through 1200 grit, then polished with 3 and 1 μm diamond slurries. A final polishing step was performed with colloidal silica. Samples were ultrasonically cleaned in ethanol between each consecutive grinding and polishing step. The as-annealed alloys were polycrystalline, with grain sizes ranging from 50-300 μm.

Table 3-1: Nominal alloy compositions in at.%.

ID	**Ni**	**Al**	**Ti**	**Y**	**Si**
NiAl	bal.	42	0	0	0
NiAlTi	bal.	42	1	0	0
NiAlY	bal.	42	0	0.05	0
NiAlSi	bal.	42	0	0	0.5
NiAlTiY	bal.	42	1	0.05	0
NiAlSiY	bal.	42	0	0.05	0.5

Because NiAl grain orientation can have a significant effect on metastable alumina growth and transformation [53, 60, 179], care was taken to compare grains of the same orientation for each alloy at successive oxidation times. Prior to oxidation, electron back scatter diffraction (EBSD) mapping of each sample was performed using a TESCAN MIRA3 FEG scanning electron microscope (SEM) equipped with an EDAX Hikari Camera for EBSD. Sample surfaces were tilted to 70º for data collection and EBSD maps were obtained for each alloy at 30 keV.

For the short-term isothermal oxidation experiments, polished samples were placed in an alumina boat inside a quartz tube furnace. The furnace was heated to 950 °C in flowing Ar, then samples were moved into the hot zone of the furnace, where they reached a steady temperature in approximately 1-2 minutes. Once the samples reached 950 °C, flowing 20% O_2-Ar gas was introduced and samples were oxidized for times ranging from 1 to 15 hours before quenching in air. After initial observations, additional isothermal oxidation experiments were performed for 25 hours for the Ti-, Si- and co-doped alloys, and 50 hours for the Y- and un-doped alloys.

Several techniques were used for phase identification, microstructure characterization, and chemical mapping. Photo-stimulated luminescence spectroscopy (PSLS) was used to identify the alumina phases present in the transient oxidation experiments [28, 180, 181]. PSLS mapping and correlative SEM imaging were done using a TESCAN RISE scanning electron microscope (SEM) equipped with a WITec RISE Confocal Raman microscope. Imaging was done at 10 keV, and PSLS was performed using a 532 nm laser. Surface imaging after the oxidation experiments was accomplished using a TESCAN MIRA3 FEG scanning electron microscope (SEM) at an accelerating voltage of 10 or 20 keV. For image analysis, at least 3 grains oriented with the <011> direction normal to the surface were imaged using the same magnification, and ImageJ software was used for image segmentation to measure the number density, average diameter, and percent of total surface area of the α-alumina patches at each oxidation time. Transmission electron microscopy (TEM) and atom probe tomography (APT) samples were prepared by a standard focused ion beam (FIB) lift-out technique using a Thermo Fisher Helios 650 NanoLab dual scanning electron microscope (SEM)/focused ion beam (FIB). TEM imaging and diffraction were done using a JEOL 2010F analytical electron microscope operated with an accelerating voltage of 200 keV, and additional imaging and energy dispersive spectroscopy (EDS) mapping and analysis were done using a JEOL 2100F scanning transmission electron microscope (STEM) equipped with an EDAX EDS detector and acquisition software, at an accelerating voltage of 200 keV. Atom probe tomography (APT) data collection was performed using a Cameca LEAP 5000HR instrument operated in laser pulsing mode with a pulse energy of 20-30 pJ, a pulse rate of 125 kHz, and a detection rate of 0.5%, with samples cooled to 50K. APT data analysis was done using Cameca IVAS software, version 3.8.2.

3.3 Results

To examine the nucleation and lateral growth behavior of α-Al_2O_3, SEM imaging was used to characterize the surface microstructure, while correlative photoluminescence imaging allowed for Al_2O_3 phase identification on the same area. At each oxidation time, ranging from 1 to 15 hours of oxidation at 950 °C, bright circular "patches" could be seen using secondary electron imaging, while most of the surface was covered by an oxide that appeared darker. A representative image for the NiAlY alloy oxidized for 15 hours is shown in **Figure 3.1**. For all alloys, the surface topography of the darker phase appeared rougher than the bright patches, which appeared smoother near their centers. Using PSLS mapping (**Figure 3.1**), the dark oxide exhibited fluorescence spectra with peaks consistent with those of the θ-Al_2O_3 phase (blue in PSLS mapping), while the bright patches revealed fluorescence spectra consistent with that of the α-Al_2O_3 phase (red). The number density and shape of the α-Al_2O_3 patches were found to depend on substrate grain orientation, so the remainder of the results are presented only for <011> orientated NiAl grains.

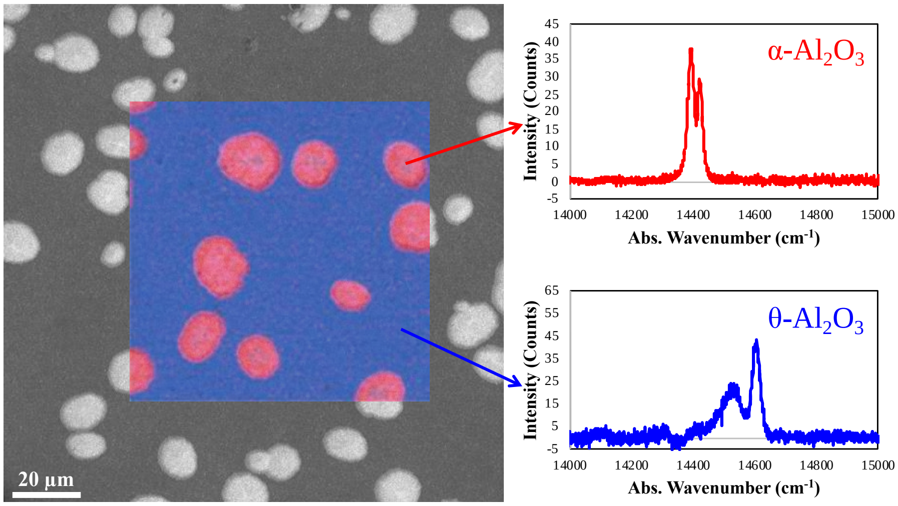

Figure 3.1: SEM surface image of the NiAlY alloy oxidized for 15 hours at 950 °C, with an overlaid PSLS map. Luminescence spectra from the bright and dark regions are shown on the right. Peak positions in the spectra from the bright (red) regions were consistent with those of the α-Al_2O_3 phase, while those in spectra from the dark (blue) region were consistent with that of the θ-Al_2O_3 phase.

Surface SEM images were taken at progressing oxidation times for each alloy (**Figure 3.2**) to compare their patch nucleation and growth behaviors. After one hour of oxidation, both Ti-containing alloys had a few larger α-Al_2O_3 patches and a higher number density of patches compared to the other alloys. Some of the larger patches that had visibly cracked on the Ti-containing alloys often contained nodules of Ti-rich oxide at their centers (for example, NiAlTi at 5h), as evidenced by EDS analysis. After two hours of oxidation, no evolution was noted for the un-doped, Y- and Si-containing alloys. However, many more α-Al_2O_3 patches were present on the Ti-doped alloys. Some patches had grown larger compared to the patches observed after 1 hour. After five hours, a higher density of patches as well as larger patches were noted for the un-doped, Y-, and Si-doped alloys compared to the observations at 1 and 2 hours. Patches also continued to grow on the Ti-containing alloys. After 10 hours, the un-doped and Y-doped alloys had the smallest patches, while the Si and Ti-containing alloys had larger, similarly sized patches. After 15 hours, the Y- and un-doped alloys again showed smaller patches than the other alloys. Patches on the Si- and Ti-containing alloys started to impinge upon each other due to continued growth. Additionally, dark spots can be seen in the SEM images from 1-15 h of the un-doped, Y-, Si-, and SiY-doped alloys, but not on those of the Ti-containing alloys. The spots (**Figure 3.3a**) are associated with faceted interfacial voids present at the oxide-metal interface, as evidenced via cross-sectional imaging (**Figure 3.3b**). The number density and shape of the voids varied with alloy chemistry, grain orientation, and surface finish. No voids were observed on the Ti-containing alloys. On the un-doped, Y-, and Si-doped alloys, a higher density of voids was observed on <111>-oriented NiAl grains and on polishing scratches.

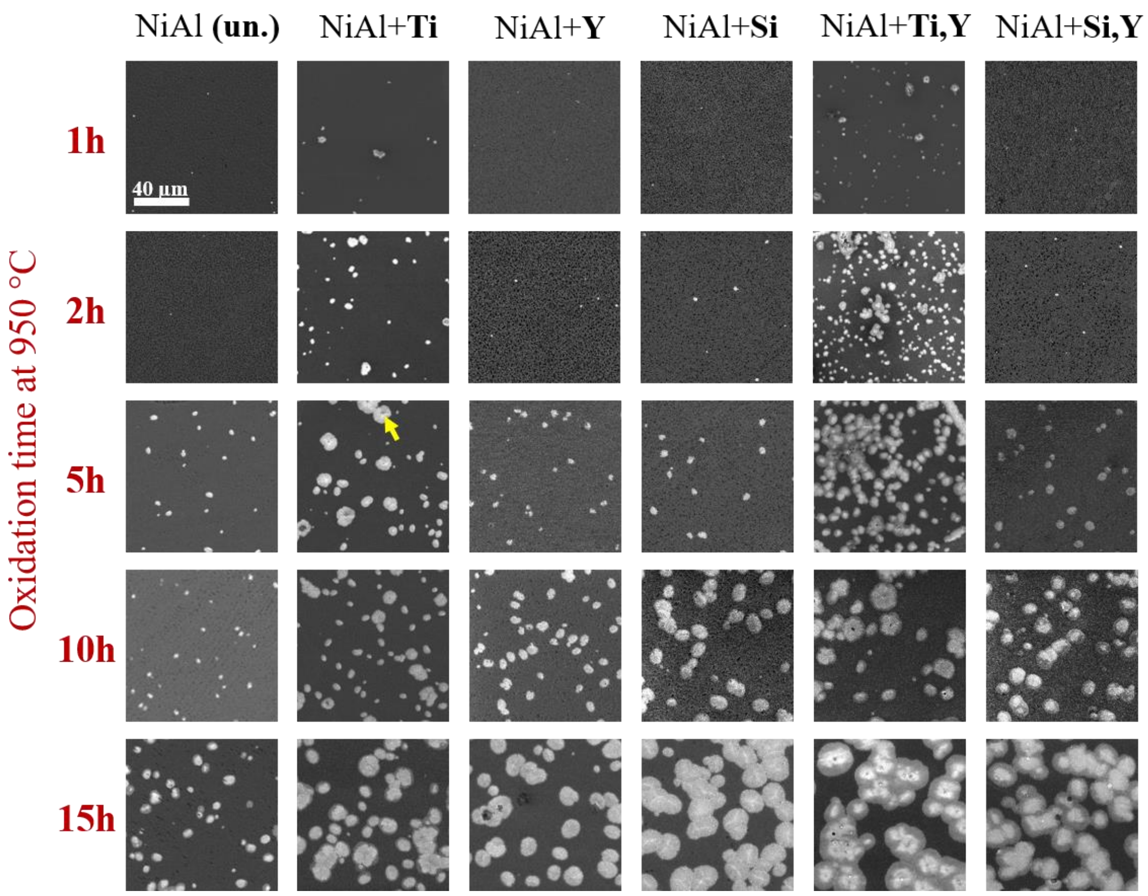

Figure 3.2: SEM surface images after oxidation exposures at 950 °C for 1 to 15 hours. The yellow arrow indicates a nodule of Ti-rich oxide at the center of one of the α-Al_2O_3 patches.

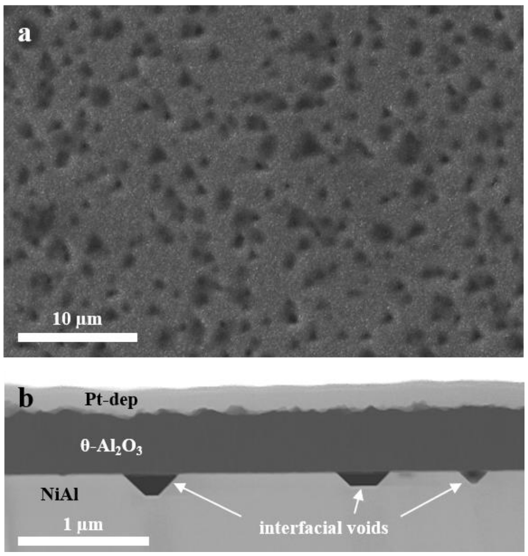

Figure 3.3: a) SEM surface image and b) dark field STEM image of the NiAl alloy oxidized for 10 hours at 950 °C.

The qualitative α-Al_2O_3 patch nucleation and lateral growth behavior was further examined with quantitative image analysis of at least three <011> grains from each alloy; results are summarized in **Figure 3.4**. The overall transformation rate on each alloy was captured via the α-Al_2O_3 surface coverage (**Figure 3.4a**). After 1 hour, only a small fraction of the alloy surfaces (less than 3%) had transformed to α-Al_2O_3. By 5 hours, the α-Al_2O_3 surface coverage remained limited, but was higher on the Ti-containing alloys (8-10%) than on the other alloys (<5%). After 10 hours, the TiY and SiY co-doped alloys showed a significant increase in transformed area, 33 and 25% respectively. The Si and Ti-doped alloys showed a lesser increase in surface coverage to ~19 and 13% respectively. The un-doped and Y-doped alloy still had very low fractions of the total area transformed to α-Al_2O_3, with <8% transformed after 10 hours. By 25 hours, the TiY-doped alloy was nearly entirely transformed to α-Al_2O_3. The Ti-, Si-, and SiY-doped alloys showed about 80% of the surface transformed to α-Al_2O_3. Over twice the time (50 hours) was needed for the un-doped and Y-doped alloys to exhibit similar 80% α-Al_2O_3 coverage. In summary, the transformation to α-Al_2O_3 occurred at a faster rate on Si- and Ti-containing alloys than on the un-doped and Y-doped alloys.

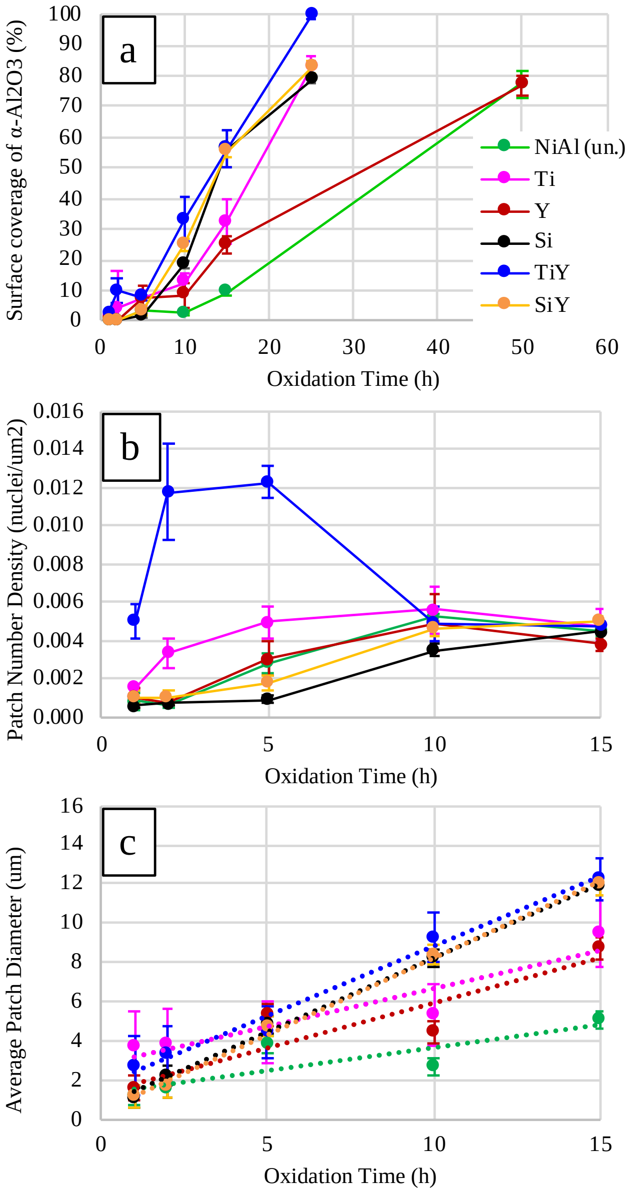

Figure 3.4: Summary of quantitative image analysis of surface SEM images showing a) % of the surface covered by the α-Al_2O_3 phase, b) number density of α-Al_2O_3 patches, and c) average α-Al_2O_3 patch diameter, at consecutive oxidation exposures at 950 °C.

The α-Al_2O_3 nucleation behavior was inferred from the evolution of the number density of patches at consecutive oxidation times **(Figure 3.4b)**. The Ti- and TiY-doped alloys had significant early increase in the number densities of patches between 1 and 5 hours. On the Ti-doped alloy, the patch number density then remained constant, suggesting that no significant additional nucleation took place. The TiY-doped alloy exhibited significantly higher nucleation density that the other alloys from 1-5 hours, but then showed a decrease at 10 and 15 hours to about the same level as the other alloys. The sudden decrease could be due to variability in the oxide grains examined or slight differences in oxidation conditions. Further work would be needed to confirm this unusual result. The number densities on the un-doped and Y-doped alloys steadily increased from 2 to 5 and 5 to 10 hours; reaching comparable values as the Ti-containing alloys by 10 hours. Finally, the Si-containing alloys showed delayed behavior with the most significant increases in the number densities between 5 and 10 hours.

The lateral growth rate of α-Al_2O_3 was then compared for each alloy by measuring the average α-Al_2O_3 patch diameter at successive oxidation times (**Figure 3.4c**). After 1 hour, the Ti-containing alloys exhibited larger patches with diameters, around 4 µm, compared to all other alloys with patch diameters around 1 µm. As oxidation progressed, the average α-Al_2O_3 patch size on the Y-, and Ti-doped alloys increased slightly faster than that on the un-doped alloy. The Si- and TiY- doped alloys had significantly higher rates of lateral patch growth, and after 15 hours, the Si-containing alloys and TiY-doped alloy had the largest α-Al_2O_3 patches compared to the other alloys. Consequently, Y, Ti, and Si increase lateral growth rate of α-Al_2O_3, with Si exhibiting the strongest effect.

In search for mechanisms explaining the changes in nucleation and growth rates, we hypothesized that the dopants may elicit differences in the θ-Al_2O_3 microstructure and/or the structure of the θ-α transformation front. Cross-section TEM lift-outs were examined from each of the alloys on <011>-oriented grains after 10 hours of oxidation at 950 °C. The θ-Al_2O_3 microstructure was found to be similar for all the alloys, and a representative bright-field STEM image is shown in **Figure 3.5a**. Near the oxide metal interface, the θ-Al_2O_3 was observed to consist of a layer of discrete, nano-crystalline grains, as evidenced by the rings in the diffraction pattern (**Figure 3.5b**) that were consistent with the d-spacing of the θ-Al_2O_3 phase. Toward the surface of the θ-Al_2O_3 layer, elongated lathe-like grains were visible. A diffraction pattern from this region (**Figure 3.5c**) showed textured rings that had d-spacings consistent with θ-Al_2O_3, and contained streaking perpendicular to the lathes. Spacing between the streaks was consistent with the d-spacing in the <001> direction of the θ-Al_2O_3 phase. Both the nano-crystalline grains and lathe-like grains can be seen clearly in the dark-field STEM image shown in **Figure 3.5d**.

While the θ-Al_2O_3 layer exhibited comparable microstructure, its thickness varied with alloy composition. **Figure 3.6** shows a comparison of the θ-Al_2O_3 layer on the un-doped, Ti-, Y-, and Si-doped alloys, along with a plot of the θ-Al_2O_3 thickness. The Si- and SiY-doped alloys exhibited the thickest θ-Al_2O_3 layers, followed in decreasing thickness by the TiY-, Y-, Ti-, and un-doped alloys.

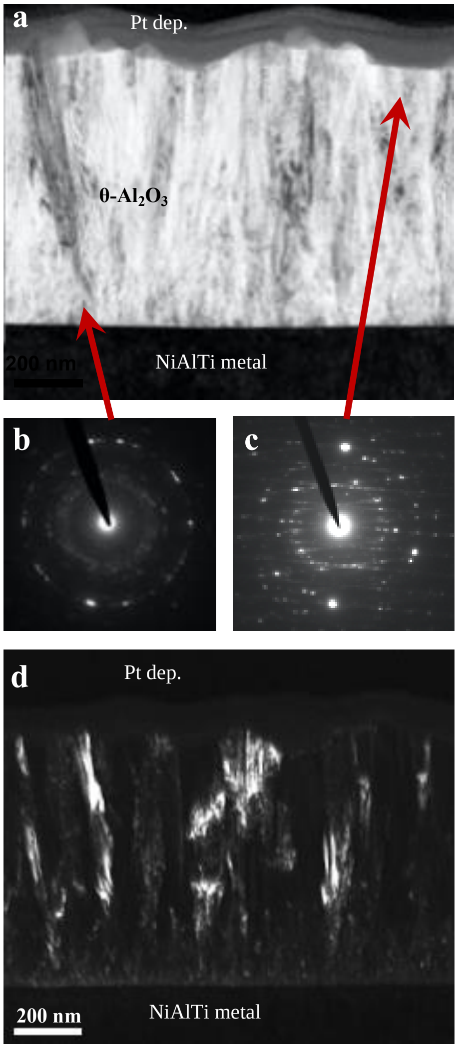

Figure 3.5: NiAlTi alloy oxidized for 10 hours at 950 °C. a) Bright-field image of the θ-Al_2O_3 layer in cross-section. c) Selected area diffraction pattern from a region near the θ-Al_2O_3-metal interface. d) Selected area diffraction pattern from a region near the θ-Al_2O_3 layer surface. b) Dark-field TEM image of the same area.

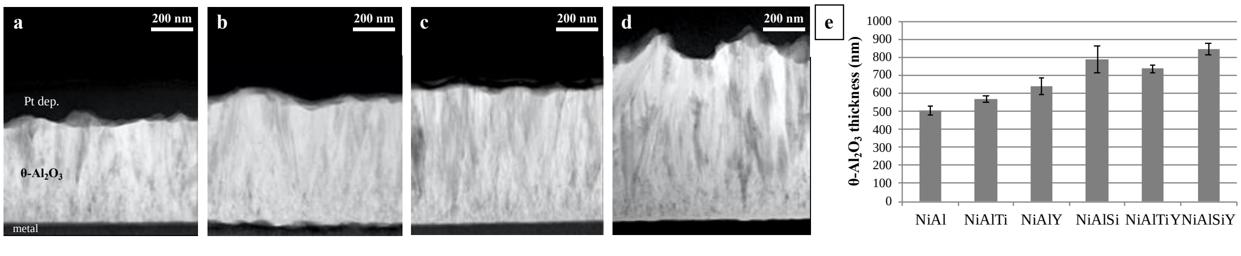

Figure 3.6: Bright-field TEM images of the θ-Al_2O_3 layer in cross-section on the a) NiAl, b) NiAlTi, c) NiAlY, and d) NiAlSi alloys oxidized for 10 hours at 950 °C. e) θ-Al_2O_3 layer thicknesses after 10 hours of oxidation at 950 °C.

The growth of the α-Al_2O_3 through the θ-Al_2O_3 layer in cross-section was similar for all of the alloys. A representative cross-section through an α-Al_2O_3 patch on the TiY-doped alloy is shown in **Figure 3.7**. Diffraction patterns from the bright grain visible at the right of the image were consistent with the α-Al_2O_3 phase and revealed that the patch had nucleated and grown as a single crystal. In some cases where patches had already cracked, grain boundaries were observed, with slightly misoriented α-Al_2O_3 sub-grains. On all alloys, the α-Al_2O_3 patches were slightly wider laterally near the top surface of the scale than at the oxide-metal interface. In the surface SEM images (**Figure 3.2**) the slightly darker contrast visible around the edge of some of the patches (for example NiAlTiY at 15 hours) is thought to be the result of both θ- and α-Al_2O_3 present through the scale thickness, thus giving different contrast in SEM than the patch centers, which consist entirely of α-Al_2O_3. The α-Al_2O_3 patches were also observed to be thinner in cross-section near their centers than at the patch edges due to both volume contraction and slower growth rate of the α-Al_2O_3 phase compared to θ-Al_2O_3.

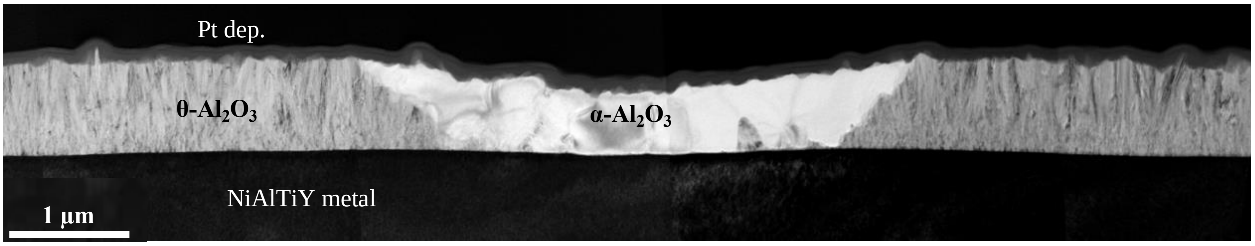

Figure 3.7: Bright-field cross-section TEM image of the NiAlTiY alloy oxidized for 10 hours at 950 °C showing the θ-Al_2O_3 layer and an α-Al_2O_3 patch.

Observing that θ- and α-Al_2O_3 microstructure was similar for each of the alloys, we next examined potential differences in chemistry of the alumina scales. Using STEM-EDS mapping no detectable levels of Y, Ti, and Si were observed in either the θ- or α-Al_2O_3 phase. APT analyses also showed Ti and Y levels that were below the instrument detection level in both the θ- (**Figure 3.8)** and α-Al_2O_3 phase (**Figure 3.9**). EDS maps were also collected on several areas that included the θ-Al_2O_3 layer, the θ/α-Al_2O_3 interface, and the oxide-metal interface under both the θ- and α-Al_2O_3 on each alloy. No Y or Si segregation was observed at any of the interfaces. On the Ti- and TiY-doped alloys however, a somewhat continuous layer of Ti-segregation at the oxide-metal interface was observed after a short 30 minute exposure (**Figure 3.10**). After 10 hours, discrete Ti-rich regions were observed at the oxide-metal interface under both the θ- and α-Al_2O_3, shown in **Figure 3.11**.

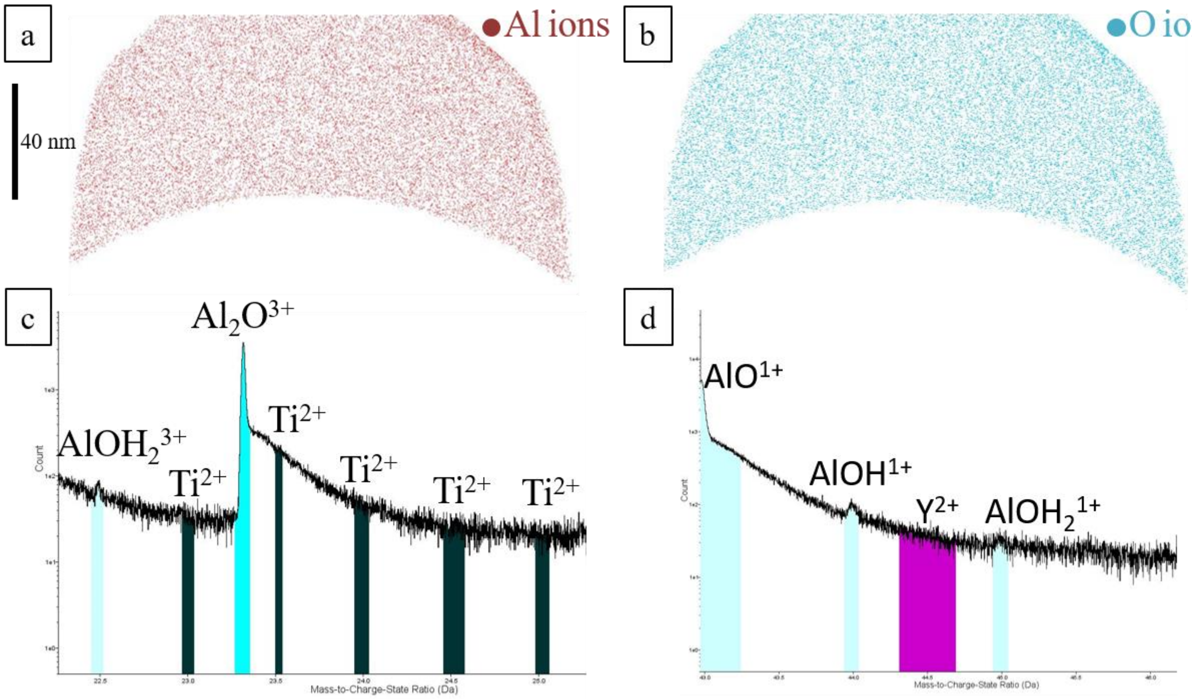

Figure 3.8: APT reconstruction of a volume prepared from the θ-Al_2O_3 phase after 30 minutes of oxidation at 950 °C. a) Al ions are shown in red and b) O ions are shown in blue in a 20 nm thick slice. The mass spectrum revealed minimal peaks for a) Ti and b) Y.

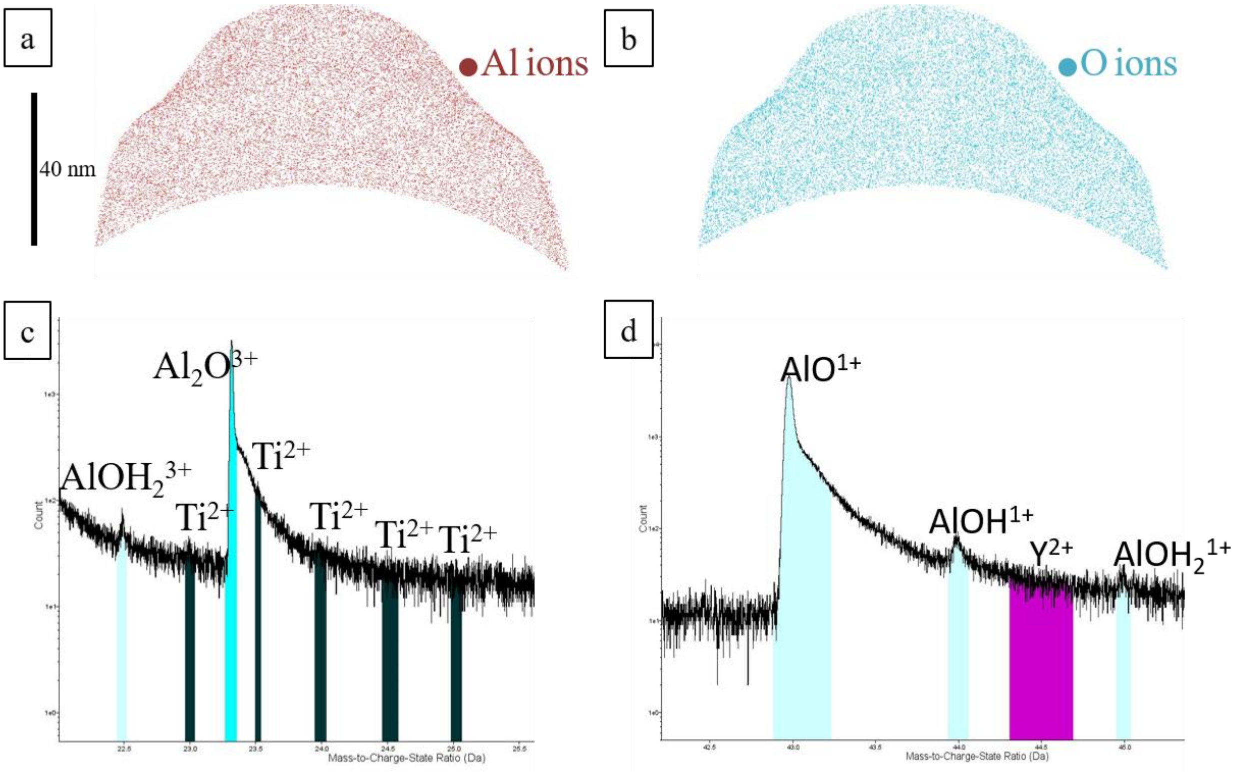

Figure 3.9: APT reconstruction of a volume prepared from the α-Al_2O_3 phase after 30 minutes of oxidation at 950 °C. a) Al ions are shown in red and b) O ions are shown in blue in a 20 nm thick slice. The mass spectrum revealed minimal peaks for a) Ti and b) Y.

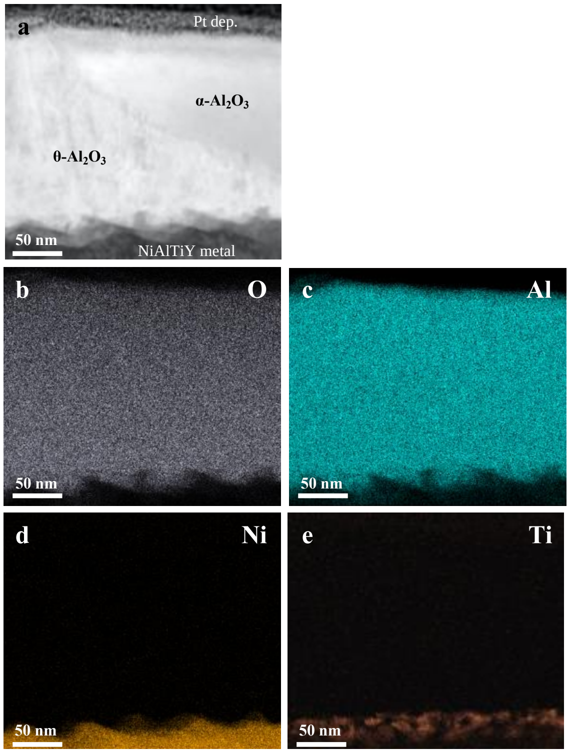

Figure 3.10: STEM-EDS maps of the NiAlTiY alloy oxidized for 30 minutes at 950 °C. a) Bright-field STEM image of the θ-α-Al_2O_3 interface, with corresponding elemental maps showing the distribution of b) oxygen, c) aluminum, d) nickel, e) titanium.

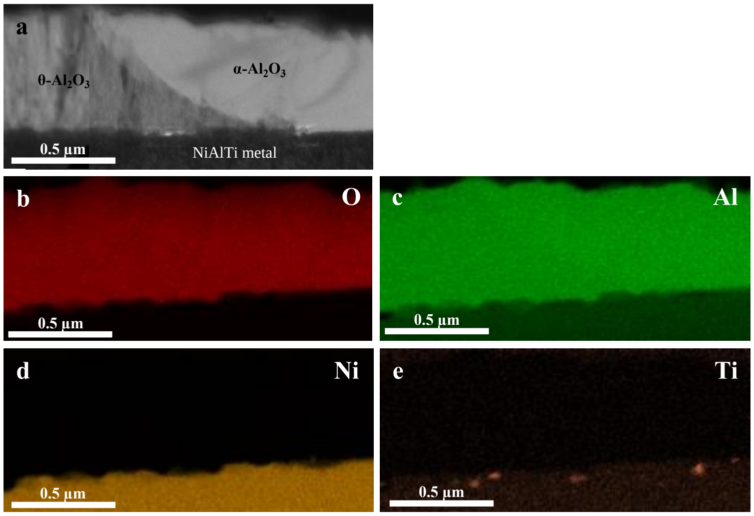

Figure 3.11: STEM-EDS maps of the NiAlTi alloy oxidized for 10 hours at 950 °C. a) Bright-field STEM image of the θ-α-Al_2O_3 interface, with corresponding elemental maps showing the distribution of b) oxygen, c) aluminum, d) nickel, e) titanium.

3.4 Discussion

It is well established that dopant elements can significantly reduce the oxidation rate of alumina-forming alloys. The majority of the prior studies on this topic focused on the effect of dopants on the steady-state oxidation stage, i.e. changes Al and O transport along the grain boundaries during oxidation. However, as demonstrated here and in previous literature, dopants also can have significant effects on the transient oxidation stage. The prolonged growth of metastable alumina in the transient stage can deplete the alloy of aluminum, a significant problem for thin-walled components at intermediate temperatures (~800-1000 °C). Thus, understanding how various dopants change the length of transient oxidation is of technological importance.

The overall oxide morphology and its evolution with time observed on all alloys of the current study are consistent with literature on the transient oxidation of NiAl alloys [27, 28, 53, 77]. An initial metastable alumina layer precedes the nucleation and radial growth of α-Al_2O_3. The initial θ-Al_2O_3 layer has a rough, blade-like appearance due to the rapid outward growth of the metastable phase [51, 54, 55]. When the transformation to α-Al_2O_3 occurs, the rapid outward growth of θ-Al_2O_3 ceases and surface diffusion smooths out the blade-like topology [28, 59]. Thus, α-Al_2O_3 patches within the θ-Al_2O_3 layer are smoother near their centers where the transformation to α-Al_2O_3 first takes place.

While the scales on all of the NiAl alloys shared these common features, they also differed by the nucleation and growth rates of the α-Al_2O_3 patches. The present results suggest that Ti and Si accelerate the transformation, in agreement with prior literature [71, 168, 169, 174, 175]. Our findings also suggest that Y has minimal effect on the transformation, contrary to prior results [52, 62, 71, 173]. Since the rate of transformation of the θ-Al_2O_3 layer to a fully α-Al_2O_3

scale is controlled by the nucleation and the lateral growth rate of α-Al_2O_3 patches, it is worth noting that dopants affect nucleation and growth differently.

Si retards the onset of nucleation and accelerates lateral growth. The longer incubation time in the presence of Si is consistent with Si acting to stabilize the metastable Al_2O_3 phase and decrease the driving force of the θ-α transformation [182, 183]. Because Si-containing alloys exhibited the thickest θ-Al_2O_3 layers, Si also accelerated the growth of θ-Al_2O_3, which is dominated by the outward diffusion of Al cations [51]. Prior work showed that minute levels of dopants can dramatically affect the concentration of intrinsic defects in α-Al_2O_3 [184]. If Si^{4+} cation substitutes for Al^{3+} in the θ-Al_2O_3 phase [182], charge neutrality requires additional cation vacancies to form, promoting faster diffusion of Al cations than in un-doped θ-Al_2O_3, and explaining the faster outward growth of the θ-Al_2O_3 layer observed on the Si-doped alloy. A significant assumption here is the presence of Si in the scale, which we could not confirm. Nonetheless, the increased concentration of cation vacancies in the Si-doped scale could conceivably accelerate the transformation from θ- to α-Al_2O_3, since the transformation is diffusion-controlled [47, 48] and involves the structural re-arrangement of Al atoms [39, 41].

Ti and Y also have a slight tendency to accelerate lateral growth, and TiY-doping had a significant effect. The slight acceleration of the lateral α-Al_2O_3 growth in the presence of Y and Ti compared to Si may be due to smaller changes in the cation vacancy concentration, which are less expected for Y and Ti since large Y^{3+} ions typically substitute for Al^{3+} with the same charge state, and Ti can coexist as Ti^{4+} or Ti^{3+} in alumina depending on the oxygen partial pressure [185, 186]. The significant effect of co-doping with Ti+Y on lateral α-Al_2O_3 growth is not understood at present. However, the TiY-doped alloy, like the Si-containing alloys, had a thicker

θ-Al_2O_3 layer than the undoped alloy. Therefore co-doping accelerated both θ-Al_2O_3 growth and the θ-α transformation, suggesting a similar mechanism involving defect concentrations.

Unlike Si, Ti appears to promote early nucleation. After just 30 minutes, a Ti-rich layer was observed at the alumina-metal interface of the TiY-doped alloy. It may be a thin Ti-based oxide phase because of the presence of an oxidizing atmosphere, however it was not confirmed. One possible explanation for increased nucleation seen on the Ti-doped alloys is that the potential Ti oxide layer functioned as a seed layer for α-Al_2O_3, promoting α-Al_2O_3 nucleation. Such template layers have previously been reported for Cr- and Fe-containing alloys [27, 72, 187] that can form an initial layer of $(Cr,Fe)_2O_3$ that is isostructural with Al_2O_3. In the present case, Ti_2O_3 is isostructural with Al_2O_3, however other Ti oxide phases could form as well, and further evidence is needed to support this mechanism. At longer oxidation times, the continuous Ti-rich layer was no longer observed, possibly due to its destabilization and incorporation into the thickening Al_2O_3 layer. The disappearance of the Ti-rich layer is also consistent with a decrease in the nucleation rate at longer oxidation times.

An additional feature of the Ti-containing alloys was the absence of interfacial voids. Faceted interfacial voids have been widely observed upon the oxidation of NiAl alloys and are thought to occur by vacancy injection and coalescence [53, 77, 81, 85, 86]. As aluminum selectively oxidizes to form Al_2O_3, the alloy becomes depleted of Al while vacancies are formed at the oxide metal interface. The resulting surplus nickel at the oxide-metal interface diffuses back into the alloy, leaving additional vacancies at the interface. For Al-lean NiAl alloys, the diffusivity of nickel is larger than that of aluminum [188] and the flux of Ni back into the alloy exceeds that of Al. This flux imbalance allows vacancies to coalesce into large interfacial cavities underneath the rigid surface oxide [81]. There are several possible mechanisms by which

Ti may be suppressing these interfacial voids. Ti additions in NiAl may change the diffusivity of Ni or Al such that they are approximately equal, i.e. increasing the diffusivity of Al or decreasing the diffusivity of Ni. In Pt-containing NiAl for example, Pt suppresses interfacial void formation by increasing the aluminum diffusivity [90]. In the case of Ti additions, no evidence from literature could be found suggesting that it alters the Al or Ni diffusivity. Using wavelength dispersive spectroscopy (WDS), we also verified that the depletion distance of Al beneath the scale was essentially the same on both the un-doped NiAl alloy and the Ti-doped NiAl. From the oxide thickness observations, Ti is also not reducing the growth rate of θ-Al_2O_3, which would reduce the formation of vacancies at the scale-alloy interface. A more likely explanation for the lack of voids comes from the observation of the Ti-rich layer at early oxidation times. Under the assumption that this layer is a Ti-based oxide, its formation would be accompanied by an increase in volume, since Ti-based oxides and suboxides are less dense than NiAl [189, 190]. Vacancies at the oxide-metal interface formed during the growth of Al_2O_3 could conceivably be annihilated upon the formation of the Ti-based oxide layer at the interface.

Y had no conclusive effect on alumina transformation, in contrast with previous literature reporting that Y hinders the metastable Al_2O_3 to α-Al_2O_3 transformation [52, 62, 71, 173]. The majority of these studies, however, utilized either implanted Y or larger alloying additions of Y in comparison to the current study, which could explain the lack of any obvious effect. The alloys co-doped with Ti+Y and Si+Y behaved similarly to the single-doped Ti- and Si-doped alloys, respectively, consistent with the observation that the Y-addition had little effect on the θ- to α-Al_2O_3 transformation.

3.5 Conclusions

We presented results that clarify the effect of several dopant elements on the nucleation and growth behavior during transient stage alumina phase transformation. The following conclusions were reached:

- Ti, Si, and Y doping had no effect on the microstructure of the θ-Al_2O_3 layer.
- Doping NiAl with Ti accelerated the θ to α alumina transformation by reducing the incubation time for nucleation and increasing nucleation rate.
- On the Ti-containing alloys, a Ti-rich layer was detected at the oxide-metal interface at the shortest oxidation times, but no segregation or partitioning of the dopants was otherwise observed.
- Doping NiAl with Ti suppressed interfacial void formation.
- Doping NiAl with Si accelerated the θ to α alumina transformation by accelerating the lateral growth rate of α-Al_2O_3, despite slightly increasing the incubation time for nucleation compared to the un-doped alloy.
- Ti, Si, and Y doping accelerated the outward growth of θ-Al_2O_3, with Si having the most significant effect.
- The addition of Y had little effect on the overall transformation rate.
- Co-doping with Ti+Y accelerated the overall transformation to α-Al_2O_3 by increasing both nucleation rate and lateral growth rate of α-Al_2O_3.
- Co-doping with Si+Y had no additional effect on the transformation rate compared to doping only with Si.

Finally, our results indicate that the length of transient oxidation can be tuned with the addition of various dopant elements. This has implications for both alloy design and modelling oxidation kinetics. Understanding how certain dopants reduce the length of transient oxidation may enable the design of alloys that quickly form a protective α-Al_2O_3 scale over a range of temperatures. Measurements of nucleation and lateral growth rate of α-Al_2O_3 during transient oxidation are needed to develop more accurate predictive models of oxidation kinetics and component lifetime. Future work is underway to ascertain any relationship between behavior during transient oxidation (for example the nucleation rate), steady-state scale microstructure and grain size, and steady-state oxidation kinetics.

CHAPTER 4:

Dopant Effects on Transport Through Thermally Grown α-Al_2O_3 Scales on NiAl

4.1 Introduction

Nickel-based alloys continue to play an essential role in components used at high temperatures due to their superior mechanical properties. However, aggressive oxidation can quickly jeopardize the integrity of components despite excellent alloy strength, toughness, and creep resistance [171, 172]. With the right alloy composition and oxidation conditions, a continuous, adherent layer of α-Al_2O_3 can form on the alloy surface [3]. Al_2O_3 is very stable and tends to grow more slowly than other oxides, and thus it is able to protect the underlying alloy from excessive degradation [4].

Small improvements in reducing oxidation rate and spallation of protective aluminum oxide scales can make a substantial difference in increasing the useful lifetime of a high temperature component [144]. The addition of small amounts of "reactive" dopant elements such as Y, Hf, and Zr to the alloy is a well-establish path to improve the oxidation behavior of Al_2O_3, and several reviews are available on the topic [7-9, 116]. Reactive dopants enhance the selective oxidation of Al, reduce the oxidation rate of Al_2O_3 significantly, and improve adhesion of the Al_2O_3 scale to the alloy. Hereafter we focus on the contribution of reactive elements to reducing oxidation rate and growth of α-Al_2O_3.

Reactive elements are thought to reduce the alumina oxidation rate by limiting the transport of Al and O through the scale. The growth of α-Al_2O_3 occurs by cation and anion diffusion along the oxide grain boundaries [23]. Cations from the alloy diffuse upward to react at the surface with oxygen, and anions from the gas diffuse down to react at the oxide-alloy interface. In the presence of reactive elements, outward Al transport is reduced and growth of the alumina layer becomes dominated by inward growth via oxygen diffusion [56, 98, 117, 118]. The extent to which Al diffusion is reduced depends on the reactive element [99], and to date there is no accepted mechanism that explains these variations. Furthermore, co-doping with multiple elements seems to reduce oxidation rate even further, suggesting synergistic effects on scale transport [104, 129, 144]. Prior literature extensively used commercial alloys with many alloying additions [99, 148, 151, 191-193], presenting a challenge in isolating the effects of individual elements or interactions between two elements. Finally, the segregation of dopants to grain boundaries and interfaces throughout Al_2O_3 scales, consistently reported for a large range of alloys [97, 194-199], has been linked to reduction in Al diffusion [97, 98, 195]; but the atomistic mechanisms have yet to be elucidated.

Because transport occurs along grain boundaries, it is also important to consider how reactive elements might affect scale grain size. Indeed, oxidation rate is inversely related to scale grain size [108, 109]. It was suggested that scale grain size depends on the early stages of scale formation [28, 63, 64], though no direct experimental evidence is currently available. After longer oxidation times, the alumina scale on un-doped alloys typically exhibits a dual-layered structure, with smaller equiaxed grains near the scale surface from cation outward diffusion and elongated columnar grains closer to the alloy from anion inward diffusion [99]. In the presence of reactive elements, the alumina scale consists mostly of long columnar grains [98], due to the dominance of anion inward diffusion. On FeCrAlY alloys, increasing alumina grain size from the surface to the scale-metal interface was thought to be responsible for the decrease in oxidation rate over time [100]. Alternatively, it was also suggested that some dopants, such as Cr, may reduce scale grain size [64, 108], increasing scale growth rate. However, there is no systematic understanding of how different dopants affect scale grain size, either during the initial stages of scale formation or during steady-state oxidation. Furthermore, since oxidation is conducted at high temperatures, it is conceivable that diffusion-mediated mechanisms would take place. Grain growth and creep are known to be significantly affected by the presence of reactive elements in bulk polycrystalline α-Al_2O_3 [138, 139, 200]. However, there is insufficient data in literature to determine to what degree thermally activated grain growth occurs in α-Al_2O_3 scales during oxidation.

In summary, while it well accepted that some dopant elements reduce alumina grain boundary transport, their contributions on transport or grain size have not been quantified. In this study, Ti and Y were selected due to their varied effects on oxidation rate reported in literature. Y additions significantly reduce alumina oxidation rate [8, 97, 128, 201, 202], while Ti additions have little to no effect [97, 203-205]. In addition, co-doping with Y+Ti seems to reduce the oxidation rate more than doping with Y or Ti alone [152, 206]. To isolate the roles of Ti and Y additions, the microstructures and transport through alumina scales on un-doped NiAl and NiAl with additions of Ti, Y, and Ti+Y, were compared during oxidation at 1200 ^{o}C. We assessed outward alumina transport by measuring new oxide formed above the scale grain boundaries. We then analyzed inward oxygen transport using 2-stage isotope tracer experiments and high-resolution SIMS imaging. The individual and combined effects of Y and Ti on Al and O transport are discussed in the context of their overall effects on oxidation rate.

4.2 Experimental Details

4.2.1 Sample Preparation

Four different alloys were considered, and their nominal compositions are listed in **Table 4-1**. Dopant levels were chosen to avoid formation of Ti and Y oxides in and below the Al_2O_3 scale based on observations from prior literature [129, 152, 206]. Cast cylindrical rods of each alloy were obtained from the Ames Laboratory Material Preparation Center. The as-received alloys were sectioned, encapsulated in argon gas, and annealed at 1200 °C for at least 20 h to ensure a homogeneous composition and microstructure. After annealing, sample surfaces were ground with 320, 600, 800, and 1200 grit SiC paper, then polished with 3 and 1 μm diamond slurries. Samples were ultrasonically cleaned in ethanol between each consecutive grinding and polishing step. The homogenized alloys were polycrystalline, with grain sizes ranging between 80 and 300 μm.

For the isothermal oxidation experiments, samples were placed in an alumina boat inside a quartz tube, then heated to 1200 °C in high-purity Ar. Once at temperature, O_2 gas was introduced and samples were oxidized in a 20% O_2-Ar atmosphere for the specified time before quenching in air. Weight gain measurements during oxidation at 1200 °C for 100 hours in a 20% O_2-Ar atmosphere were recorded using a Netzsch STA 449 F3 Jupiter.

Table 4-1: Nominal alloy composition in at.%.

ID	Ni	Al	Ti	Y
NiAl	bal.	42	0	0
NiAlTi	bal.	42	1	0
NiAlY	bal.	42	0	0.05
NiAlTiY	bal.	42	1	0.05

4.2.2 Outward Aluminum Transport Experiment

Experiments to measure the outward Al transport through alumina scales were designed after Refs. [99] and [207]. NiAlTi, NiAlY, and NiAlTiY were pre-oxidized for 100 h at 1200 °C in 20% O_2-Ar atmosphere order to grow 3-5 μm thick Al_2O_3 scales. NiAl exhibited extensive spalling under these oxidation conditions, so it was pre-oxidized for 1 h at 1200 ºC in order to grow a thinner scale that maintained contact with the alloy. The scales were observed in TEM to have the expected equiaxed-columnar microstructure, but tended to have large local variations in thickness, due to the much higher growth rates near grain boundaries, as reported previously [28]. The top equiaxed portion of the alumina was removed by mechanical polishing using 3 and 1μm alumina lapping films to ensure a flat surface, followed by a final polish with 0.25 μm diamond slurry. Re-oxidation times were determined experimentally and were chosen such that new oxide ridges were thick enough to reduce error in the AFM profile measurements, but thin enough that the ridges did not impinge on each other. NiAlY and NiAlTiY were re-oxidized for 40 h, NiAlTi for 2 h, and NiAl for 0.5 h at 1200 ºC.

Atomic force microscopy (AFM) was performed using a Veeco Dimension Icon AFM in ScanAsyst mode. AFM scans were taken at several locations on the surface each alloy after re-oxidation, taking care to avoid areas of exposed metal. Scans were 10×10 μm in size, and were sampled at 512 lines per scan with a scan rate of 0.567 Hz. The AFM data was processed using NanoScope software, and volume of the new oxide ridges was measured using the "bearing analysis" feature.

Oxide thickness was measured for each AFM scan by milling local cross-sections using focused ion beam (FIB) and taking images using scanning electron microscopy (SEM), on a FEI Helios 650 Nanolab SEM/FIB. Thickness was determined using image segmentation to measure the cross-sectional area of the alumina scale and dividing by the length of the cross-section to get an average thickness, making sure to correct for the angle of the SEM beam to the cross-section surface.

The outward Al grain boundary flux per unit length of grain boundary per unit time was estimated using:

$$J_{GB}^{Al} = \frac{N_{GB}^{Al}}{L_{GB}\Delta t} \tag{1}$$

where N_{GB}^{Al} is the number of Al atoms in the new oxide, L_{GB} is the grain boundary length per unit surface area, and Δt is the re-oxidation time. The numerator, N_{GB}^{Al}, can be written as:

$$N_{GB}^{Al} = \frac{V_{ridge}}{V_{UC}} N_{UC}^{Al} \tag{2}$$

where V_{ridge} is the measured volume of new oxide in the surface ridges, V_{UC} = 2.54 x 10^{-22} cm^3 [208] is the hexagonal unit cell volume of Al_2O_3, and N_{UC}^{Al} = 12 is the number of Al atoms per unit cell.

A diffusional dependence was assumed in the form of Fick's law:

$$J_{GB}^{Al} = -\delta D_{GB}^{Al} \frac{\Delta c}{h} \propto \frac{D_{GB}^{Al}}{h} \tag{3}$$

where δ is the grain boundary width, D_{GB}^{Al} is the diffusivity of aluminum along the grain boundary, Δc is the difference in aluminum concentration from the top of the grain boundary to the bottom, and h is the scale thickness. Following the approach outlined in [99], we assumed that δ and Δc are comparable for all alloys, and differences in the Al grain boundary diffusivity were then estimated by plotting the calculated Al grain boundary flux against the scale thickness.

4.2.3 Inward Oxygen Transport Experiment

To ascertain the effect of dopants on inward oxygen transport, two-stage isotopic tracer experiments were performed. Samples were first oxidized in a 100% O_2 (99.76% ^{16}O natural abundance) atmosphere in order to grow alumina scales that were roughly 2 μm thick. To reach this thickness, different oxidation times were used for each alloy, reflecting their different oxidation rates. NiAl and NiAlTi were oxidized for 15 and 18 hours, respectively, while NiAlY and NiAlTiY were oxidized for 26 hours.

The second oxidation step was executed in one of two ways, using either a resistive heating (for 1h oxidation times) or an encapsulation set-up (for longer oxidation times, >1h). Using the resistive heating set-up, the sample chamber was purged several times in Ar prior to heating and oxidation. Current was then passed through the sample, bringing it to a stable temperature at 1200 ºC in less than 1 minute. Each (pre-oxidized) sample was then exposed to a 97% $^{18}O_2$ atmosphere at just over atmospheric pressure for 1 hour before cooling, which again took less than 1 minute once current through the sample was turned off. For oxidation times longer than 1 hour, an encapsulation method was used. Pre-oxidized samples were encapsulated in $^{18}O_2$ (97% enrichment) and subsequently heated in a furnace to 1200 ºC, reaching temperature in about 2 minutes. All alloys were oxidized in $^{18}O_2$ for 20 hours before quenching in water. After the second stage of oxidation in $^{18}O_2$, cross-sections of each sample were prepared using a standard FIB lift-out technique on a FEI Helios 650 Nanolab SEM/FIB. The distributions of ^{18}O and ^{16}O within the cross-sections were mapped using a Cameca NanoSIMS 50, operating with a Cs^+ beam with a current of ~0.2 pA with a spot size of ~50 nm. The secondary mass spectrometer was tuned for ~3000 mass resolving power [209], and the ions of interest were quantified on electron multipliers using pulse counting: the two oxygen isotopes, $^{16}O^-$ and $^{18}O^-$, as well as $^{12}C^-$ to note the position of the Pt deposited on the surface of the alumina during the lift-out process. 20 μm x 20 μm scans were acquired with 512 x 512 pixels. Image analysis was done using L'image software run in IDL to generate ^{16}O, ^{18}O and $^{18}O/^{16}O$ ratio maps and line profiles. MATLAB was used for image segmentation and measurements of the inner oxide layer thickness.

The inward flux of O along the grain boundaries was calculated as described by the previous section using the 2D cross-sectional area of ^{18}O measured at the oxide-metal interface in the ^{18}O isotope maps. Since the grain boundary line length per unit surface area could not be measured during the 2-step isotope experiments, it was instead estimated using the average in-plane grain size measured from the cross-section images.

4.2.4 Additional Characterization

TEM foils and APT specimens were prepared using standard FIB lift-out and thinning procedures on a FEI Helios 650 Nanolab SEM/FIB. Scanning transmission electron microscopy (STEM) imaging and analysis was performed on a JEOL 2100F analytical electron microscope equipped with an EDAX energy dispersive X-ray spectroscopy (EDS) detector, operated at 200 kV. APT data collection was performed using a Cameca LEAP 5000HR instrument operated in laser pulsing mode with a detection rate of 0.5% and a pulse rate of 125 kHz, with samples cooled to 50K. APT data analysis was done using Cameca IVAS software, version 3.8.2.

4.3 Results

To assess the relative oxidation rates at 1200 °C, we first compared weight gain and thickness measurements. As a rough comparison of oxidation rate, the parabolic oxidation rate constants, k_p, were calculated from the weight gain data in the steady-state regime. The rate constants were found to be 52.8, 21.7, 4.9, and 2.4 $\times 10^{-7}$ $mg^2/mm^4/h$ for the NiAl, NiAlTi, NiAlY, and NiAlTiY alloys respectively, within the normal range of most alumina-forming alloys [8]. Not surprisingly, NiAl had the fastest oxidation rate (**Figure 4.1**). NiAlTi exhibited a slightly reduced oxidation rate, and NiAlY and NiAlTiY had the slowest oxidation rates. After 100 hours, the average alumina thicknesses for each alloy were consistent with the weight gain results. NiAl had the thickest oxide, averaging 6.2 µm, followed by the NiAlTi alloy, averaging 4.3 µm, and NiAlY and NiAlTiY had the thinnest oxides, averaging 2.5 µm.

The surface of oxide scales formed on each alloy after 100 hours had different morphologies (**Figure 4.2**). NiAl and NiAlTi had rougher oxide surfaces (**Figure 4.2a and Figure 4.2b**). Distinct, thicker ridges could be seen in some areas of the oxide surface on the NiAlTi alloy (**Figure 4.2b**). NiAlY and NiAlTiY exhibited a network of thin ridges. NiAlY had some "whisker-like" growth in between ridges in some regions across the sample (**Figure 4.2c**), while the oxide on NiAlTiY had a much smoother surface (**Figure 4.2d**). STEM-EDS (**Figure 4.3 and Figure 4.4**) and/or APT grain boundary excess analysis (**Figure 4.5**) confirmed that both Y and Ti segregated to the grain boundaries within the alumina scale on NiAlTi, NiAlY, and NiAlTiY. Ti was detected only in the outer portion of the scale, as has been reported previously [210, 211].

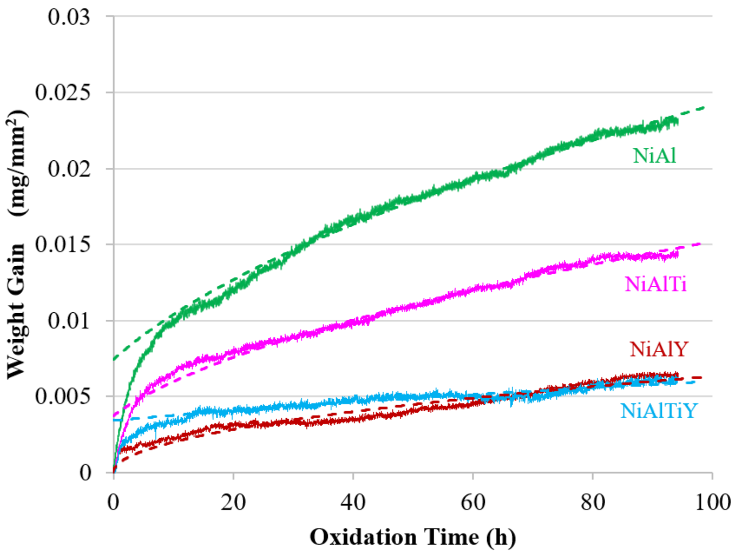

Figure 4.1: Weight gain as a function of oxidation time at 1200 °C. Dotted lines correspond to the parabolic fit for the steady-state regime.

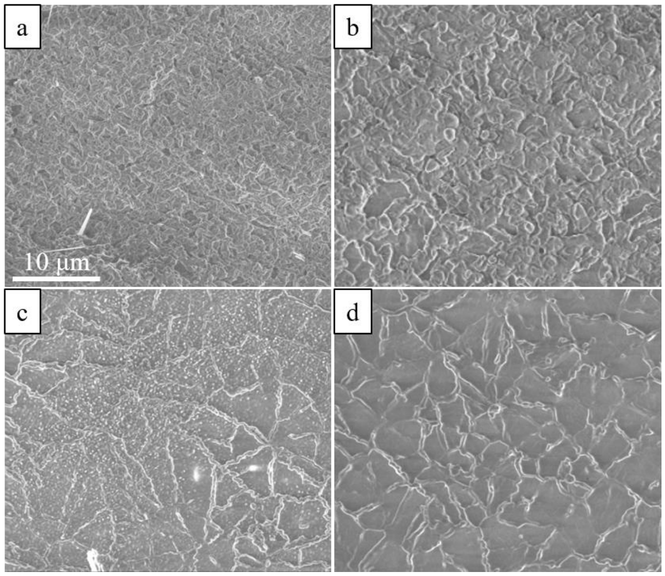

Figure 4.2: SEM images of the surface morphology of the alumina scales on a) NiAl, b) NiAlTi, c) NiAlY, and d) NiAlTiY after 100 hours at 1200 °C.

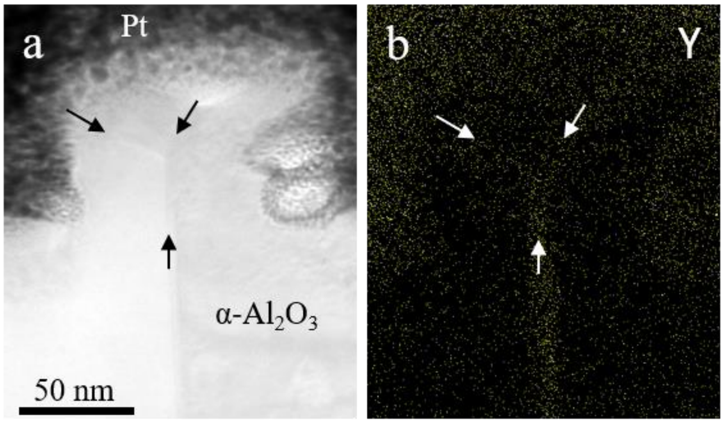

Figure 4.3: STEM-EDS maps of the NiAlY alloy oxidized for 100 hours at 1200 °C prior to polishing the surface and oxidizing for an additional 10 hours. a) Bright-field STEM image of a α-Al_2O_3 ridge with several grain boundaries, with b) a corresponding elemental map showing the distribution of Y.

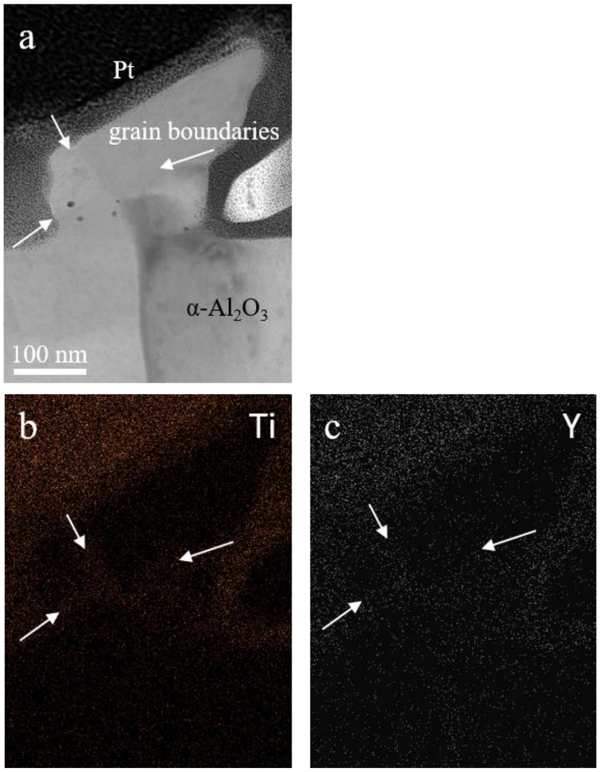

Figure 4.4: STEM-EDS maps of the NiAlTiY alloy oxidized for 100 hours at 1200 °C prior to polishing the surface and oxidizing for an additional 10 hours. a) Bright-field STEM image of a α-Al_2O_3 ridge with several grain boundaries, with corresponding elemental maps showing the distribution of b) Ti, c) Y.

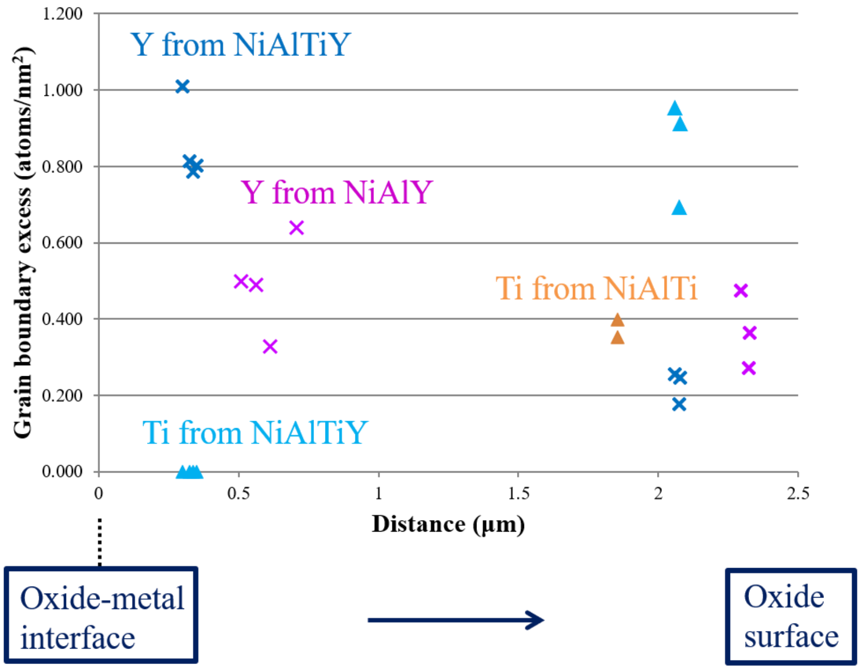

Figure 4.5: APT grain boundary excess of Ti and Y as a function of distance from the alumina-metal interface. Data is from 5 different samples: 2 NiAlTiY (blue), 2 NiAlY (pink), and 1 NiAlTi (orange) each oxidized for 100h at 1200 °C. Note that the alumina scale on each sample had a different thickness.

Differences in outward Al diffusion were assessed through the re-oxidation experiments. A representative cross-section of the polished and re-oxidized scale on the NiAlY alloy is shown in **Figure 4.6**, where small ridges of "new" oxide formed during the re-oxidation step are visible above each grain boundary. Height profile maps of the oxide surface were generated from AFM area scans and correlated with SEM images of ridge networks on the same areas. The upward aluminum grain boundary flux to the surface calculated from the AFM measurement was plotted against the average aluminum oxide thickness measured from SEM/FIB cross-sections in each scan area (**Figure 4.7**). With a thinner scale than the doped alloys, NiAl exhibited a significantly greater flux of Al. For a comparable oxide thickness of 2 μm, the flux of Al is about 30 times greater in NiAlTi than in NiAlY and NiAlTiY. Under the assumptions listed in the experimental section, Al grain boundary diffusivity was comparable in scales on NiAl and NiAlTi, and was about 30-50x greater than for NiAlY and NiAlTiY. Consequently, Ti did not change the Al outward transport kinetics and had little to no effect when co-doped with Y. On the other hand, Y led to a significant reduction in the Al diffusivity.

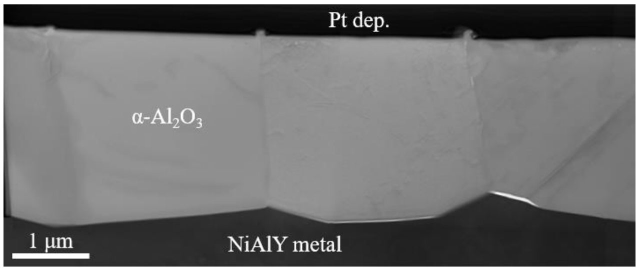

Figure 4.6: Bright field STEM image of a cross-section of the alumina scale on the NiAlY alloy after oxidation for 100h at 1200 °C followed by re-polishing the surface and oxidizing for 10h at 1200 °C. Small ridges of new oxide can be seen above the three vertical grain boundaries.

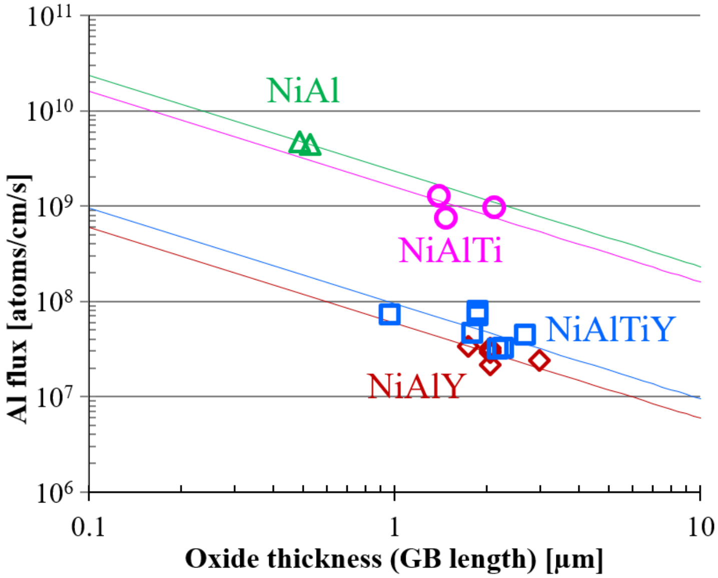

Figure 4.7: Outward Al grain boundary flux versus oxide thickness. Each flux data point was calculated from the new oxide volume measured in the AFM scans of the polished and re-oxidized oxide surfaces. Lines are fit through the data using Eq. (3).

To verify whether Ti affects the inward O transport and to evaluate the effect of co-doping, we used oxygen isotopic tracers in a 2-stage oxidation experiment. A representative set of cross section images is shown in **Figure 4.8** for the NiAl sample oxidized for 15h in $^{16}O_2$ and 20h in $^{18}O_2$. New oxide, identified from the ^{18}O map (**Figure 4.8b**), formed at both the scale surface and the scale-alloy interface. The ^{18}O signal also revealed grain boundaries within the scale, confirming that O transport occurred along these fast diffusion paths. Comparing the ^{18}O maps for each alloy after the same $^{18}O_2$ exposure (**Figure 4.9**), NiAl exhibited smaller, equiaxed grains near the scale surface, and columnar, elongated grains near the scale-NiAl interface. NiAlTi exhibited a dual-layered structure, with smaller equiaxed grains near the scale surface and elongated columnar grains near the scale alloy interface. NiAlY and NiAlTiY had microstructures consisting almost entirely of elongated columnar grains, with few smaller equiaxed grains near the surface of the scale. All alloys exhibited a continuous layer of new oxide at the oxide-scale interface, while the new oxide formed on the scale surface was discontinuous. On NiAl, the new oxide near the top of the scale was thicker in some regions while in some small regions, almost no oxide formed on the surface. In the regions without surface oxide, grain boundaries were spaced further apart. On NiAlTi, regions of new oxide at the scale surface seemed to be smaller than those on the un-doped NiAl, while significant new oxide formed along grain boundaries near the surface of the scale. On NiAlY and NiAlTiY, only small amounts of new oxide could be seen above the scale grain boundaries. Some grain boundaries within the scales had thicker ^{18}O signal than others, especially near the surface of the scale on NiAl and NiAlTi and near grain boundary junctions.

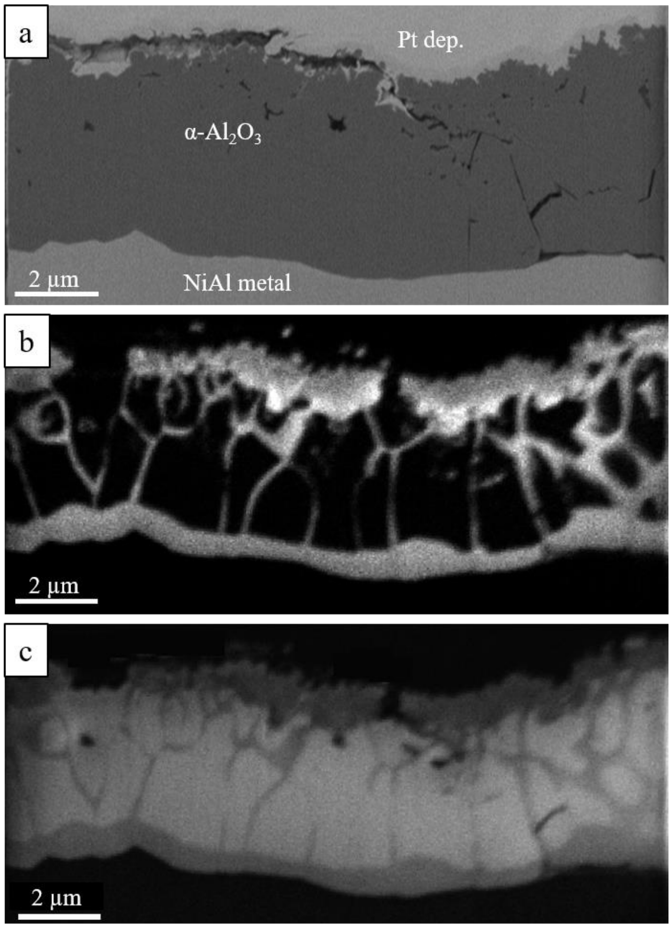

Figure 4.8: a) SEM image, b)^{18}O and c)^{16}O SIMS maps of a cross-section of the alumina scale grown on NiAl oxidized for 15h in $^{16}O_2$ and 20h in $^{18}O_2$. Cracks visible in (a) are from FIB lift-out preparation.

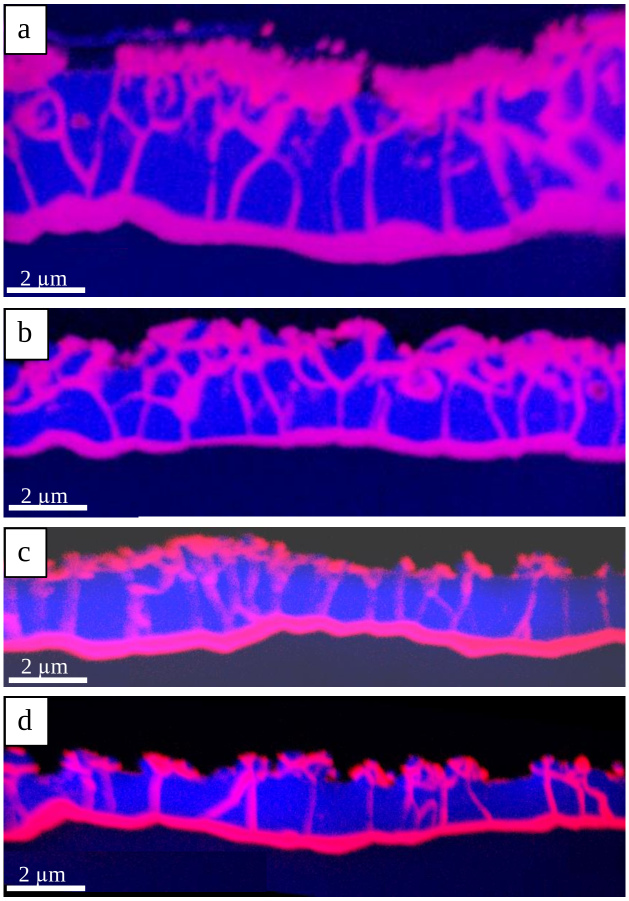

Figure 4.9: Overlaid SIMS maps of the alumina scales on a) NiAl, b) NiAlTi, c) NiAlY, and d) NiAlTiY after pre-oxidation in $^{16}O_2$ and 20h in $^{18}O_2$. ^{18}O in red and ^{16}O in blue.

To quantitatively compare the inward oxygen transport through the scale on each alloy, we measured the area of the continuous layer of ^{18}O-rich oxide at the scale-alloy interface, assuming it to be "new" oxide formed during the oxidation step in $^{18}O_2$. The inward oxygen flux to the oxide-metal interface was calculated as described in the "Experimental Details" section. The average oxygen flux for each alloy was then plotted against the average oxide thickness (**Figure 4.10**). The intercept was smaller for all of the doped alloys. The values for the Ti- and Y- doped alloys were similar, while that of the Ti+Y-doped alloy was slightly lower, suggesting a beneficial impact of co-doping.

The relative inward/outward growth of the alumina scales was estimated by measuring the thicknesses of the equiaxed and columnar layers (**Figure 4.11**) in the ^{18}O maps**.** NiAlY and NiAlYTi had significantly thinner equiaxed layers than NiAl and NiAlTi. The three doped alloys had slightly thinner columnar layers than that of NiAl. The ratios of equiaxed to columnar layer thickness were 0.80, 0.93, 0.31, and 0.37 for the alumina scales on NiAl, NiAlTi, NiAlY, and NiAlTiY respectively.

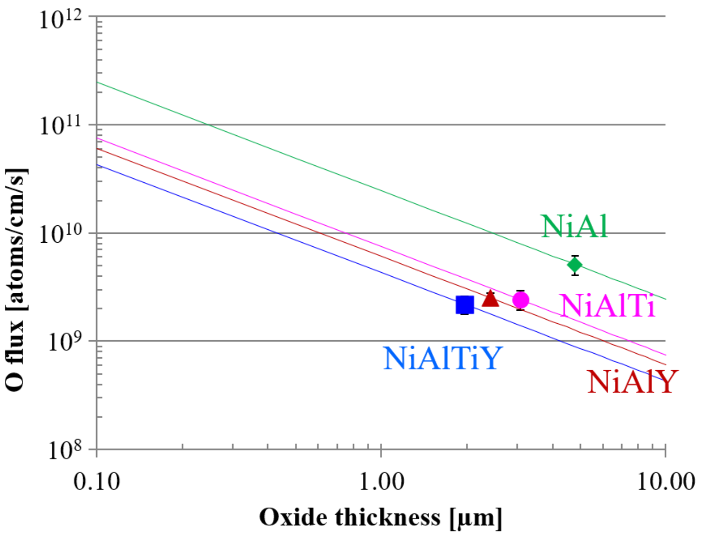

Figure 4.10: Inward O grain boundary flux versus oxide thickness for each alloy. Each flux data point was calculated from the average thickness of the inner ^{18}O-rich layer measured in the ^{18}O SIMS maps. Lines are fit using Eq. (3).

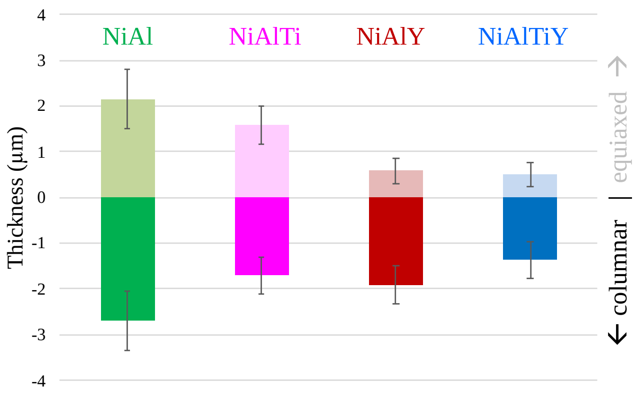

Figure 4.11: Thickness of the equiaxed (light) and columnar (dark) layers on alumina scales on each alloy after pre-oxidation and subsequent 20h of oxidation in $^{18}O_2$.

To clarify whether the apparent grain boundary thickness in the ^{18}O SIMS maps was an artefact of the foil thickness or reflective of new oxide, we performed APT analyses. Several tips were prepared along grain boundaries within the middle of the alumina scales on NiAl and NiAlTiY, avoiding the new oxide regions formed at the top surface and scale-metal interface. A representative APT reconstruction obtained from NiAlTiY is shown in **Figure 4.12** where Y atoms acted as markers for the alumina grain boundaries. The ^{18}O atoms are present only on one side of the grain boundaries, extending about 10-15 nm, as confirmed by the concentration profile (**Figure 4.12c**) taken perpendicular to one of the grain boundaries. The measured ratio of $^{18}O/^{16}O$ was about 0.5 and increased slightly away from the Y segregation. In the un-doped NiAl sample, the location of the grain boundary could not be determined since no dopants were present to act as a marker (**Figure 4.13**). However, the ^{18}O-enriched region was found to be about 15-20 nm thick, exhibited a similar $^{18}O/^{16}O$ ratio (~0.6), and a slightly increasing ^{18}O concentration across the new oxide region.

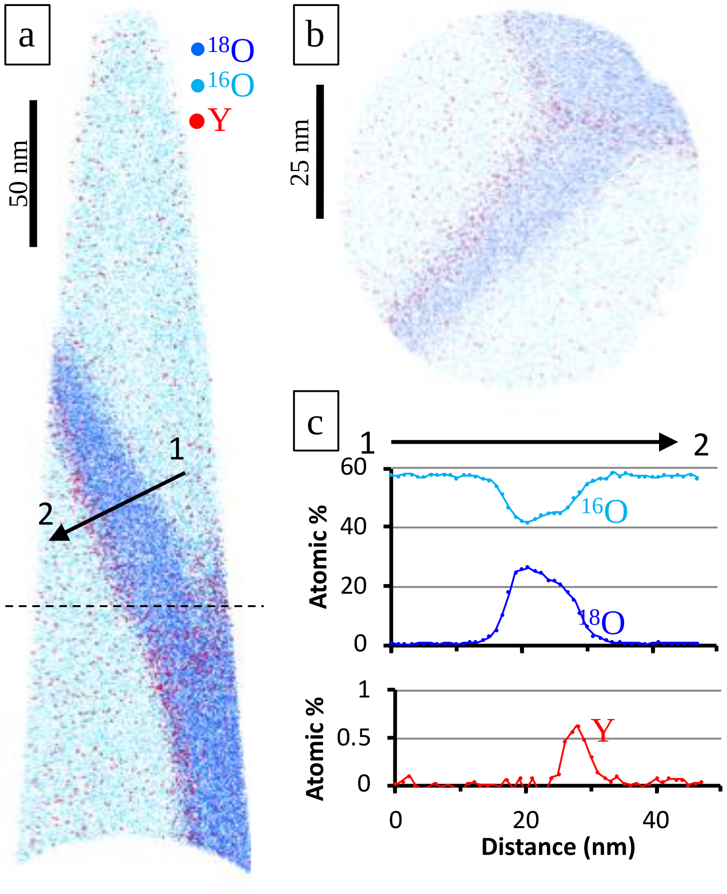

Figure 4.12: APT reconstruction of a volume prepared from within the alumina scale on the NiAlTiY alloy after 26h in $^{16}O_2$ and 20h in $^{18}O_2$. a) A 20nm thick vertical slice and b) a 10nm thick horizontal slice of the reconstruction with ^{18}O ions shown in dark blue, ^{16}O ions in light blue, and Y ions in red. Al ions are not shown for clarity. c) Composition profile across grain boundary shown by the line marked 1-2 in (a).

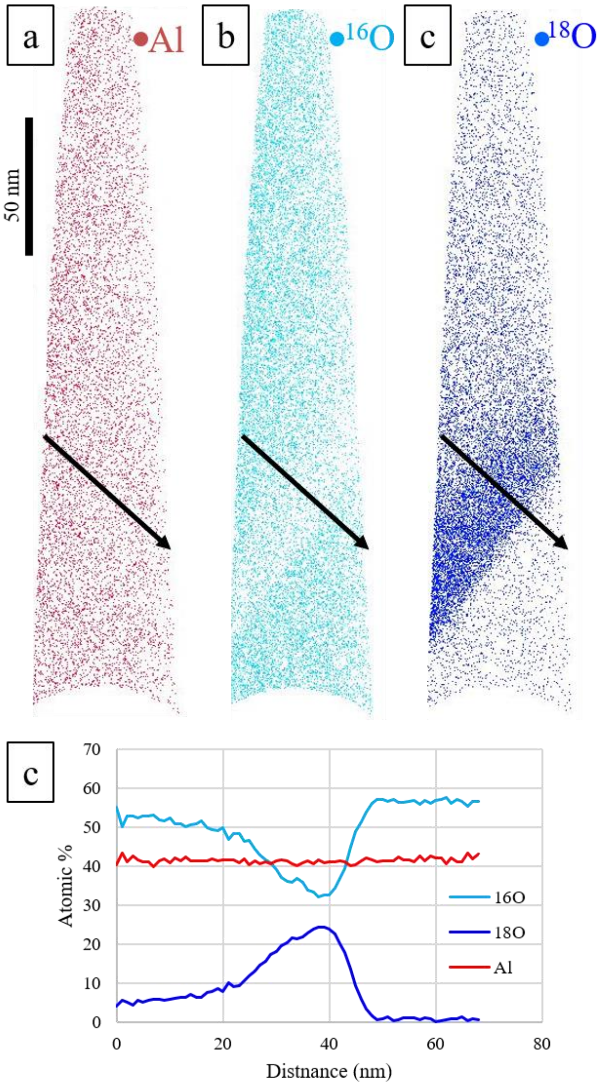

Figure 4.13: APT reconstruction of a volume prepared from within the alumina scale on the NiAl alloy after 15h in $^{16}O_2$ and 20h in $^{18}O_2$. A 5nm thick slice shows a) Al ions shown in red, b) ^{16}O ions in light blue, and c) ^{18}O ions in dark blue. c) A composition profile across the grain boundary, shown by the line marked in (a),(b), and (c).

The $^{18}O/^{16}O$ ratios were not constant throughout the ^{18}O-enriched regions in the cross-sections analyzed by NanoSIMS. In the ^{18}O-rich oxide at the scale surface, $^{18}O/^{16}O$ ratios ranged from ~0.7-2, while in the bottom ^{18}O-rich layer, the $^{18}O/^{16}O$ ratios ranged from ~0.3-0.6, suggesting that some isotope exchange took place as ^{18}O diffused from the gas to the alloy interface. At the oxide surface, ^{18}O reacts with Al that has diffused up from the alloy. Thus, the

^{18}O/^{16}O ratio should reflect the ^{18}O/^{16}O ratio of the gas used in the 2nd stage exposure. The ^{18}O-enriched gas used was thought to be at least 97% ^{18}O, much higher than the concentration detected in the top ^{18}O-rich oxide (~40-70% ^{18}O). To resolve this inconsistency, an additional experiment was undertaken.

An NiAl sample previously oxidized for 15 hours in $^{16}O_2$ and 5 hours in $^{18}O_2$ was oxidized for an additional 5 hours in air (**Figure 4.14**). A new layer of nearly pure ^{16}O oxide (^{18}O/^{16}O ratio of ~0), reflecting the gas composition, appeared at the surface above an ^{18}O-rich layer (**Figure 4.14b**). The ^{18}O-rich layer just below the new surface oxide that was formed during the $^{18}O_2$ exposure had an unchanged ^{18}O/^{16}O ratio of ~0.7 (**Figure 4.14c**). Since oxidation in air (~ pure $^{16}O_2$) led to an oxide with nearly no ^{18}O, we conclude that the ^{18}O-enriched gas used in the tracer experiments likely had a lower concentration of ^{18}O than expected. At the scale-gas interface, the new oxide layer formed during air exposure exhibited a slight enrichment with ^{18}O. A line profile through the bottom layer revealed that the ^{18}O/^{16}O ratio in the top part of the layer was ~0.4, while closer to the alloy the ratio was ~0.1 (**Figure 4.14d**). For comparison, a line profile through the bottom ^{18}O-rich layer on NiAl without the additional 5 hour air exposure shows a ^{18}O/^{16}O ratio of ~0.3 with a steep drop off to 0. This suggests that the portion of the ^{18}O-rich layer near the alloy with ^{18}O/^{16}O ~0.1 was a result of new oxide growth during the additional air exposure. This new layer was slightly enriched in ^{18}O due to isotope exchange as the ^{16}O atoms diffused along the scale-gas interface of the previous ^{18}O-rich layer. Some of the thicker ^{18}O regions on the grain boundaries also appeared to have a region of lower ^{18}O/^{16}O on one side (see white arrow in **Figure 4.14b**), suggesting that similar isotope exchange took place as ^{16}O diffused downward along the grain boundaries.

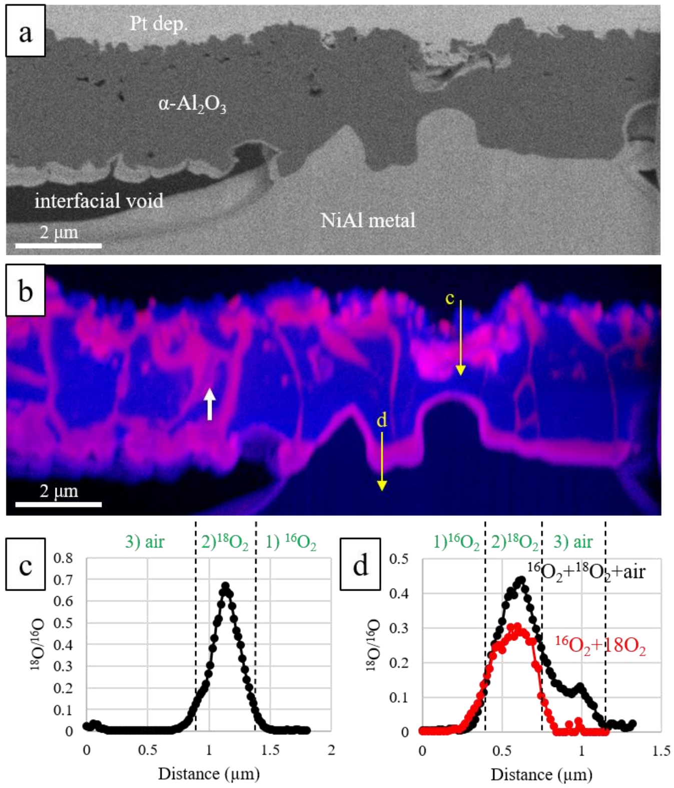

Figure 4.14: a) SEM image of a cross-section of an alumina scale grown on NiAl after 15h in $^{16}O_2$, 5h in $^{18}O_2$, and 5h in air. b) Overlaid ^{18}O (red) and ^{16}O (blue) SIMS maps of the same area. c) A profile of the $^{18}O/^{16}O$ ratio through the top portion of the scale and d) through the region near the scale-alloy interface (locations shown in (b)), along with the profile from a similar region in the scale on NiAl oxidized for 15h in $^{16}O_2$ and 5h in $^{18}O_2$ shown in red. Above the plots in (c) and (d), regions are labeled with the oxidation step during which they formed.

4.4 Discussion

Though the benefits of reactive dopant additions on oxidation behavior are widely known, the question of why different dopant elements produce different effects on oxidation rate remains elusive. High temperature oxidation involves multiple oxide phases, evolving microstructures, transport processes, and stress development, all of which can be affected by dopant additions. This study tested one aspect, specifically that different dopant elements, Y and Ti, elicit varied effects on aluminum and oxygen transport through the alumina scale, yielding differences in oxidation rate.

Doping with Y was the most effective in reducing oxidation rate, and reduced both Al and O transport through the scale. The alloys doped with yttrium (NiAlY and NiAlTiY) exhibited a significantly lower Al grain boundary flux compared to un-doped NiAl. As a result, the Y-containing alloys had a significantly smaller equiaxed to columnar thickness ratio compared to the un-doped alloy, and exhibited thin surface ridges compared to thicker overgrown ridges on the surface of the un-doped alloy. These results are consistent with reports that Y additions reduces outward alumina scale growth and Al and O transport [98, 99, 118, 120]. In particular, Nychka *et al*. [99] found that commercial FeCrAl-based alloys containing Y had lower Al flux through alumina compared to Y-free alloys. Y additions also reduced oxygen grain boundary diffusion in bulk α-Al_2O_3 [130, 131, 212]. In contrast, a recent study of Y-doped bulk polycrystalline α-Al_2O_3 using a ^{26}Al isotope tracer found that Y addition did not affect Al grain boundary diffusion [141]. However, it is yet to be determined if transport in bulk α-Al_2O_3 is comparable to transport through α-Al_2O_3 scales [108].

Ti additions were slightly less effective than Y, but still reduced the oxidation rate in comparison to the un-doped alloy. This moderate oxidation rate was consistent with changes in Al/O transport. Ti reduced inward O grain boundary flux relative to the un-doped NiAl alloy, but had no significant effect on Al flux. The surface morphology of the Ti-doped alloy had thick overgrown ridges like the un-doped alloy, consistent with no change in the outward Al flux. The Ti-doped alloy had a slightly larger equiaxed to columnar ratio and a thinner columnar layer compared to the un-doped NiAl, consistent with reduced inward O flux. In bulk polycrystalline α-Al_2O_3, additions of Ti were also found to reduce oxygen grain boundary diffusion [213].

Co-doping with Ti+Y slowed the oxidation rate only slightly further than doping only with Y. This reduction in oxidation rate is consistent with the slight reduction in inward O flux compared to the single-doped Y sample. This is also reflected in the measurement of the equiaxed and columnar thickness layers, where NiAlTiY exhibited a thinner columnar layer than NiAlY. Previous studies also found that co-doping with multiple elements can have a synergistic effect on oxidation behavior [9, 104, 129], and that the combination of Ti+Y in particular may reduce the oxidation rate of alumina-forming alloys [152, 206]. It was proposed that co-doping reduced the formation of internal RE-rich oxides in and below the scale [129, 206], which can promote fast diffusion and initiate spalling [214]. Alternatively, others suggested co-doped elements form ionic clusters on alumina grain boundaries that suppress diffusion [104, 153]. In the current study, no internal Y- or Ti-rich oxides were formed within the scales on the single-doped alloys, perhaps explaining why only a slight change in oxidation rate was observed with NiAlTiY in comparison to NiAlY. Y and Ti co-segregated along the alumina grain boundaries, possibly leading to additional reductions in O transport.

Though it remains difficult to determine the mechanism for dopant effects on grain boundary transport, many explanations have been proposed in the context of thermally grown scales. The relatively larger size of the Y^{3+} ion compared to Al^{3+} was suggested to effectively "block" Al diffusion along the grain boundaries [97, 99, 131, 215]. Others proposed that defect chemistry may play a role, and aliovalent dopants may change the defect concentration at the grain boundaries due to charge compensation [211]. Alternatively, isovalent dopants such as Y^{3+} may sit in cation sites at the grain boundary that otherwise may be occupied by aliovalent impurities, such as Ca^{2+} or Si^{4+}, that could alter Al vacancy concentration and increase Al diffusivity in the un-doped sample [131]. The electronic nature of the scale may also play a role. Dopant elements have been proposed to modify Al_2O_3 donor and acceptor states, altering the availability of electronic defects needed for the creation of Al/O vacancies [146]. Others have suggested the dopant metal-oxide bonding strength may influence the diffusion of O along the grain boundaries [137]. Further studies are needed to determine the dominant diffusing species along grain boundaries in Al_2O_3 during oxidation, and to conclusively explain the mechanisms of dopant effects on grain boundary transport.

In addition to comparison of outward and inward transport, ^{18}O maps of the scale cross-sections revealed the dynamic nature of the scale microstructure. Thick ^{18}O layers, sharply defined by ^{18}O concentrations, were present along the grain boundaries of the scales. The measured thicknesses of these ^{18}O-rich regions, ~10-30 nm, is significantly larger than one would expect if ^{18}O was simply segregated along the grain boundary. If ^{18}O atoms initially along the grain boundaries diffused into existing grains, then a smoothly decreasing concentration of ^{18}O atoms would be expected on both sides of the grain boundaries marked with Y. Instead, the steep concentration gradients and their location on one side of the grain boundaries suggests that the alumina grain boundaries are migrating during oxidation. A few previous studies have likewise observed ^{18}O on what looked to be grain boundaries in the scale [122, 123, 125], but did not discuss its origin.

Grain boundary migration during oxidation could be the result of several parallel processes. New oxide may form along the grain boundaries due to the simultaneous counter-diffusion of Al and O. Rather than forming new grains, the growth of new oxide may favor one pre-existing grain over another to minimize strain energy. The formation of oxide at the grain boundaries causes a lateral expansion, and is thought to generate compressive stress build-up in growing alumina scales [156-159]. The thicknesses of new oxide formed at the boundaries are consistent with oxide growth strains estimated in previous literature [61, 157, 158]. While growth strain varies with scale thickness and oxidation temperature [157], for a 2 µm scale at

1200 °C (similar conditions to the current study), the growth strain was estimated to be 0.5%. Assuming a simplified model of oxide microstructure with vertical grain boundaries, the expected growth strain in the scale due to new oxide formation and lateral expansion can be estimated according to:

$$\varepsilon_G = \frac{\Delta L}{L} = \frac{\Delta x}{D}$$

where ε_G is the growth strain associated with new oxide formation at the grain boundaries, Δx is the lateral thickness of new oxide, and D is the lateral oxide grain size [157]. If the ^{18}O regions on the grain boundaries observed in the current work are indeed a result of new oxide formation, then Δx = 10-12 nm for the NiAlTiY alloy, and the average lateral grain size, D = 1.2 μm, resulting in a growth strain, ε_G~0.5-0.8% in agreement with Tolpygo *et al.* [157].

The variation in the thickness of new oxide among individual grain boundaries can be explained by the variation of transport along individual grain boundaries, as demonstrated for oxygen diffusion [133-135]. The scales on NiAl and NiAlTi showed a larger flux of upward Al and more extensive ^{18}O along the grain boundaries near the top portion of the scale among the equiaxed grains, suggesting that increased grain boundary flux may also increase the formation of new oxide within the scale.

Other diffusional processes such as grain coarsening and creep could drive grain boundary migration. Grain coarsening occurs in bulk alumina ceramics at high temperature [110-112, 216]. However, the current literature is not clear on whether significant alumina grain coarsening occurs during oxidation, and limited data can be found for grain size measurements of Al_2O_3 scales [100, 108, 113]. In the present study, the average lateral grain size of each alloy oxidized for shorter times was similar to that of the same alloys oxidized for longer times, however the measurements were not sensitive enough to capture a change smaller than 100 nm.

In bulk ceramics, alumina coarsening studies are typically conducted at temperatures above 1400 °C, significantly higher than relevant temperatures for thermal oxidation, (~800-1200 °C). Grain growth can be described by:

$$d^n = d_o^n + Kt$$

where d is the average grain size, d_o is the initial grain size, t is the time at temperature, n is the grain growth exponent, and K is the temperature-dependent grain growth constant. For bulk polycrystalline alumina at temperatures between 1700-1850 °C, $n \sim 3$ and $K \sim 9 \times 10^{-19}$ m^3/s [110, 216]. Extrapolating K to 1200 °C and using an estimated 1.2 µm for the initial scale grain size, 20 hours of additional oxidation would result in a grain size of roughly 86 µm, far larger than typical grain sizes observed in Al_2O_3 scales. Thus, it seems grain growth relationships found for bulk alumina at temperatures above 1700 °C do not hold for thermally grown alumina scales at 1200 °C.

For thermally grown alumina on a NiCoCrAl(Y) alloy oxidized at 1100 °C, Choquet *et al*. [113] estimated $n \sim 10\text{-}14$ and $K \sim 4.5 \times 10^{-4}$ $\mu m^3/h$. Using these values to estimate grain growth at 1200 °C from a starting grain size of 1.2 µm, after 20 hours the average grain size is estimated to be 1.8 µm. This value is closer to typical scale grain sizes, but still is far larger than the 10-30 nm grain boundary migration observed in the current study. Thus, we conclude that for the alloys studied here, grain growth in the Al_2O_3 scale appears to be minimal during oxidation. In this case, the segregation of Y and/or Ti to the grain boundaries may inhibit thermal grain growth. Finally, a creep-mediated mechanism is also possible since creep of alumina is known to occur during high temperature oxidation [61, 157, 217].

Understanding how different dopants affect Al and O transport through alumina scales is a critical step for developing predictive models of oxidation rate and component lifetime, taking into account microstructures, transport, growth rates, and stress development and relaxation. Quantifying the mechanisms is also essential to inform the design of highly oxidation-resistant alloys. This work focused on steady state oxidation rates and Al and O grain boundary transport. However, dopants can also affect other aspects of high temperature oxidation, such as transient oxidation, a topic currently under investigation.

4.5 Conclusions

Outward alumina and inward oxygen flux through alumina scales grown on NiAl alloys doped with Ti, Y, and Ti+Y were assessed and discussed in the context of the oxidation rate of each alloy. Our results suggest that different dopant elements elicit varied effects on Al and O transport, contributing to differences in oxidation rate. The following conclusions were reached:

- Ti slightly reduces the oxidation rate, while Y and Ti+Y significantly reduce the oxidation rate when alloyed with NiAl, evidenced by weight gain measurements over time and oxide thickness.
- Ti does not significantly affect upward Al transport, but reduces inward oxygen transport along grain boundaries.
- Y decreases both upward Al transport and inward O transport along alumina grain boundaries.
- Co-doping with Ti+Y reduces both oxidation rate and inward oxygen transport slightly more compared to doping only with Y.
- ^{18}O was detected along grain boundaries within the scale as a result of grain boundary migration during oxidation.

These results add to our understanding of the effects of different elements on both Al and O transport during high temperature oxidation and can be used for the development of more accurate models of oxidation rate and targeted alloy design. In addition, effects on concurrent Al and O fluxes are shown to impact the evolution of scale microstructure, which have implications for stress development and the protective scale lifetime.

CHAPTER 5:

The Effect of Ti on the Early Stages of Oxidation of an Alumina-Forming NiCrAl Alloy[1]

5.1 Introduction

Alloys are often designed to form multi-layered oxide scales to protect against oxidation and corrosion upon exposure to a range of temperatures and environments. In the case of ternary Ni-Cr-Al alloys, the steady-state morphology and composition of oxide scales formed strongly depend on alloy chemistry. This correlation has been experimentally determined and mapped onto a Ni-Cr-Al ternary phase diagram [3]. For example, a continuous Al_2O_3 scale requires a minimum alloy Al concentration and Cr alloying decreases this critical Al content. However, while the oxidation behavior of binary or ternary Ni-Cr-Al alloys is relatively well understood [18], the situation is quickly complicated by the addition of alloying elements. Commercial superalloys have on the order of ten or more components, and each may affect the formation and growth of oxide scales. Moreover, small amounts of dopant elements can have a significant effect on the oxidation kinetics and mechanical properties of a protective scale [9].

The contribution of alloying elements to the oxidation behavior may take several different forms. The “reactive” elements such as Y, Hf, Zr, and Ce, were found to segregate to Al_2O_3 grain boundaries and reduce significant upward cation transport [8, 9]. Other elements,

---

[1] The content of this chapter has been adapted from the following publication:
Barth, T. L. and Marquis, E. A., *The Effect of Ti on the Early Stages of Oxidation of an Alumina-Forming NiCrAl Alloy*. Oxidation of Metals, 2019. **92**:13-26.

such as Ti in chromia, may affect bulk diffusion through the oxide scale by changing defect concentrations [218]. The so-called “third element effect” that describes the effect of Cr on Al_2O_3 formation has been linked to a change in the activity of oxidizing elements in the alloy leading to a reduction in the critical concentration required to create a continuous oxide scale [219].

Titanium is often present as a minor alloying element in Ni-base superalloys to stabilize the γ’ strengthening phase [220], but its effect on the oxidation response is unclear. In the case of chromia-forming alloys, faster growth kinetics were observed for chromia on a Ti-containing alloy than chromia on an un-doped alloy [221]. It was suggested that Ti acts by increasing the chromium vacancy concentration in chromia [222, 223]. The effect of titanium doping on aluminum oxide scales is less clear. On NiAl alloys that form exclusive, continuous alumina scales, titanium additions slightly reduced the alumina growth rate [97][10] and suppressed the surface ridge structure typical of NiAl oxidation [71]. However, Ti additions to γ-Ni alloys slightly increased the alumina oxidation rate while having no significant effect on other alloy compositions, suggesting that the effect of Ti-doping may be dependent on the matrix composition as well as level of Ti addition [203]. In alloys containing reactive elements such as yttrium, there seems to be some synergistic effect between the different alloying elements. In NiCrAlY alloys, titanium additions reduced the long-term oxidation rate by changing the alumina morphology and promoting a uniform and continuous scale rather than internal alumina oxidation [152]. In FeCrAlY alloys, Ti+Y co-doping led to a slight decrease in oxidation rate as compared to the solely Y-doped alloy [206]. The microstructures of the Y-doped and Y+Ti doped alloys were similar, but in the Ti-doped scale, no Y-rich oxide precipitates were observed, while yttrium oxides were found in the scale grown on the Ti-free alloy, implying that titanium might affect the distribution of yttrium throughout the oxide scale. Additionally, Ti was found to segregate to grain boundaries in alumina scales, with more Ti present at the top of the scale than at the scale-alloy interface, suggesting that Ti diffuses upward through the scale along the interfaces [195], similar to the “reactive element” type effect. However, from the current literature, it is still unclear how Ti alone affects the kinetics and early development of protective oxide scales.

The variety of alloy compositions used in prior studies has limited our understanding of the exact role of Ti on the oxidation of alumina-forming Ni alloys. Therefore, the goal of this study is to isolate the effect of titanium on the oxidation behavior of a model Ni-Cr-Al alloy by performing detailed microstructural characterization of the oxide scales as they develop at short oxidation times.

5.2 Experimental Procedure

Four alloys were considered in this study. Alloy 1 was Ti-free and selected so that the γ-Ni phase was the only stable phase at the oxidation temperature of 1000 °C (**Figure 5.1**) while forming a continuous Al_2O_3 scale (region III) [3]. Two Ti-containing alloys (Alloy 2 and 3) with the same Cr and Al concentrations (26 and 10 at.% respectively) as the reference Alloy 1 were also used. Alloy 2 contained 0.6 at.% Ti and Alloy 3 1.7 at.% Ti. Alloys 1, 2, and 3 were cast using a Bridgeman furnace, solution treated at 1200 °C for 100 h, and air-cooled. All nominal compositions are listed in **Table 5-1**.

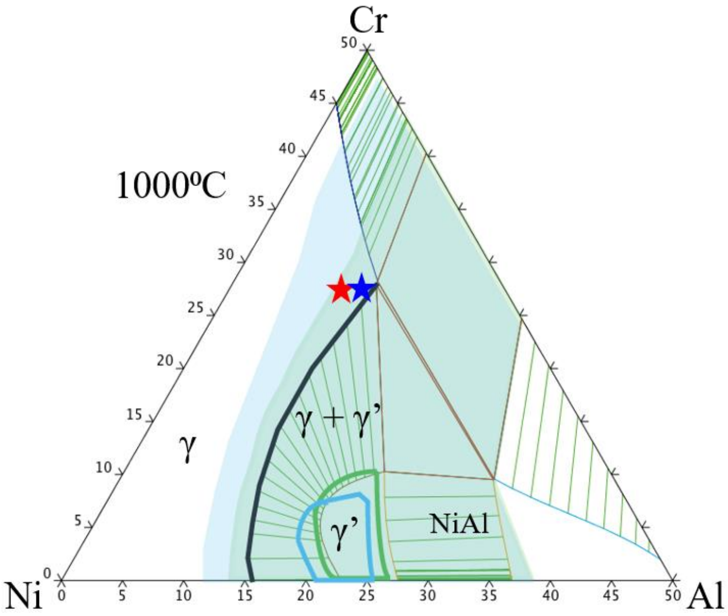

Figure 5.1: Ni-Cr-Al phase diagram (at.%) at 1000 ºC calculated in ThermoCalc using the TCNI8 superalloys database, v8.1. The red star shows the location of Alloy 1 (Ni-26Cr-10Al), and the blue star shows Alloy 4 (Ni-26Cr-12Al). The green and blue highlighted areas and lines represent the calculated γ + γ' phase fields for the +0.6Ti (Alloy 2) and +1.7Ti (Alloy 3) respectively.

Table 5-1: Nominal alloy compositions in at.%.

ID	Ni	Cr	Al	Ti
Alloy 1	bal.	26	10	0
Alloy 2	bal.	26	10	0.6
Alloy 3	bal.	26	10	1.7

Prior to oxidation, the alloy surfaces were ground using 320, 600, and 1200 grit SiC paper to ensure a flat and uniform surface, and then polished using 6, 3, and 1 μm diamond slurries. For the isothermal oxidation experiments, samples were placed in an alumina boat inside a quartz tube. Samples were first heated to 1000 ºC in pure Ar gas. Once at temperature, O_2 gas was introduced and samples were oxidized in a 20% O_2-Ar atmosphere for set times ranging from 5 minutes to 32 hours.

Oxide scale surfaces and cross-sections were characterized using a FEI Helios 650 NanoLab scanning electron microscope (SEM) and focused ion beam (FIB) and FEI Nova 200

Nanolab SEM/FIB. Wavelength dispersive spectroscopy (WDS) was performed using a Cameca SX100 Electron Probe Microanalyzer using Cr, Al, Ti, and NiAl metal reference samples. Electron-transparent cross-section lamellae were prepared using a standard FIB lift-out and thinning technique. Electron microscopy imaging, electron diffraction, and energy-dispersive spectroscopy (EDS) was performed on a JEOL 2010F Analytical Electron Microscope with 200 kV accelerating voltage, equipped with an EDAX Sapphire Si-Li X-ray detector and EDAX Genesis software. Atom probe tomography (APT) needle-shaped specimens were prepared using standard FIB lift-out and milling procedures. APT analysis was carried out on a Cameca LEAP 4000X HR Atom Probe instrument operated in laser mode with a laser energy of 50 pJ, detection rate of 0.005 atoms/pulse, and a pulse rate of 200 kHz, with samples cooled to 50 K. APT data reconstruction and analysis were done with Cameca IVAS software version 3.6.12.

5.3 Results

The as-received alloys were polycrystalline with grain sizes around 100-200 μm for Alloys 1-3. In the Ti-containing alloys, a γ+ γ' microstructure was observed, with an average γ' particle radius of 45.7 nm for the Alloy 2, and 65.2 nm for the Alloy 3 (**Figure 5.2a**). Considering the size of the γ' particles, and the calculated γ' solvus temperature of 1012 ^{o}C and 1080 ^{o}C in the low-Ti and high-Ti alloy, respectively, it is likely that γ' formed upon cooling after the solution treatment at 1200 ^{o}C. These γ' precipitates were observed below a depletion zone under the oxide scale, and coarsened slowly as oxidation progressed, but are not thought to significantly affect oxidation behavior. Additionally, large, faceted TiN particles could be seen in both Ti-containing alloys prior to oxidation (**Figure 5.2b)**.

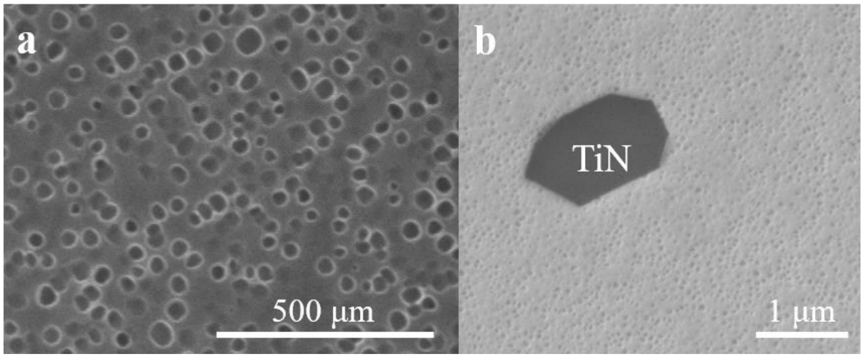

Figure 5.2: SEM images from the as-received Ni-26Cr-10Al-0.6Ti alloy: a) γ+γ' and b) TiN particle. Images were taken using a through lens detector (TLD) in secondary electron (SE) mode, with a 2 kV accelerating voltage.

The oxidation of Alloy 1 (Ni-26Cr-10Al) revealed oxide thicknesses and morphologies varying significantly across the surface of the alloy, and correlating with an inhomogeneous Al distribution throughout the alloy, despite solution treatment. As illustrated in **Figure 5.3** in the low-Al regions, with Al concentrations as low as ~ 6.7 at.% Al, long, discontinuous alumina fingers and an overall thicker oxide scale formed after oxidation for 32 hours at 1000 °C. Alternatively, a compact, continuous alumina layer and overall thinner oxide scale formed in the high-Al regions, containing 9.5 at.% Al on average. Comparatively, no Al concentration inhomogeneity was observed in the Ti-containing alloys that exhibited uniform Al distribution with concentrations comparable to those in the high-Al regions of the un-doped alloy. According to early work on the oxidation of the Ni-Cr-Al system [3, 14], the critical Al content at which the oxide scale transitions from discontinuous internal alumina precipitates to a continuous Al_2O_3 scale occurs around 10 at.% Al for alloys containing 26 at.% Cr, and small changes in Al concentration near this critical value may have a significant effect on oxidation behavior. For the remainder of this study, we focus exclusively on regions of high Al content in Alloy 1 when comparing to the Ti-containing Alloys 2 and 3, to distinguish the effect of Ti doping from effects of Al concentration.

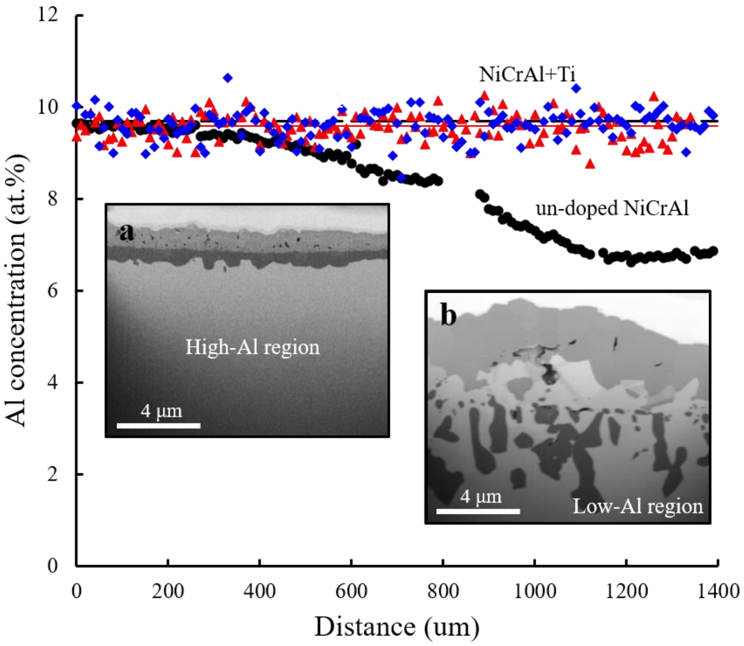

Figure 5.3: WDS composition profiles parallel to the alloy surface, measured approximately 400 µm below the scale, showing the aluminum content across the matrix region in Alloys 1, 2, and 3, after oxidation at 1000 ºC for 32 h. The right side of the line scan shows a region of low Al content typical in the as-received un-doped NiCrAl alloys, while no such regions were observed in the Ti-containing alloys. SEM images, taken using a TLD detector in backscatter-electron mode with 2 kV accelerating voltage, of the oxide scale observed on Alloy 1 in both the high (a) and low-Al (b) regions are presented for comparison.

Starting with Alloy 1 after 5 minutes of oxidation at 1000 °C, a continuous Cr_2O_3 layer was observed in cross-section (**Figure 5.4a**), below which discontinuous Al_2O_3 “fingers” formed deeper into the alloy. After 30 minutes of oxidation, the oxide scale revealed two different regions distinguished by their surface imaging contrast (bright and dark). These regions did not correlate with the Al compositional fluctuations and were present in both the low and high Al portions of the alloy (**Figure 5.5a**). In the “bright” scale regions, a multi-layered scale formed, consisting of (from top to bottom) discontinuous islands of NiO on the surface, a continuous layer of Cr_2O_3, Ni-rich metal grains, and an Al_2O_3 layer with fingers extending into the alloy (**Figure 5.5c**). In the “dark” scale regions (**Figure 5.5b)**, the same phases and morphology were present with the exception of the NiO islands. Oxide phases were identified by EDS analyses and in the case of the Cr_2O_3 and Al_2O_3 phases, by additional selected area electron diffraction. Large pores were also visible between the Cr_2O_3 and Al_2O_3 layers among the Ni metal grains that contained ~5 at.% Cr and <1 at.% Al, as estimated by EDS. After 2 hours of oxidation, two regions were still visible on the surface, with the "dark" regions still lacking NiO on the surface. The Al_2O_3 transitioned to a more continuous layer. Discontinuous Cr_2O_3 grains, rather than a continuous Cr_2O_3 layer, were observed within a Ni and Cr-rich oxide layer (**Figure 5.6b**) that had a composition consistent with that of the $NiCr_2O_4$ phase. A representative EDS mapping analysis used to distinguish the oxide phases within the scale is shown in **Figure 5.7**, along with a concentration profile across the scale. Finally, we also note that the Ni-rich metal grains observed after 30 minutes were replaced by large voids and grains of $NiCr_2O_4$. After 8 hours of oxidation, the same phases (NiO, $NiCr_2O_4$, Cr_2O_3, and Al_2O_3) were present, with few isolated grains of NiO on the surface. The distinct contrast regions were no longer observed. The alumina layer thickened slightly to become more uniform. A continuous Cr_2O_3 layer was identified directly above the Al_2O_3 layer. A $NiCr_2O_4$ layer was still present above the Cr_2O_3 layer. After 32 hours of oxidation (**Figure 5.6c**), the Al_2O_3 layer had thickened, while the combined thickness of the $NiCr_2O_4$ and Cr_2O_3 layers did not appear to grow, and only occasional NiO grains on the top surface of the scale remained.

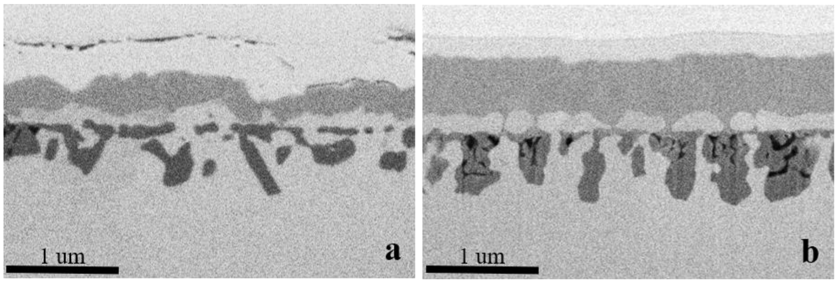

Figure 5.4: SEM images of FIB cross-sections of a) Alloy 1 and b) Alloy 3, oxidized at 1000 ºC for 5 minutes. Images were taken using a TLD detector in BSE mode, with an accelerating voltage of 2 kV.

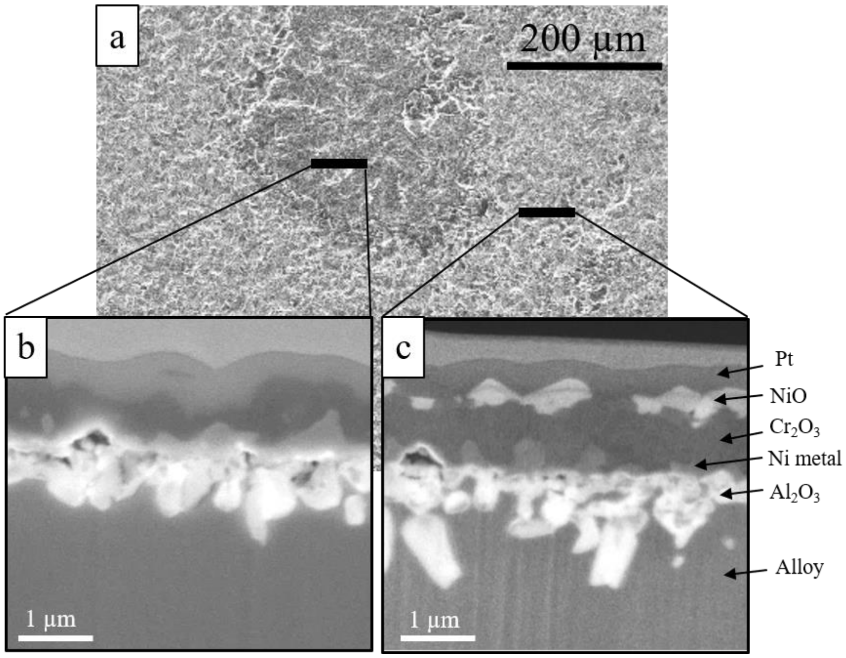

Figure 5.5: SEM images of Alloy 1 oxidized at 1000ºC for 30 minutes, showing cross-sections from two different surface contrast regions. Cross-sectional images are taken from b) the "dark" region seen on the surface and c) the "bright" region. Images were taken using a TLD detector in SE mode, with an accelerating voltage of 5 kV.

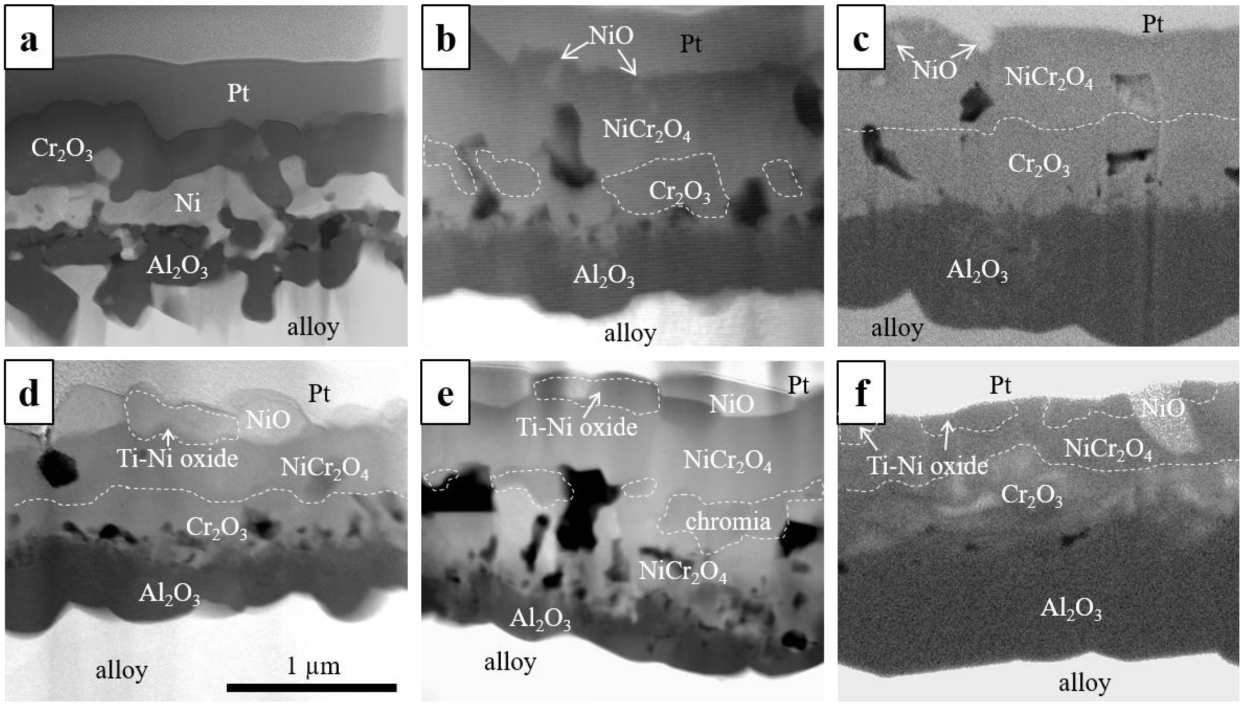

Figure 5.6: Cross-section SEM images, taken using ETD detector in SE mode with 2 kV accelerating voltage, of Alloy 1 (a,b,c) and Alloy 3 (d,e,f) oxidized at 1000 ºC for 30 minutes, 2 hours, and 32 hours at the same magnification. Oxide phases are labelled, and in some cases outlined, for increased clarity.

Upon oxidation of the Ti-doped Ni-26Cr-10Al alloys (Alloys 2 and 3), the same major oxide phases and relative oxide layer thicknesses as those present on the un-doped NiCrAl alloy (Alloy 1) were observed. Al_2O_3 layer thickness at various oxidation times were similar for Alloys 1-3 (**Figure 5.8)**. However, the formation of Ti-rich phases at the surface of the scales grown on Alloys 2 and 3 at longer oxidation times was noted. After 5 minutes at 1000 °C, a continuous Cr_2O_3 layer formed on the surface, with discontinuous Al_2O_3 fingers deeper underneath in the alloy (**Figure 5.4b)**. Compared to the Ti-free Alloy 1, the Cr_2O_3 layers on Alloys 2 and 3 were slightly thicker (~0.40 µm versus 0.25 µm), while the depth of the Al_2O_3 fingers and the distance they had precipitated beneath the Cr_2O_3 were nearly identical on Alloys 1-3. After 30 minutes at 1000 ^{o}C, two regions were observed. Similar to the scales on the un-doped alloys, the presence or absence of NiO grains on the surface of the oxide scale distinguished the two regions. The "bright region" consisted of NiO grains on the surface, a layer of $NiCr_2O_4$, then a layer of Cr_2O_3 above a thin, continuous Al_2O_3 layer **(Figure 5.6d)**. The "dark region" consisted of the same phases but without NiO grains on the surface. On Alloy 2, a thin region of Ti enrichment on the scale surface was detected, and on Alloy 3 larger grains of a Ti-Ni-rich oxide were identified at the surface between the NiO grains where present. Large pores could also be seen in the $NiCr_2O_4$ and Cr_2O_3 layers, and smaller pores were visible near the top of the Al_2O_3.

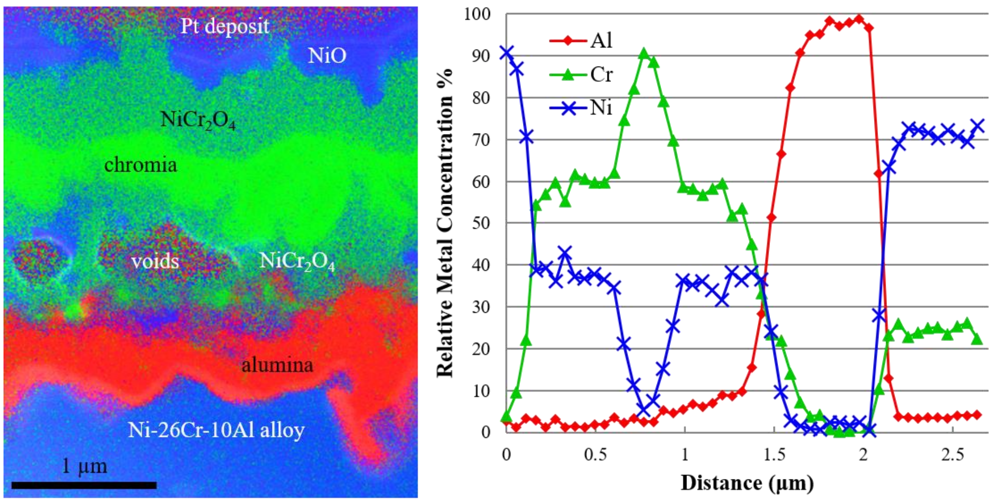

Figure 5.7: Combined EDS map (left) of scale cross-section from Alloy 1 oxidized for 2 hours at 1000 ºC, with Al shown in red, Cr shown in green, and Ni shown in blue (oxygen content is not shown). A qualitative EDS profile of the relative metal composition of Ni, Cr, and Al perpendicular to the alloy surface from the top surface of the scale into the alloy is shown to the right.

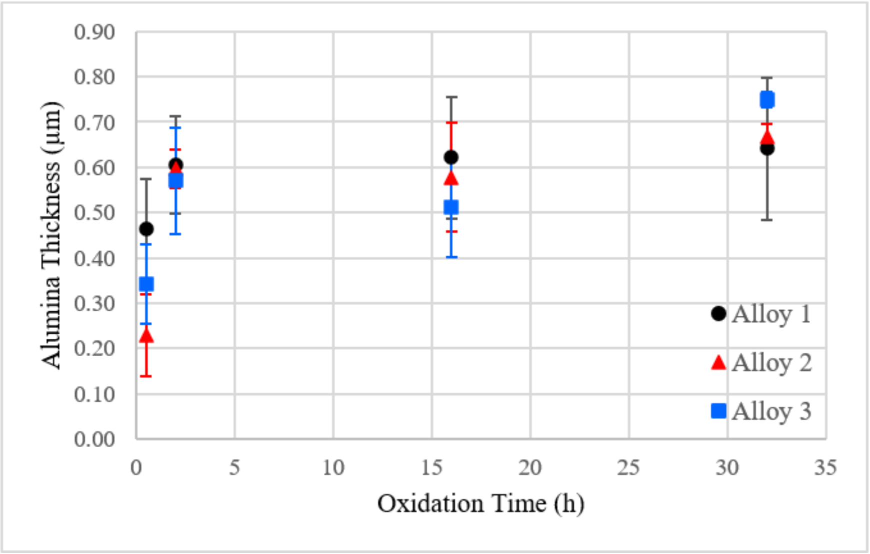

Figure 5.8: A plot of average alumina layer thickness versus oxidation time at 1000 °C. Measurements were made at several locations on each sample using FIB cross-sections.

Dispersed “nodules” were observed (**Figure 5.9a**) on the surfaces of the Ti-containing Alloys 2 and 3 after 30 minutes of oxidation, and grew in size as the oxidation time increased. The nodules consisted of a thick Ti-Ni-rich oxide protruding outward and inward above continuous $NiCr_2O_4$, chromia, and alumina layers (**Figure 5.9b)**. Small dark particles were observed locally under the nodules, and were found, using APT, to be rich in Ti, N, and C. After 2 hours of oxidation, away from the large nodules, NiO islands were still present on the surface, embedded in a layer of $NiCr_2O_4$. Again, a thin Ti-rich layer was detected at the surface of the scale of Alloy 2, and the Alloy 3 surface exhibited larger Ti-Ni-rich oxides **(Figure 5.6e)**. Discontinuous Cr_2O_3 grains could be seen in the middle of the $NiCr_2O_4$ on both alloys. APT analyses revealed that Ti segregated to grain and interphase boundaries within the chromia and $NiCr_2O_4$ layers (**Figure 5.10**). Below the $NiCr_2O_4$ layer, a continuous Al_2O_3 layer was slightly thicker and more continuous than that observed after 30 minutes of oxidation. Porosity was present in the lower part of the $NiCr_2O_4$ layer and around the Cr_2O_3 grains, and some smaller pores could still be seen near the top of the alumina. After 8 hours of oxidation, the majority of the surface on both Ti-doped alloys was covered in the $NiCr_2O_4$ layer, with interspersed embedded NiO grains. Below the $NiCr_2O_4$ layer, a continuous layer of Cr_2O_3 was present, and the continuous alumina layer had grown thicker. Porosity was observed in the $NiCr_2O_4$ layer near the $NiCr_2O_4$-chromia interface. After 32 hours, extensive spalling was visible on the alloy surfaces. On the remaining oxide, the $NiCr_2O_4$ and Cr_2O_3 layers were still present, and the Al_2O_3 layer had grown noticeably thicker **(Figure 5.6f)**. Scarce NiO particles remained on each surface, while the Ti-Ni-rich oxide grains grew on the scale surfaces of the high-Ti alloy.

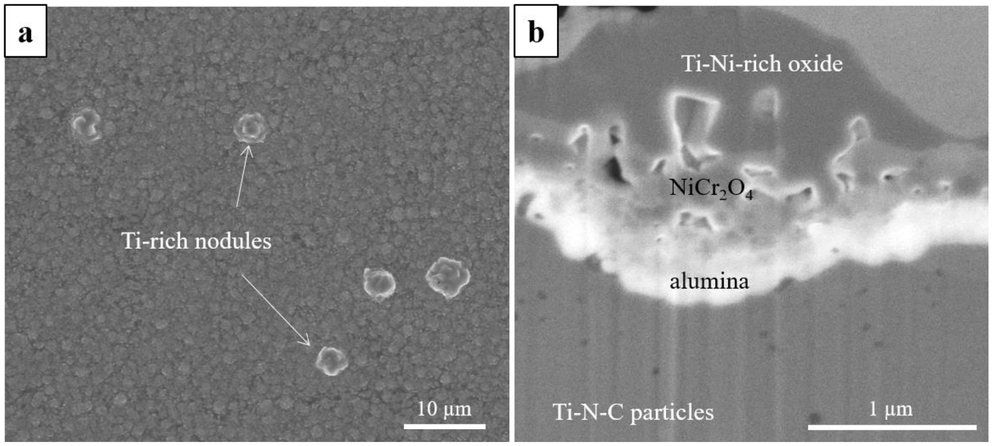

Figure 5.9: a) SEM image of the surface of Alloy 3 alloy oxidized for 2 hours at 1000 ºC. The Ti nodules could be seen on both of the Ti-containing alloys after 30 min of oxidation and grew with increasing oxidation time. b) SEM cross-section image of a nodule, using a TLD detector in SE mode with 5 kV accelerating voltage.

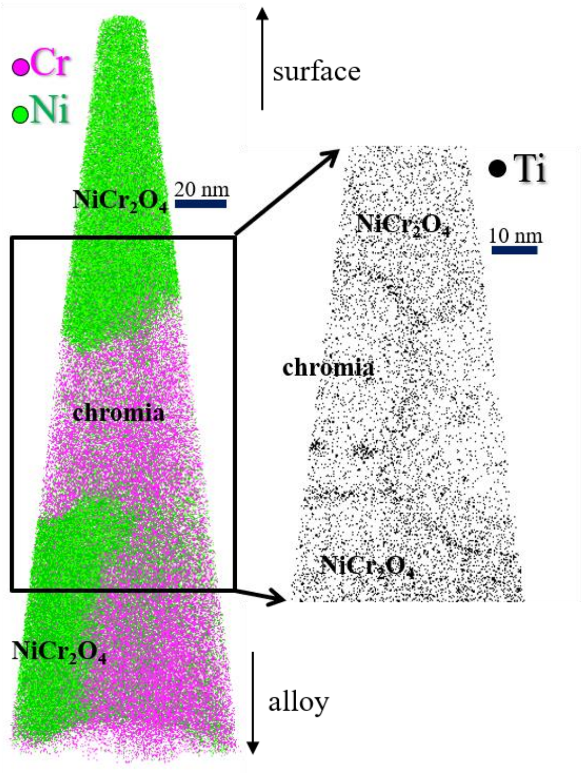

Figure 5.10: APT reconstruction of a volume prepared within the Cr_2O_3 and $NiCr_2O_4$ layers of a scale grown on Alloy 2 alloy after 2 hours of oxidation. In the reconstruction on the left, chromium ions are shown in pink and Ni ions are shown in green. In the 5 nm thick slice on the right, Ti ions are shown in black.

5.4 Discussion

The overall behavior and scale evolution described here, i.e. the development of a continuous Al_2O_3 layer below a Cr_2O_3 layer observed for Alloys 1-3, is consistent with previous work by Giggins and Pettit [3], Nijdam *et al.* [24, 224], and Hu *et al.* [78] on transient oxidation of alloys with similar composition (Ni-(26-30) % Cr –(8-11)%Al). However, the observations and interpretations of the very initial development of the oxide scale differ. In the current study, observations of the oxide scale after 5 minutes at 1000 °C (**Figure 5.4**) revealed that initially an outer layer of Cr_2O_3 formed, with discontinuous Al_2O_3 particles below, in agreement with Hu *et al.* [78]. The initial formation of Cr_2O_3 depleted the alloy of Cr. The continuous Cr_2O_3 layer also contained a non-negligible amount of Al (~7 at.% Al measured by APT), resulting in the depletion of aluminum in the alloy directly below the Cr_2O_3 layer. Consequently, internal Al_2O_3 grains precipitated at a fixed distance beneath this depletion layer as oxygen diffused into the alloy [225]. The Al_2O_3 grains continued to grow into the alloy to form elongated "fingers" (**Figure 5.3b, Figure 5.4, and Figure 5.5**). Elongated Al_2O_3 precipitates are well-documented in literature, and their evolution depends on the relative fluxes of aluminum and oxygen at the inner Al_2O_3 / metal interface [226]. The thickening Cr_2O_3 layer reduced the oxygen flux through the scale and into the alloy with time, allowing Al to diffuse to the scale-alloy interface and form additional Al_2O_3 grains rather than grow the Al_2O_3 fingers. Eventually, a continuous layer formed, as also reported in [18, 226]. The coalescence into a dense, continuous layer trapped the depleted Ni metal above, which is consistent with prior observations [24, 78]. An alternate explanation for the trapped Ni metal comes from extrusion of soft, depleted nickel upon the volume increase associated with Al_2O_3 formation [227, 228]. This creep mechanism might drive the transport of metal to the scale surface for dilute binary alloys that form single-phase scales, but in the case of ternary alloys that form multiple oxide layers, it seems unlikely extrusion would occur. Additionally, the thicknesses of trapped Ni were similar for the Ni-26Cr-10Al alloy oxidized for 10 minutes and for 30 minutes **(Figure 5.11)**, despite significant differences in Al_2O_3 morphology.

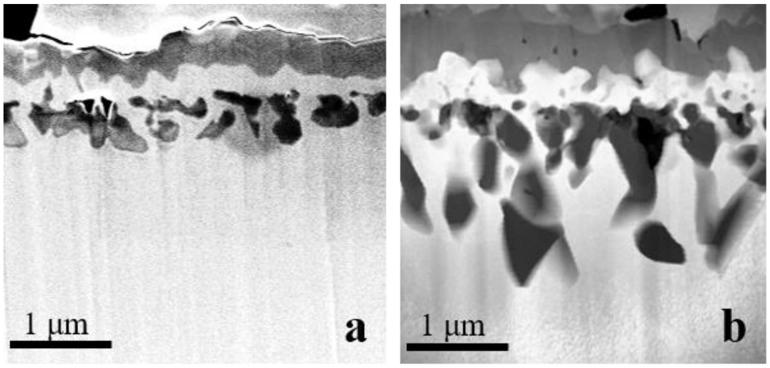

Figure 5.11: STEM dark field images of FIB cross-sections of Alloy 1 alloy oxidized for a) 10min and b) 30 minutes at 1000 ºC. The ratio of area of alumina/ area of trapped Ni in each image is 1.6 for (a) and 2.5 for (b).

After some time, NiO particles formed on regions of the scale surface above the Cr_2O_3, as previously reported [78]. As oxidation progressed, a layer of $NiCr_2O_4$ formed between the NiO and Cr_2O_3. This layer is inferred to occur by solid state reaction between diffusing Ni from the Ni pockets trapped between the Cr_2O_3 and Al_2O_3 and the Cr_2O_3 layer. We hypothesize that the depleted Ni grains evolved by two mechanisms. Ni diffused to the surface, feeding the outer NiO and $NiCr_2O_4$ layers, in agreement with [24, 78]. This upward diffusion is consistent with the formation of large voids between the Cr_2O_3 and Al_2O_3 observed at intermediate oxidation times (2 and 8 hours) and the growth of the $NiCr_2O_4$ layer above the Cr_2O_3 layer. The trapped Ni metal also oxidized and further transformed by solid-state reaction with the nearby Cr_2O_3 phase to form $NiCr_2O_4$ below the Cr_2O_3, as previously reported [78]. This is possibly enabled by concurrent upward Cr diffusion and downward oxygen diffusion. Thermodynamically, $NiCr_2O_4$ was not expected to form below Cr_2O_3 since it is relatively less stable [229]. $NiCr_2O_4$ likely formed in this region at short oxidation times for kinetic reasons or due to a shallow gradient of oxygen activity maintained through a region with large pores. We note that in addition to the spatial re-arrangements of the oxide phases following the establishment of P_{O2} gradient, the thickening of the $NiCr_2O_4$ and Cr_2O_3 layers also required upward Ni and Cr fluxes from the alloy through the continuous Al_2O_3, Cr_2O_3, and $NiCr_2O_4$ layers.

The present results suggest that Ti additions do not have a significant effect on the overall scale thickness or the major oxide phases formed and their morphologies up to 32h of oxidation. At the shortest oxidation times, before a continuous Al_2O_3 layer was formed, the Ti-doped alloys exhibited thicker layers of Cr_2O_3, consistent with prior claims that Ti accelerates the kinetics of Cr_2O_3 layer growth [221-223]. However, the Al_2O_3 growth kinetics upon formation of a continuous layer were not significantly changed by Ti (**Figure 5.7**). The Ti-enriched surface and Ti-rich oxides observed on the surfaces of the scales grown on the Ti-containing alloys indicated that Ti actively diffused towards the scale surface along grain boundaries and interfaces. This is consistent with a “reactive element”-type effect [128], however $NiCr_2O_4$, Cr_2O_3, or Al_2O_3 growth kinetics did not seem to be affected when comparing the scales on the Ti-free and Ti-containing alloys. Prior work on Fe-20Cr-10Al (at.%) alloys also concluded that titanium does not have a significant effect on alumina growth kinetics [97]. On the other hand, the discrepancy with Santoro *et al.* [203] ‘s conclusions that Ti changes the oxidation kinetics of γ-Ni-10Al alloys may be explained by differences in alloy composition; without Cr, the level of aluminum required to transition to a continuous scale rather than internal precipitates is much higher, so the phases and morphology of the oxide scale formed were significantly different than those seen in the current study. When comparing alloys close to the transition for continuous Al_2O_3 growth, the oxidation behavior is much more sensitive to the aluminum concentration and any fluctuation in Al concentration than the small additions of Ti. Finally, it is worth noting that for the alloys studied here, weight gain measurements alone would have led to inaccurate conclusions. The behavior of the un-doped alloy would have been dominated by the low-Al regions which do not form a continuous alumina layer, giving the appearance of a strong, beneficial Ti effect on oxidation behavior.

One significant difference in oxidation behavior of the Ti-containing alloys was the formation of Ti-rich oxides at the scale/gas interface, and localized Ti-rich oxide nodules. The dispersed TiN particles observed on the un-oxidized alloys were of similar number density and size as the nodules observed on the surface of the oxidized samples (**Figure 5.8a**). As these particles oxidized, it is likely that increased local oxidation occurred due to cracking caused by the large volume change as TiN transformed to TiO_2 [148, 151, 230]. During oxidation of the TiN particles, some nitrogen was rejected into the matrix. Small Ti-N-C particles then precipitated in the matrix under the scale in the areas of nitrogen enrichment. These particles below the scale became enveloped by the inward growing Al_2O_3 layer over time. The local variations in scale thickness around the Ti-rich nodules could result in stresses in the scale, and likely contributed to the accelerated spallation behavior of the titanium-doped alloys. Several superalloy and coating studies [192, 221, 231, 232] previously observed growth of titanium oxides on the surface of the scales, and increased spalling behavior with higher Ti content. This is consistent with the design trend of reducing the titanium content to improve oxidation behavior of modern superalloys. The qualitatively inferior spalling behavior observed on the Ti-alloys at longer oxidation times in the current study seems to justify this trend.

5.5 Conclusions

The scales developing on four model alloys, Ni-26Cr-10Al-(0,0.6,1.7)Ti (at%) and Ni-26Cr-12Al, during oxidation at 1000 ^{o}C in a 20% O_2-Ar atmosphere were characterized using scanning electron microscopy, transmission electron microscopy, and atom probe tomography. The following conclusions were reached:

- On the un-doped NiCrAl alloys, NiO, $NiCr_2O_4$, Cr_2O_3, and Al_2O_3 layers formed and developed over time, consistent with previous studies on the transient oxidation of alloys of similar composition. In regions of the alloy with low Al composition, internal alumina fingers formed which extended into the alloy, while in regions with high Al composition, the alumina transitioned into a continuous layer which grew with increasing oxidation time.
- For similar Al and Cr composition in the base alloy, Ti addition did not affect the kinetics and morphology of the protective oxide phases (Al_2O_3 and Cr_2O_3) in the early stages of oxidation, up to 32 hours at 1000 ^{o}C.
- Ti diffused upward toward the scale/gas interface along interfaces and grain boundaries within the oxide scale, becoming enriched at the scale surface and forming Ti-rich oxides with sufficient Ti level in the alloy.
- TiN particles present in the Ti-doped alloys oxidized and experienced large increases in volume, leading to thick local oxide “nodules” which are potentially starting sites for scale spallation.

CHAPTER 6:

Conclusions and Future Directions

This work has focused on expanding our understanding of dopant effects on high temperature oxidation behavior. Comparing the effects of different dopants in prior literature is difficult due to the complexity of alloy compositions. In addition, oxidation typically involves many intertwined processes such as the evolution of microstructure, phase transformations, and changes in scale transport, making it challenging to determine exact mechanisms of dopant effects. To overcome these limitations and establish the key mechanisms at play, the current work used model NiAl and NiCrAl alloys doped with only one or two dopant elements to isolate their effects. A focus was placed on separating the effects of dopant additions on transient alumina scale development and steady-state alumina transport. The main findings from each of these areas are summarized below. Open questions that arose from this work and future directions for research are also addressed.

6.1 Dopant Effects on Transient Oxidation

Prior work has linked the addition of dopant elements to changes in the length of transient oxidation. However, there are conflicting messages concerning the rate of metastable to α-Al_2O_3 transformation for various dopants, especially on alloys with complex compositions. The mechanisms by which dopants alter the alumina transformation rate are also not clearly established. Pertaining to the effects of Si, Ti, and Y on transient NiAl oxidation, the following conclusions were reached:

- Si-, Ti-, and Y-doping do not affect the microstructure of the θ-Al_2O_3 layer.
- Si doping accelerates the outward growth of θ-Al_2O_3.
- Doping NiAl with Ti accelerates the θ- to α-Al_2O_3 transformation by reducing the incubation time for nucleation and increasing nucleation rate in the initial stages of oxidation.
- While increasing the incubation time for nucleation compared to the un-doped alloy, doping NiAl with Si accelerates the θ to α alumina transformation by accelerating the lateral growth rate of α-Al_2O_3 through the θ-Al_2O_3 layer.
- The addition of Y had little effect on the overall θ- to α-Al_2O_3 transformation rate.
- Co-doping NiAl with Ti+Y or Si+Y had no additional effect on the transformation rate beyond the effects of the single-doped Ti and Si alloys respectively.
- On the Ti-containing alloys, a Ti-rich layer was detected at the oxide-metal interface at the shortest oxidation times, but no segregation or partitioning of the dopants was otherwise observed.
- Doping NiAl with Ti suppressed interfacial void formation.

These results indicate that the length of transient oxidation can be tuned with the addition of various dopant elements, which has implications for both alloy design and modelling oxidation kinetics. Understanding how certain dopants reduce the length of transient oxidation may enable the design of alloys that quickly form a protective α-Al_2O_3 scale over a range of temperatures.

Measurements of nucleation and lateral growth rate of α-Al_2O_3 during transient oxidation can be used to develop more accurate predictive models of oxidation kinetics and component lifetime.

6.1.1 Research Opportunities

Though the current work helped clarify that different dopant elements can affect the transient nucleation/growth behavior of α-Al_2O_3 in different ways, several unknowns and limitations remain evident. Mechanisms for the effect of Si on lateral α-Al_2O_3 growth and Ti on α-Al_2O_3 nucleation were proposed in Chapter 3, but should be confirmed with further experimentation. In addition, the link between transient nucleation/growth rates and fully-transformed α-Al_2O_3 scale microstructure should be investigated. Additional experiments pertaining to these topics are needed to develop more accurate models of oxidation kinetics that account for dopant effects and the relationship between nucleation/growth rate, transformation rate, and scale microstructure.

1. It was shown that various dopants changed the thickness of the θ-Al_2O_3 layer and proposed that aliovalent dopants such as Si^{4+} likely changed the concentration of cation vacancies, thereby changing the lateral growth rate of the α-Al_2O_3 patches. To validate this mechanism, further experiments could be performed with NiAl doped with other aliovalent dopants such as Zr^{4+}/ Hf^{4+} and Mg^{2+} to verify their effects on oxide growth. Specifically, the 4+ ions may be expected to increase cation vacancies and accelerate θ-Al_2O_3 layer growth and α-Al_2O_3 lateral growth, while the 2+ ions may be expected to have the opposite effect, resulting in fewer cation vacancies, thinner θ-Al_2O_3 layers, and slower α-Al_2O_3 lateral growth. In addition, density functional theory (DFT) or mass action analysis (as in [184]) could be used to predict defect energies and concentrations in θ-Al_2O_3 doped with different ions.

2. Previous studies have shown Y additions to delay the θ- to α-Al_2O_3 transformation, yet no significant effect of Y on alumina transformation or α-Al_2O_3 nucleation/growth was observed in the current work. This was thought to be the result of the low concentration of Y used (0.05 at%). To confirm this hypothesis, additional nucleation/growth experiments could be undertaken using higher Y concentrations.
3. The addition of Ti was observed to reduce the incubation time and increase the nucleation rate of α-Al_2O_3 in the early stages of oxidation. The Ti-rich layer observed at the alumina-metal interface at short oxidation times was suggested to act as a seeding layer that promoted α-Al_2O_3 nucleation. Prior literature shows that seeding layers isostructural with α-Al_2O_3, such as Cr_2O_3, promote the nucleation of α-Al_2O_3 grains and faster transformation to α-Al_2O_3 [27]. Further characterization of the Ti-rich layer could be done to identify the phase of this layer, and confirm if it is isostructural with α-Al_2O_3.
4. Several previous studies suggested that the steady-state α-Al_2O_3 scale grain size may be determined by nucleation/growth behavior during alumina transformation in the transient oxidation stage [27, 63]. However, no experimental correlation currently exists. The current work showed that different alloying elements have varied effects on α-Al_2O_3 nucleation and growth on NiAl. Longer oxidation experiments could be done on the same NiAl alloys to establish a fully α-Al_2O_3 scale. The alumina grain size could be measured in each alumina scale using techniques such as TEM or EBSD, and compared to the nucleation/growth rates of α-Al_2O_3 to ascertain any relationship. As suggested previously [27], increased nucleation of α-Al_2O_3 should lead to a finer-grained scale, and result in faster oxidation kinetics. Thus, the Ti-doped NiAl alloys, which were found to have increased α-Al_2O_3 nucleation, would be expected to have smaller α-Al_2O_3 grain sizes in

the fully-transformed scale than the un-doped NiAl, and should also have faster steady-state oxidation kinetics. Doping with Si was shown to accelerate the lateral growth rate of the α-Al_2O_3 patches, so the fully transformed α-Al_2O_3 scale on Si-doped NiAl would be expected to have larger grains and slower steady-state oxidation kinetics than that on the un-doped alloy.

6.2 Dopant Effects on Steady-State Alumina Transport

One of the primary ways dopants reduce oxidation rate during steady-state α-Al_2O_3 growth is by inhibiting upward Al transport. Prior studies showed that alumina scales on doped alloys grow primarily inward via oxygen grain boundary transport. However, the extent to which different dopant elements reduce both Al and O transport along scale grain boundaries was not directly compared. We discussed the effects of Y and Ti on Al and O grain boundary transport through alumina scales on NiAl alloys. The differing effects of Y and Ti on Al and O transport were consistent with oxidation rates measured on each alloy. The following conclusions were reached:

- Ti slightly reduces the oxidation rate, while Y and Ti+Y significantly reduce the oxidation rate when alloyed with NiAl, as evidenced by weight gain measurements over time and oxide thickness.
- Ti does not significantly affect upward Al transport, but does reduce inward oxygen transport along the scale grain boundaries.
- Y decreases both upward Al transport and inward O transport along the alumina grain boundaries.

- Co-doping with Ti+Y reduced both oxidation rate and inward O transport slightly more than doping with Ti or Y alone.
- ^{18}O was detected along grain boundaries within the scale as a result of grain boundary migration during oxidation.

Clarifying the effects of different elements on both Al and O transport through alumina scales is a critical step for developing predictive models of oxidation rate and component lifetime. Knowledge of the effects of different dopants can lead to the design of highly oxidation-resistant alloys in the future. In addition, stress development and relaxation processes in the scale can be modelled more accurately if dopant effects on transport and microstructure are identified, leading to more accurate lifetime predictions.

6.2.1 Research Opportunities

The current work confirmed that different dopant elements, in this case Ti and Y, have varied effects on the individual magnitudes of Al and O transport. However, several limitations of the Al/O transport experiments became apparent. The diffusivity of Al and O in the presence of dopants could not be compared directly in the current work, since the Al and O flux were measured using different methods. In addition, though the $^{18}O/^{16}O$ tracer experiment provided useful information about the scale microstructure and relative inward oxygen flux, it produced several open questions about the evolution of scale microstructure during oxidation. Additional experiments are proposed below to elucidate some of these unknowns.

1. Previous studies have measured the diffusivity of O and Al in polycrystalline Al_2O_3 using concentration profiles of ^{18}O and ^{26}Al isotopic tracers [141]. To compare Al and O grain

boundary diffusivity in thermally grown alumina scales, it would be useful to perform isotopic tracer experiments for both O and Al under the same oxidation conditions. Then, changes in the diffusivities of Al and O in the presence of dopants could be compared directly. We hypothesize that the same relative changes would be observed (i.e. Y would reduce both Al and O diffusivity, while Ti would reduce only O diffusivity). Based on previous studies of bulk Al_2O_3 [141], we hypothesize that the Al diffusivity is larger than O diffusivity.

2. It remains difficult to determine the mechanism for dopant effects on Al/O grain boundary flux since the diffusing species in Al_2O_3 has not been clearly established. Several possibilities were proposed in Chapter 4. To briefly restate them, proposed mechanisms included site-blocking, altering defect chemistry, changing the electronic structure of the alumina scale, or modifying the local bonding environment in the grain boundary. To test the first two mechanisms, transport experiments could be performed with additional dopant elements using a range of ion sizes and valences. To investigate the second two mechanisms, computational methods such as DFT could be used to predict differences in the electronic properties of the Al_2O_3 scale, and to calculate the bond energy in the presence of various dopants, as has been done for Y [136].
3. As discussed in Chapter 4, the ^{18}O signal observed on the grain boundaries within the scale could arise in several ways. New oxide may form on the grain boundaries due to the concurrent upward Al and downward O diffusion. The formation of new oxide at the boundaries is thought to explain the observed development of compressive stress in growing oxide scales [156]. Alternatively, the grain boundaries may migrate during oxidation due to thermal coarsening, or stress relaxation processes such as creep. If the

grain boundaries are migrating while ^{18}O is diffusing along them, this could result in the relatively thick regions of ^{18}O observed at the boundaries in the NanoSIMS cross-sections. To verify which of these processes is occurring, several additional experiments could be done. Performing a similar 2-stage $^{16}O/^{18}O$ tracer experiment, *in situ* stress could be measured during the 2nd stage when the scale is exposed to ^{18}O. Then, growth stress could be compared to the strain expected from the width of ^{18}O on the grain boundaries assuming it is new oxide. To analyze stress relaxation and thermal coarsening processes, a scale which has previously been exposed to $^{16}O/^{18}O$ (effectively marking the original grain boundaries) could be held at temperature in a non-oxidizing environment to determine if significant thermal coarsening occurred. Under the same conditions, a stress could be applied to verify if the microstructure significantly changes due to stress relaxation. Characterizing the evolution of scale microstructure due to both thermal coarsening and stress relaxation would help to clarify the origin of ^{18}O signal.

6.3 Ti Effects on Multi-phase Scales

Ti is a commonly used as a minor alloying element in γ-Ni alloys to promote strengthening, but reports of its effect on oxidation behavior vary widely. Some studies of complex superalloys and coatings observed increased spalling behavior with higher Ti contents, yet others reported reduced oxidation rates on Ti-doped alloys. To clarify the effect of Ti on the oxidation of alloys that form multi-phase oxide scales, four model alloys, Ni-26Cr-10Al-(0,0.6,1.7)Ti (at%) and Ni-26Cr-12Al, were investigated after oxidation at 1000 ºC. The resulting surface oxides were characterized using scanning electron microscopy, transmission electron microscopy, and atom probe tomography. The following conclusions were reached:

- On the un-doped NiCrAl alloys, NiO, $NiCr_2O_4$, Cr_2O_3, and Al_2O_3 layers formed and developed over time, consistent with previous studies on the transient oxidation of alloys of similar composition. In regions of the alloy with low Al composition, internal alumina fingers formed which extended into the alloy, while in regions with high Al composition, the alumina transitioned into a continuous layer which grew with increasing oxidation time.
- For similar Al and Cr composition in the base alloy, Ti addition did not affect the kinetics and morphology of the protective oxide phases (Al_2O_3 and Cr_2O_3) in the early stages of oxidation, up to 32 hours at 1000 ^{o}C.
- Ti diffused upward toward the scale/gas interface along interfaces and grain boundaries within the oxide scale, becoming enriched at the scale surface and forming Ti-rich oxides with sufficient Ti level in the alloy.
- TiN particles present in the Ti-doped alloys oxidized and experienced large increases in volume, leading to thick local oxide “nodules” which are potentially starting sites for scale spallation.

6.3.1 Research Opportunities

The results of the current work suggested that Ti additions do not have a significant effect on the oxidation kinetics of NiCrAl alloys that form continuous alumina scales. However, Ti interactions with impurities in the alloy, in this case nitrogen, led to the formation of nitrides that were found to oxidize rapidly. It was proposed that these impurity interactions may play a major role in affecting oxidation resistance. Several additional experiments could be done to clarify the effects of the Ti-impurity interactions on oxidation behavior, as described below:

1. The presence of nitrogen impurities in the NiCrAlTi alloys led to the formation of TiN particles that upon oxidation resulted in thick local regions of the oxide scale. It was hypothesized that these thicker regions in the scale may be points of stress concentration, and the cause of increased spalling reported in literature for Ti-containing alloys. To verify, longer cyclic oxidation experiments could be performed to compare the spalling behavior of un-doped NiCrAl to that of the NiCrAl+Ti. An additional NiCrAl+Ti alloy with higher purity and minimal concentrations of N/C could be used to confirm if increased spalling occurs due to TiN/TiC particles, or if it is caused by Ti in some other way.
2. The formation of a continuous alumina scale was quite sensitive to Al concentration in the alloy. In regions of comparable Al concentration, continuous alumina scales were formed on both NiCrAl and NiCrAl+Ti, and Ti additions did not significantly affect the growth kinetics of this alumina layer. In our subsequent work on NiAl alloys, Ti additions were found to promote α-Al_2O_3 nucleation during transient oxidation, and to reduce inward O flux during steady-state α-Al_2O_3 growth. Considering these results, we hypothesize that Ti may promote the formation of a continuous α-Al_2O_3 scale on NiCrAl alloys with lower Al concentrations than the current work (<10 at% Al), by promoting Al_2O_3 nucleation, and reducing inward O flux leading to shorter Al_2O_3 “fingers”. To test this hypothesis, NiCrAl alloys with slightly lower Al concentrations (~6-8 at%) could be oxidized for short times (~1-30 minutes) and compared with the behavior of the same base alloy with Ti additions.

APPENDICES

APPENDIX I: EBSD Analysis of NiAl Alloys

I.i Background

During transient oxidation of NiAl alloys, the surface oxide scale consists of metastable Al_2O_3 phases before transforming to the stable, slow-growing α-Al_2O_3 phase after longer exposure times. This transformation is governed by the nucleation and radial growth of α-Al_2O_3 nuclei through the metastable Al_2O_3 layer. Chapter 3 of this dissertation focused on clarifying the effects of alloy composition on the nucleation/ growth aspect of the alumina transformation on NiAl-based alloys. However, several other factors beyond alloy composition can influence α-Al_2O_3 transformation in thermally grown scales. For example, NiAl substrate orientation was found in an initial oxidation experiment to affect α-Al_2O_3 nucleation rate (**Figure I.1**), confirmed by previous literature [53, 60, 61, 179]. To control for this orientation effect, only NiAl grains of the same orientation were compared in Chapter 3, and the same samples were re-polished for subsequent oxidation experiments. The goal of this work was to characterize the polycrystalline NiAl samples prior to oxidation using EBSD, so that grains of similar orientations could be examined.

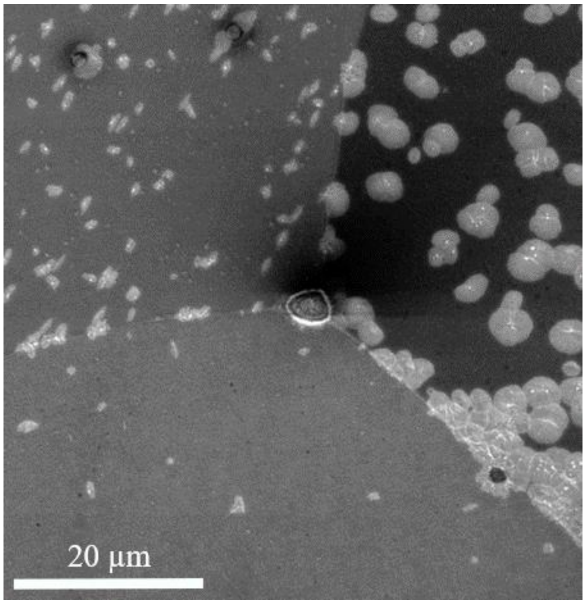

Figure I.1: Triple junction of 3 β grains on the β-NiAlTiY alloy oxidized for 1h at 950 °C. The bright areas correspond with the α-Al_2O_3 phase while the darker areas are θ-Al_2O_3. Significant differences in the number density of α-Al_2O_3 nuclei can be seen on each NiAlTiY grain.

I.ii Experimental

Single phase polycrystalline β-NiAl alloys with nominal compositions listed in **Table 3-1** were sectioned, homogenized at 1200 °C in argon gas for at least 20 hours, and subsequently quenched in water. Prior to oxidation, samples were ground with SiC paper using 320, 600, 800, then 1200 grit, polished with 3 and 1 µm diamond slurries, and finally colloidal silica. Ultrasonic cleaning in ethanol was performed between each consecutive grinding and polishing step, and sample surfaces were dried using compressed air.

Samples were tilted to 70° using a 45° pre-tilt holder, and electron back scatter diffraction (EBSD) maps were collected using a TESCAN MIRA3 FEG scanning electron microscope (SEM) equipped with an EDAX Hikari Camera. Approximately 1 mm^2 areas were mapped at an accelerating voltage of 30 keV with the beam intensity set to 18, and a 6-10 µm step size.

I.iii Results and Discussion

EBSD mapping of each alloy revealed uniform polycrystalline microstructures with no dominant texture relative to the surface normal. **Figure I.2** shows a representative EBSD inverse pole figure (IPF) color-coded map and corresponding inverse pole figure for the NiAl alloy. To compare the transient oxidation behavior of similarly oriented grains on each alloy for the experiments in Chapter 3, the (011) orientation was chosen arbitrarily. A tolerance angle of 5-10° was used to select grains with their (011) direction nearly normal to the alloy surface, as shown in **Figure I.2b**.

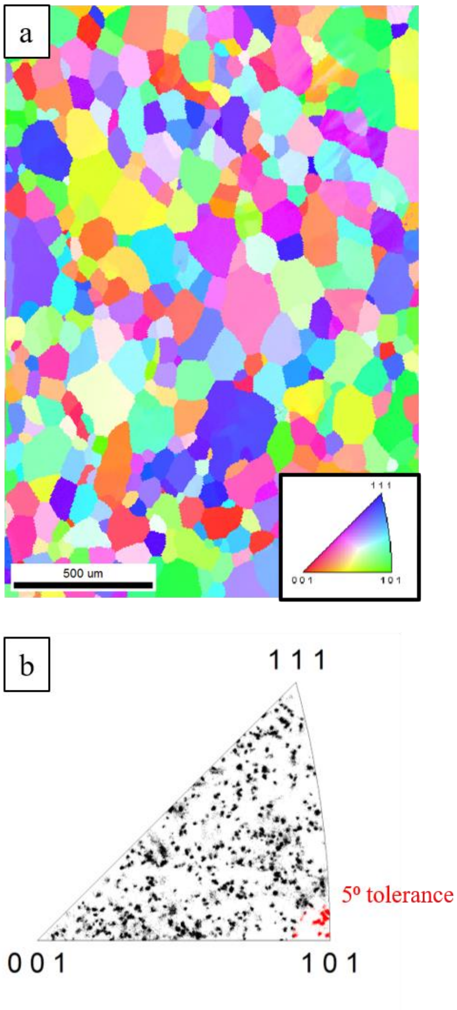

Figure I. 2: a) EBSD inverse pole figure color-coded map of the surface of the NiAl alloy prior to oxidation and b) corresponding inverse pole figure highlighting grains with their surface normal within 5° of the (011) direction.

Grain size varied among the different alloys (**Table I-1**), despite annealing for the same time, but was not thought to have a significant effect on α-Al_2O_3 nucleation and growth. The NiAlY alloy exhibited the largest average grain size, followed by NiAlSiY, NiAl, NiAlSi, NiAlTi, and NiAlTiY. Ti additions seemed to inhibit the coarsening of NiAl grains. This has been observed previously [233], but the mechanism is currently not understood, for example whether Ti reduces diffusivity in NiAl or modifies NiAl grain boundary structure.

Table I-1: Average grain size of each alloy after annealing at 1200 °C for 21 hours.

	grain size (µm)	std dev (µm)
NiAl	345	84
NiAlY	432	63
NiAlTi	204	34
NiAlSi	240	30
NiAlTiY	181	42
NiAlSiY	381	100

APPENDIX II: EBSD Analysis of Al_2O_3 Scale Cross-Sections

I.i. Background

As described in the literature review, Al_2O_3 scales were found to have a texture relative to the scale growth direction [100]. However, it is unclear how Al_2O_3 scale growth and grain orientation may depend on alloy composition. To determine any effect of dopant additions on the Al_2O_3 scale texture in the current studies, proof-of-concept experiments were performed to collect orientation maps of scale cross-sections. Three different methods were attempted:

1) Mechanical cross-section sample preparation
2) FIB lift-out preparation and transmission Kikuchi diffraction (TKD)
3) FIB cross-section preparation on sample edge and standard EBSD

II.ii. Experimental

A single phase polycrystalline β-NiAl alloy with nominal composition listed in Table 3-1 was sectioned, homogenized at 1200 °C in Ar gas for at least 20 hours, and subsequently quenched in water. Prior to oxidation, the sample was ground with SiC paper using 320, 600, 800, then 1200 grit, polished with 3 and 1 μm diamond slurries, and finally colloidal silica. Ultrasonic cleaning in ethanol was performed between each consecutive grinding and polishing step, and sample surfaces were dried using compressed air. The sample was then oxidized at 1200 °C for 100 hours to grow a α-Al_2O_3 scale with an average thickness of 6.2 μm.

II.ii.1 Mechanical cross-section preparation and EBSD

To prepare a mechanical cross-section of the scale for EBSD characterization, the sample was mounted in low-shrinkage epoxy resin with the scale surface toward the middle of the mount in order to protect the scale from damage during subsequent sectioning steps. Next, the hardened mount was sectioned using a low-speed diamond saw set at approximately 300 rpm. To maintain adherence of the surface scale with the metal below, the mount was positioned such that the saw blade first contacted the scale surface and then cut into the metal. After sectioning, half of the original mount was rotated and mounted in epoxy resin so that the sectioned surface was positioned at the surface of the new mount. (Note: this step is not necessary unless a particular mount size is needed for characterization or polishing). Once the new mount hardened, the sectioned surface was ground using 600, 800, then 1200 grit SiC paper, polished with 3 and 1 µm diamond slurries, and a final polishing step was done using colloidal silica. In all polishing steps, the sample was positioned such that the polishing direction went from the scale surface into the metal to maintain scale adhesion to the metal. Ultrasonic cleaning in ethanol was performed between each consecutive grinding and polishing step, and sample surfaces were dried using compressed air.

After polishing, the mount was attached to a 45° pre-tilt SEM stub for imaging and EBSD mapping. Using SEM imaging, a gap was observed between the scale surface and the mount resin. Due to this gap, the scale surface was selectively polished/damaged, and high quality EBSD patterns could not be collected.

II.ii.2 FIB cross-section preparation and TKD/EBSD

Cross-sections of the scale were prepared using a standard FIB lift-out and thinning technique for TEM foil preparation. For TKD data collection, the lift-outs were placed on a pre-tilted holder and back-tilted 20° from horizontal. TKD data was collected using a 30 kV accelerating voltage.

In addition to TKD, standard EBSD mapping was attempted on the same sample. In this case, a cross section of the scale was prepared using FIB near the sample edge to prevent shadowing of the signal to the EBSD camera. The sample was then attached to a pre-tilted sample holder, tilted such that the cut cross-section face was 70° from horizontal, and EBSD maps were collected at an accelerating voltage of 30 kV.

II.iii. Results and Discussion

TKD mapping on the thinned lift-out was successful for limited areas of the lift-out, as shown in **Figure II.1**. TKD background collection is sensitive to sample thickness, thus the slight wedge shape of the thinned lift-out and bending of the lift-out when it reached a certain thickness made it difficult to collect diffraction data for the entire section.

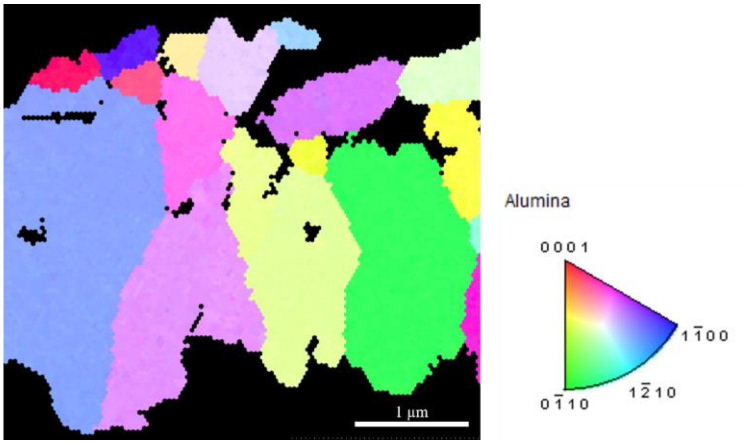

Figure II. 1: TKD inverse pole figure color-coded orientation map of a cross section of the Al_2O_3 scale grown on the NiAl alloy after 100h at 1200 °C. Orientations are shown with respect to the scale surface normal. TKD data was collected at an accelerating voltage of 30 kV.

Standard EBSD mapping on the FIB cross-section prepared on the sample edge was more successful in comparison to the FIB lift-out method for mapping a larger area of the Al_2O_3 scale, as shown in **Figure II.2**.

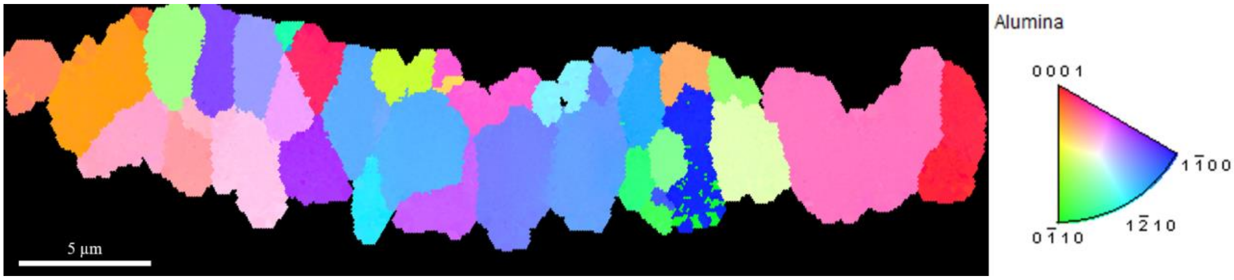

Figure II. 2: EBSD inverse pole figure color-coded orientation map of a cross section of the Al_2O_3 scale grown on the NiAl alloy after 100h at 1200 °C. Orientations are shown with respect to the scale surface normal. EBSD data was collected at an accelerating voltage of 30 kV.

II.iv. Summary

In summary, several methods were explored in order to collect orientation data for the Al_2O_3 scales grown on a NiAl alloy, including mechanical cross-section preparation, FIB lift-out preparation and TKD, and FIB cross-section preparation on the sample edge and EBSD. Each method had trade-offs in terms of the ease of preparation and the statistics of EBSD data collected.

Mechanical cross-section preparation of EBSD samples is desirable because one can prepare large cross-sections that have good statistics in terms of number of grains, and this method is relatively inexpensive. However, the mechanical preparation proved to be challenging to achieve the high-quality surface finish required for the indexing of EBSD patterns. This was likely due to a gap between the epoxy and sample that arose during the mounting step. Several steps could be taken in the future to improve the mechanical cross-section preparation method for EBSD. One possibility is to plate the scale surface with a hard metal such as NiCr prior to sectioning and polishing, so that the scale stays in contact and is protected by the metal during surface preparation. Another improvement could be to maintain an extremely flat sample surface during grinding and polishing by using an automatic grinder/polisher or a manual holder that evens out pressure on the sample surface.

FIB lift-out preparation is a standard method that can provide the necessary surface finish easily with many different materials, and TKD can be performed with relative ease on the same instrument if equipped with an EBSD camera. One problem with this method, however, is that only small sections can be prepared at a time, so getting a large number of grains for improved EBSD statistics would be time intensive and expensive. To improve TKD data collection over a single lift-out, care should be taken to make sure the final lift-out thickness is uniform, and to avoid bending of the lift-out foil as it is thinned.

FIB cross-section preparation near the edge of the sample again is a relatively straightforward way to get a good surface finish for EBSD data collection. One can prepare a slightly larger area than would be attained by the lift-out method. However, this method is still time intensive and expensive to prepare a large enough area for good grain statistics. To improve on this, plasma-FIB could be used to prepare a much larger cross-section in a short amount of time.

APPENDIX III: NanoSIMS Data Analysis

III.i Background

To understand the effects of minor alloying additions on α-Al_2O_3 scale growth rate, the transport of Al and O through the scale were investigated using a few different methods, as described in Chapter 4. One experiment involved exposing samples at 1200 °C first to $^{16}O_2$ and then $^{18}O_2$, and then mapping the distributions of ^{16}O and ^{18}O throughout the Al_2O_3 scale to ascertain where "new" oxide was forming. To map out the different oxygen isotopes, 1 μm thick cross-sections of the Al_2O_3 scales were prepared using a standard FIB lift-out technique on a Thermofisher Helios 650 Nanolab SEM/FIB. The cross-sections were then analyzed using a Cameca NanoSIMS 50 operating with a Cs^+ beam with a current of ~0.2 pA with a spot size of ~50 nm. The secondary mass spectrometer was tuned for ~3000 mass resolving power [209], and the ions of interest were quantified on electron multipliers using pulse counting: the two oxygen isotopes, $^{16}O^-$ and $^{18}O^-$, as well as $^{12}C^-$ to note the position of the Pt deposited on the surface of the alumina during the lift-out process. 20 μm x 20 μm scans were acquired with 512 x 512 pixels, and 10-50 approximately nm "slices" were obtained in depth for each sample. Image analysis was done using L'image software run in IDL to generate ^{16}O, ^{18}O and $^{18}O/^{16}O$ ratio maps and line profiles. MATLAB was used for image segmentation and measurements of the inner oxide layer thickness. This section describes the detailed image analysis procedures for generating the isotope maps and measuring the thickness of the inner oxide layer.

III.ii Data Analysis Procedures

III.ii.1 Isotope and Ratio Maps in L'image and IDL

To generate ^{16}O, ^{18}O, and ^{18}O/^{16}O ratio maps, the raw data (".im" format) was loaded into L'image (developed at LLNL), which was run as a ".sav" file application using IDL Virtual Machine. A deadtime correction of 44 ns was applied, and then images from multiple slices were aligned using the ^{18}O images and the "Auto-Align Cycles" function. ^{16}O and ^{18}O maps were generated using the "Save Images" tab, and aligned images of all slices were saved in black and white contrast (Figure 4.8). To generate overlaid maps of ^{16}O and ^{18}O on the same image (Figure 4.9), the "RGB" tab was used. The logarithm of the ^{16}O signal was added on the blue channel while the log(^{18}O) was added on the red channel. Ratio images were generated by first using the "Define Ratios" tab to define the ratio of ^{18}O/^{16}O (Numerator → 18O, Denominator → 16O, "ADD"), then the "Ratio Images" tab to display the defined ratio map. Line profiles (Figure 4.14) of the ^{18}O/^{16}O ratio were generated by right-clicking the ^{18}O/^{16}O ratio image and selecting "Profiles", with the re-binning function off ("Options" → "Rebin" → "Off").

Finally, for image segmentation and measurement of the inner oxide layer, ^{18}O images of each individual slice were generated in black and white contrast using the "Save Images" tab and saved as ".tif" files.

III.ii.2 Inner Oxide Thickness Measurement in MATLAB

To measure the thickness of the inner oxide layer, the single slice ^{18}O images generated in L'image were further analyzed using MATLAB software. Each ^{18}O image was sectioned into smaller sections, segmented into black and white areas, the inner ^{18}O layer area was measured, and then the thickness was estimated and averaged for all sections and cycles. The following steps summarize the image segmentation and measurement processes performed in the custom MATLAB script “NScycles.m”, which is included at the end of this section.

1. Read in the series of “.tif” ^{18}O images for each slice generated from L’image.
2. Crop and rotate images.
3. Convert images to grayscale values and equalize the histogram for each image.
4. Split each image into 10 sections.
5. Crop sections to inner ^{18}O layer.
6. Segment ^{18}O area in cropped section using “activecontour’ MATLAB function to measure average area of ^{18}O region.
7. Measure line length of ^{18}O layer in section.
8. Estimate inner ^{18}O region thickness of each section by dividing area by line length.

MATLAB “NScycles.m” Script:

```
%measure 18O layer area and line length for all NanoSIMS cycles in given
%data file

clear
clc

%%read in all data%%

numfiles=15; %number of cycles
data=cell(1,numfiles); %create empty cell array
scale=17.4; %pixels/um from imageJ

for k=1:numfiles %read in consecutive .tif files
myfilename=sprintf('NiAl-2_3_18O_%d.tif',k);
data{k}=importdata(myfilename);
end

A=cell(1,numfiles);
angle=-91; %angle of rotation, '-' is CW, '+' is CCW
cropW=910; %crop parameters; choose before running (impixelinfo is helpful)
cropH=250;
```

```
rowstart=90;
colstart=130;

for k=1:numfiles
    a=data{k};
    a=rgb2gray(a); %convert each image to grayscale
    a=imrotate(a,angle);
    a=imcrop(a,[rowstart colstart cropW cropH]); %crop each image
    A{k}=imadjust(a); %equalize histogram for each image
end

%%define sections of interest%%
numsects=10;
sectionNumber=1;
sect=cell(1,numfiles); %empty cell array for section crop
sect18=cell(1,numfiles); %empty cell array for 18O layer crop
sectW=cropW/numsects; %section width in pixels


sectStart=1+sectW*(sectionNumber-1);

for k=1:numfiles
        im=A{k}; %cropped,rotated, and histeq'ed image for each cycle
        sect{k}=im(:,sectStart:sectW*sectionNumber); %cropped section for each cycle
        cropSect=sect{k};
end

%%crop to 18O using peak intensity%%
intSum=sum(sect{1},2); %sum intensity for each row
figure,plot(intSum)
title('click point before 18O peak, then press enter')
[x,y]=ginput;
datacutoff=round(x);

 for k=1:numfiles
    cropSect=sect{k};
    sect18{k}=cropSect(datacutoff:end,:); %crop to 18O layer only using peak intensity
 end

 bw=cell(1,numfiles);
 area=zeros(1,numfiles);
 mask=roipoly(sect18{1}); %choose mask close to 18O layer, R click--'create mask'
 for k=1:numfiles
     cropSect=sect18{k};
     bw{k}=activecontour(cropSect,mask); %segment each cycle using mask
     SE=strel('sphere',3);
     bw2{k}=imclose(bw{k},SE);

     area(k)=bwarea(bw2{k}); %array of areas for each cycle

 end
 avgAreas=mean(area); %avg area of all cycles in pixels^2
 Area=area./(scale^2); %area of each cycle in um^2
 avgA=mean(Area) %avg area of all cycles in um^2 (displayed)
```

```
 Astdev=std(Area) %standard deviation of areas in um^2


 %%find line length using 1st cycle%%

  cropSect1=sect18{1};
       for i=1:sectW
           [M,I]=max(cropSect1(:,i));
           M1(i)=M;
           I1(i)=I;
       end
       I1=double(I1);
       sI1=smooth(I1,0.4,'rloess');

       for j=1:sectW-1 %estimate line length
           l(j)=sqrt(((j+1)-j)^2+abs((sI1(j+1)-sI1(j))^2));
       end
L=sum(l);
linelength=L/scale
Layer18OThickness=(avgAreas/L)/scale

imshow(sect18{1})
hold on
plot(sI1)
hold off
figure, imshow(bw2{1})

%find total oxide thickness from 1st cycle using full width half max
figure,plot(intSum)
title('click point before 1st peak, enter, then after 2nd peak, then enter')
[x1,y1]=ginput;
[x2,y2]=ginput;
x1=round(x1);
x2=round(x2);

%find half-max location on L side
[peaks,locs]=findpeaks(intSum,'MinPeakProminence',500);
hm1=((peaks(1)-intSum(x1))/2)+intSum(x1);
hm2=((peaks(end)-intSum(x2))/2)+intSum(x2);
for l=x1:locs(1)
    if (hm1>=intSum(l))&&(hm1<=intSum(l+1))
        k1=intSum(l);
        k2=intSum(l+1);
        j1=l;
        j2=l+1;
    end
end

%interpolate between pts
m1=(k2-k1)/(j2-j1);
b1=k2-m1*j2;
w1=(hm1-b1)/m1; %x value of L-side hm

%find half-max location on R side
```

```
for m=locs(end):x2
    if (hm2<=intSum(m))&&(hm2>=intSum(m+1))
        k3=intSum(m);
        k4=intSum(m+1);
        j3=m;
        j4=m+1;
    end
end

%interpolate between pts
m2=(k4-k3)/(j4-j3);
b2=k4-m2*j4;
w2=(hm2-b2)/m2;%x value of R-side hm
hold on
plot(w1,hm1,'rx',w2,hm2,'rx')

fwhm=w2-w1; %oxide thickness in pixels
totalOxideThickness=fwhm/scale
```

APPENDIX IV: APT Spectra of θ- and α-Al_2O_3

The following figures include detailed APT bulk spectra obtained from the θ-Al_2O_3 sample analyzed in Chapter 3. The spectra are representative of the data obtained for several θ- and α-Al_2O_3 samples.

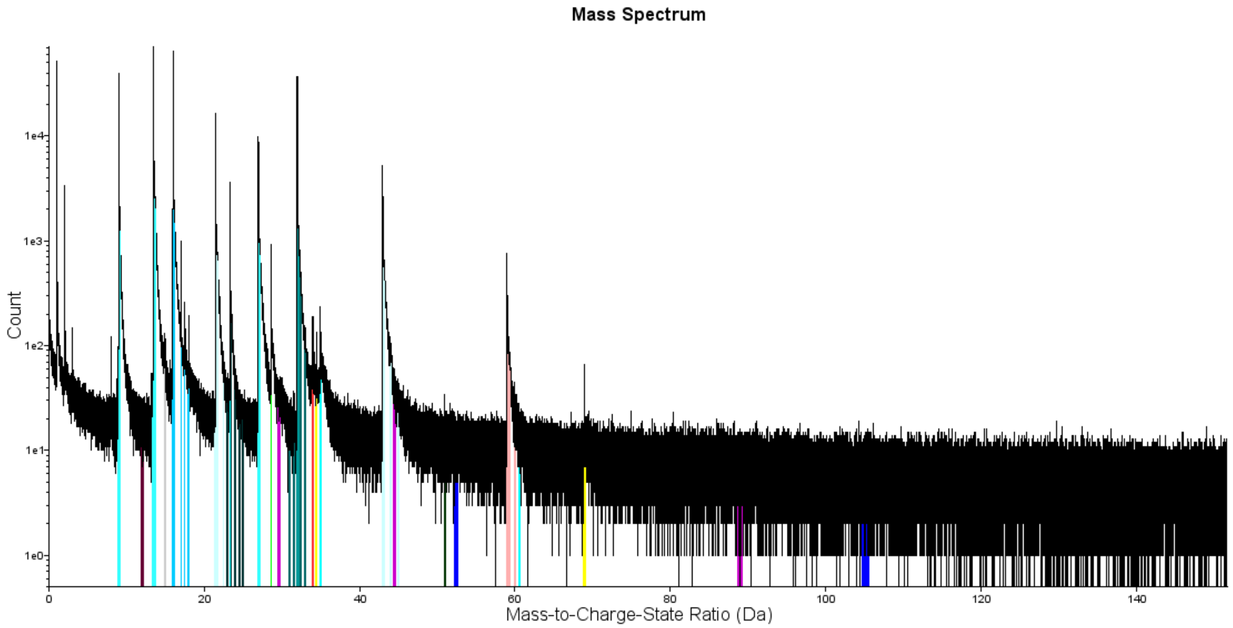

Figure IV. 1: Entire range of the APT spectra obtained from a θ-Al_2O_3 sample, after oxidation of NiAlTiY for 30 minutes of oxidation at 950 °C.

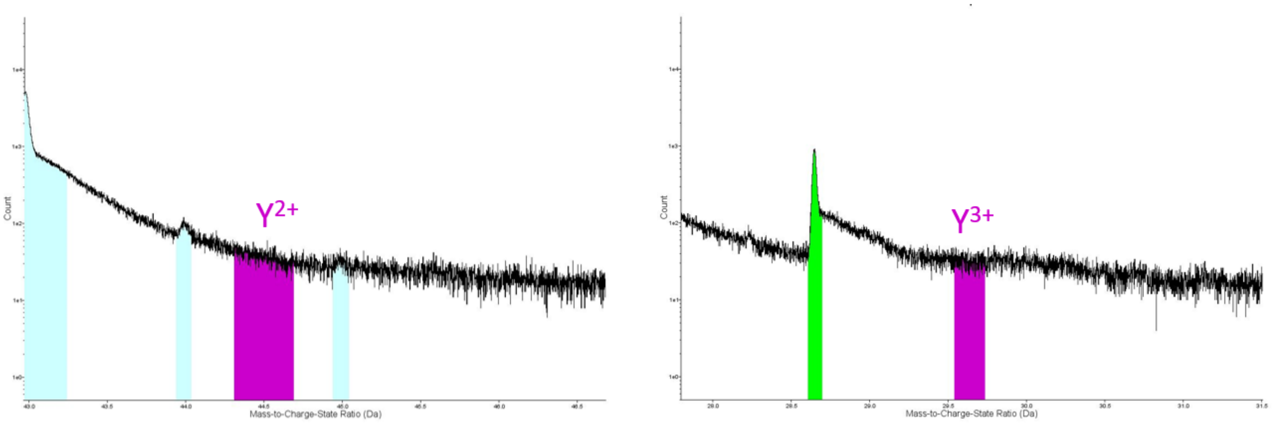

Figure IV. 2: A portion APT spectra obtained from a θ-Al_2O_3 sample after oxidation of NiAlTiY for 30 minutes of oxidation at 950 °C. No Y^{2+} or Y^{3+} peaks were observed.

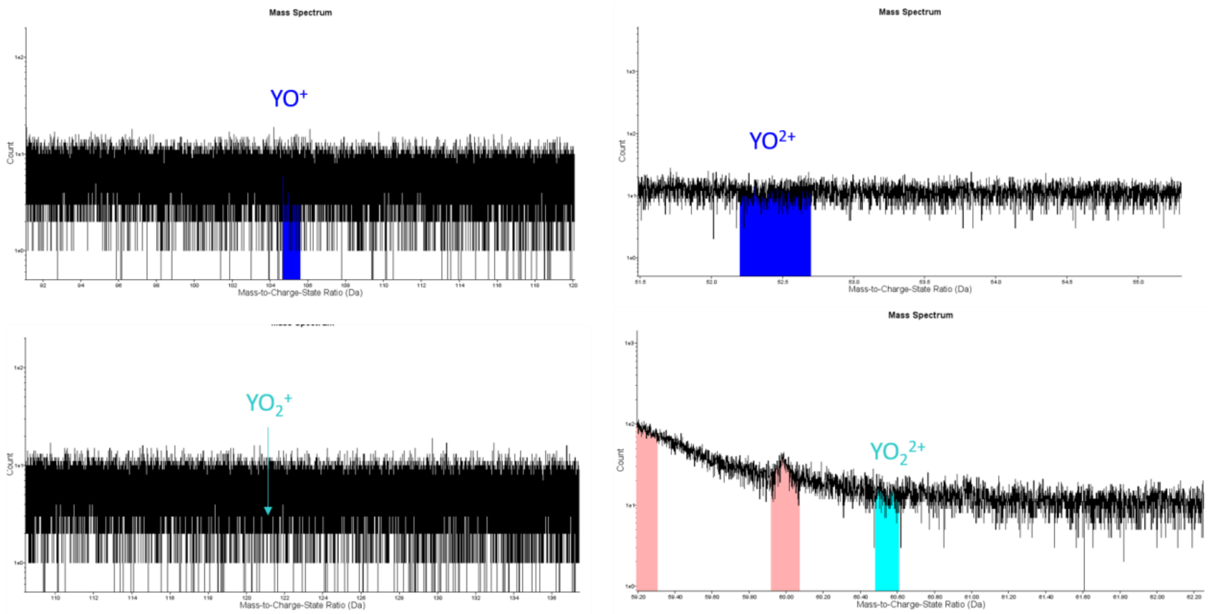

Figure IV. 3: A portion APT spectra obtained from a θ-Al_2O_3 sample after oxidation of NiAlTiY for 30 minutes of oxidation at 950 °C. No peaks were observed for YO or YO_2.

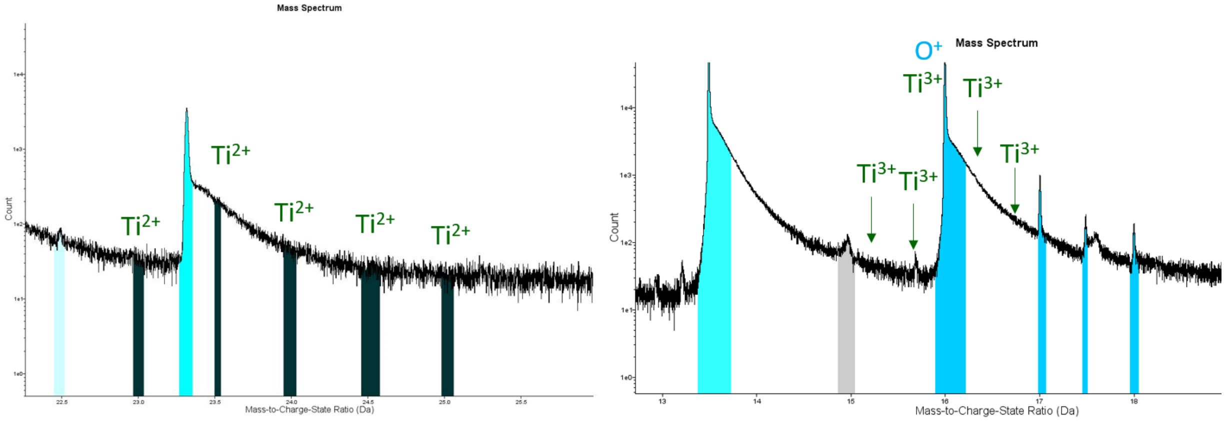

Figure IV. 4: A portion APT spectra obtained from a θ-Al_2O_3 sample after oxidation of NiAlTiY for 30 minutes of oxidation at 950 °C. No Ti^{2+} or Ti^{3+} peaks were observed.

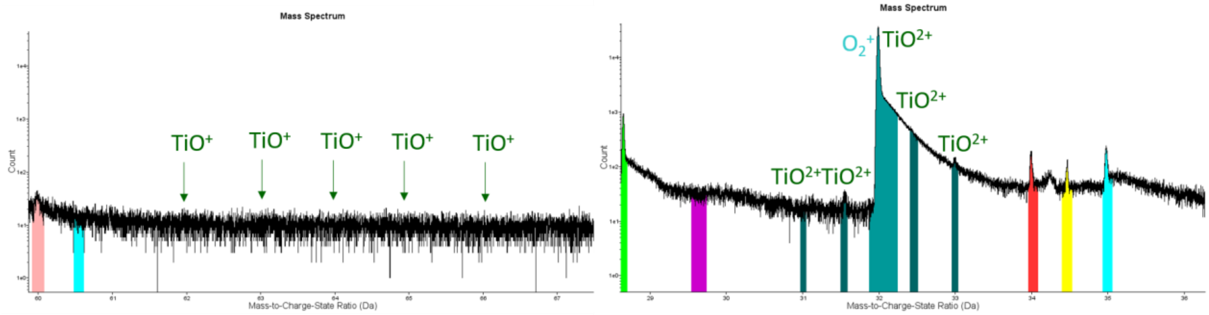

Figure IV. 5: A portion APT spectra obtained from a θ-Al_2O_3 sample after oxidation of NiAlTiY for 30 minutes of oxidation at 950 °C. No peaks were observed for TiO or TiO_2.

REFERENCES

1. Pollock, T.M. and Tin, S., *Nickel-Based Superalloys for Advanced Turbine Engines: Chemistry, Microstructure, and Properties.* Journal of Propulsion and Power, 2006. **22**(2): p. 361-374.
2. Rhys-Jones, T.N., *Protective oxide scales on superalloys and coatings used in gas turbine blade and vane applications.* Materials Science and Technology, 1988. **4**(5): p. 421-430.
3. Giggins, C.S. and Pettit, F.S., *Oxidation of Ni-Cr-Al Alloys Between 1000 and 1200C.* Journal of the Electrochemical Society: Solid State Science, 1971. **118**(11): p. 1782-1790.
4. Birks, N., Meier, G.H., and Pettit, F.S., *Introduction to the High-Temperature Oxidation of Metals*. 2006: Cambridge University Press.
5. Whittle, D.P., *Spalling of Protective Oxide Scales.* Oxidation of Metals, 1972 **4**(3): p. 171-179.
6. Whittle, D.P. and Stringer, J., *Improvement in high temperature oxidation resistance by additions of reactive elements or oxide dispersions.* Philosophical Transactions of the Royal Society of London, Series A, 1980. **295**: p. 309-329.
7. Pint, B.A., *Progress in Understanding the Reactive Element Effect Since the Whittle and Stringer LIterature Review.* Proceedings of the John Stringer Symposium on High Temperature Corrosion, 2001. **5-8**(Nov. 2001): p. 9-19.
8. Hou, P.Y., *Impurity Effects on Alumina Scale Growth.* Journal of the American Ceramic Society, 2003. **86**(4): p. 660-668.
9. Naumenko, D., Pint, B.A., and Quadakkers, W.J., *Current Thoughts on Reactive Element Effects in Alumina-Forming Systems: In Memory of John Stringer.* Oxidation of Metals, 2016. **86**: p. 1-43.
10. Gaskell, D.R. and Laughlin, D.E., *Introduction to the Thermodynamics of Materials*. 6 ed. 2018: CRC Press, Tayor & Francis Group
11. Ellingham, H.J.T., *Reducibility of oxides and sulfides in metallurgical processes.* Journal of the Society of Chemical Industry, 1944.
12. Gaskell, D.R. and Laughlin, D.E., *Introduction to the Thermodynamics of Materials*. 6 ed. 2017, Boca Raton: CRC Press.
13. Opila, E.J., *Volatility of Common Protective Oxides in High-Temperature Water Vapor: Current Understanding and Unanswered Questions.* Materials Science Forum, 2004. **461-464**: p. 765-774.
14. Wallwork, G.R. and Hed, A.Z., *Some Limiting Factors in the Use of Alloys at High Temperatures.* Oxidation of Metals, 1971. **3**(2): p. 171-184.
15. Mehan, R.L. and McKee, D.W., *Interaction of metals and alloys with silicon-based ceramics.* Journal of Materials Science, 1976. **11**: p. 1009-1018.
16. Berthod, P., *Kinetics of High Temperature Oxidation and Chromia Volatilization for a Binary Ni-Cr Alloy.* Oxidation of Metals, 2005. **64**(3/4): p. 235-252.

17. Sachitanand, R., Svensson, J.-E., and Froitzheim, J., *The Influence of Cr Evaporation on Long Term Cr Depletion Rates in Ferritic Stainless Steels.* Oxidation of Metals, 2015. **84**: p. 241-257.
18. Young, D.J., *High Temperature Oxidation and Corrosion of Metals*. Second Edition ed. 2016: Elsevier.
19. Pettit, F.S. and J. B. Wagner, J., *Transition from the Linear to the Parabolic Rate Law During the Oxidation of Iron to Wustite in CO-CO2 Mixtures.* Acta Metallurgica, 1964. **12**: p. 35-40.
20. Quadakkers, W.J., et al., *Growth Rates of Alumina Scales on Fe-Cr-Al Alloys.* Oxidation of Metals, 2004. **61**(1/2): p. 17-37.
21. Pieraggi, B., *Calculations of Parabolic Reaction Rate Constants.* Oxidation of Metals, 1987. **27**(3/4): p. 177-185.
22. Evans, H.E. and Lobb, R.C., *Conditions for the Initiation of Oxide-Scale Cracking and Spallation.* Corrosion Science, 1984. **24**(3): p. 209-222.
23. Hindam, H. and Whittle, D.P., *Microstructure, Adhesion and Growth Kinetics of Protective Scales on Metals and Alloys.* Oxidation of Metals, 1982. **18**(5/6): p. 245-284.
24. Nijdam, T.J., Pers, N.M.v.d., and Sloof, W.G., *Oxide phase development upon high temperature oxidation of gamma-NiCrAl alloys.* Materials and Corrosion, 2006. **57**(3): p. 269-275.
25. Schumann, E., et al., *TEM Investigations on the Oxidation of NiAl.* Oxidation of Intermetallics, 1998: p. 121-134.
26. Grabke, H.J., *Oxidation of NiAl and FeAl.* Intermetallics, 1999. **7**: p. 1153-1158.
27. Brumm, M.W. and Grabke, H.J., *The Oxidation Behaviour of NiAl-- I. Phase Transformations in the Alumina Scale During Oxidation of NiAl and NiAl-Cr Alloys.* Corrosion Science, 1992. **33**(11): p. 1677-1690.
28. Tolpygo, V.K. and Clarke, D.R., *Microstructural study of the theta-alpha transformation in alumina scales formed on nickel-aluminides.* Materials at High Temperatures, 2000. **17**(1): p. 59-70.
29. Lipkin, D.M., et al., *Lateral growth kinetics of a-alumina accompanying the formation of a protective scale on (111) NiAl during oxidation at 1100C.* Appl. Phys. Lett., 1997. **70**(19): p. 2550-2552.
30. Rybicki, G.C. and Smialek, J.L., *Effect of the theta-alpha-Al2O3 Transformation on the Oxidation Behavior of beta-NiAl+Zr.* Oxidation of Metals, 1989. **31**(3/4): p. 275-304.
31. Levin, I. and Brandon, D., *Metastable Alumina Polymorphs: Crystal Structures and Transition Sequences.* Journal of the American Ceramic Society, 1998. **81**(8): p. 1995-2012.
32. John, C.S., Alma, N.C.M., and Hays, G.R., *Characterization of Transitional Alumina by Solid-State Magic Angle Spinning Aluminum NMR.* Applied Catalysis, 1983. **6**: p. 341-346.
33. Wefers, K. and Misra, C., *Oxides and Hydroxides of Aluminum.* Alcoa Technical Paper, 1987(19).
34. Lippens, B.C. and Boer, J.H.D., *Study of Phase Transformations During Calcination of Aluminum Hydroxides by Selected Area Electron Diffraction.* Acta Crystallography, 1964. **17**: p. 1312-1321.
35. Paglia, G., et al., *Boehmite Derived gamma-Alumina System. 1. Structural Evolution with Temperature, with the Identification and Structural Determination of a New Transition Phase, gamma'-Alumina.* Chemistry of Materials, 2004. **16**: p. 220-236.

36. Zhou, R.-S. and Snyder, R.L., *Structures and Transformation Mechanisms of the eta, gamma and theta Transition Aluminas.* Acta Crystallography, 1991. **B47**: p. 617-630.
37. Smrcok, L., Langer, V., and Krestan, J., *gamma-Alumina: a single-crystal X-ray diffraction study.* Acta Crystallographica, 2006. **C62**(83-84).
38. Kronberg, M.L., *Plastic Deformation of Single Crystals of Sapphire: Basal Slip and Twinning.* Acta Metallurgica, 1957. **5**: p. 507-524.
39. Levin, I., et al., *Cubic to Monoclinic Phase Transformations in Alumina.* Acta Materialia, 1997. **45**(9): p. 3659-3669.
40. Jayaram, V. and Levi, C.G., *The Structure of d-Alumina Evolved from the Melt and the g-d Transformation.* Acta Metallurgica, 1989. **37**(2): p. 569-578.
41. Loong, C.K., Jr., J.W.R., and Ozawa, M., *Structural phase transformations of rare-earth modified transition alumina to corundum.* Journal of Alloys and Compounds, 1997. **250**: p. 356-359.
42. Levin, I., Gemming, T., and Brandon, D.G., *Some Metastable Polymorphs and Transient Stages of Transformation in Alumina.* Physica Status Solidi, 1998. **166**: p. 197-218.
43. Kachi, S., Momiyama, K., and Shimizu, S., *An Electron Diffraction Study and a Theory of the Transformation from gamma-Fe2O3 to alpha-Fe2O3.* Journal of the Physical Society of Japan, 1963. **18**(1): p. 106-116.
44. Wynnyckyj, J.R. and Morris, C.G., *A Shear-Type Allotropic Transformation in Alumina.* Metallurgical Transactions B, 1985. **16B**(345-353).
45. Pach, L., Roy, R., and Komarneni, S., *Nucleation of alpha alumina in boehmite gel.* Journal of Materials Research, 1989. **5**(2): p. 278-285.
46. Badkar, P.A. and Bailey, J.E., *The mechanism of simultaneous sintering and phase transformation in alumina.* Journal of Materials Science, 1976. **11**: p. 1794-1806.
47. Burtin, P., et al., *Influence of Surface Area and Additives on the Thermal Stability of Transition Alumina Catalyst Supports. II: Kinetic Model and Interpretation.* Applied Catalysis, 1987. **34**: p. 239-254.
48. Bagwell, R.B., Messing, G.L., and Howell, P.R., *The formation of alpha-Al2O3 from theta-Al2O3: The relevance of a "critical size" and: Diffusional nucleation or "synchro-shear"?* Journal of Materials Science, 2001. **36**: p. 1833-1841.
49. Kao, H.-C. and Wei, W.-C., *Kinetics and Microstructural Evolution of Heterogeneous Transformation of theta-Alumina to alpha-Alumina.* Journal of the American Ceramic Society, 2000. **83**(2): p. 362-368.
50. Yen, F.S., et al., *theta- to alpha- phase transformation subsystem induced by alpha-Al2O3-seeding in boehmite-derived nano-sized alumina powders.* Journal of Crystal Growth, 2003. **249**: p. 283-293.
51. Pint, B.A., Martin, J.R., and Hobbs, L.W., *The oxidation mechanism of theta-Al2O3 scales.* Solid State Ionics, 1995. **78**: p. 99-107.
52. Rommerskirchen, I. and Kolarik, V., *Oxidation of B-NiAl, undoped and doped with Ce, Y, Hf.* Materials and Corrosion, 1996. **47**: p. 625-630.
53. Hindam, H.M. and Smeltzer, W.W., *Growth and Microstructure of alpha-Al2O3 on beta-NiAl.* Journal of the Electrochemical Society: Solid State Science, 1980. **127**(7): p. 1630-1635.
54. Doychak, J., Smialek, J.L., and Mitchell, T.E., *Transient Oxidation of Single-Crystal B-NiAl.* Metallurgical Transactions A, 1989. **20A**: p. 499-518.
55. Yang, J.C., et al., *Transient Oxidation of NiAl.* Acta Materialia, 1998. **46**(6): p. 2195-2201.

56. Prescott, R., et al., *Oxidation Mechanisms of B-NiAl+Zr Determined by SIMS.* Corrosion Science, 1995. **37**(9): p. 1341-1364.
57. Young, E.W.A. and Wit, J.H.W.D., *The Use of a 18O Tracer and Rutherford Backscattering Spectrometry to Study the Oxidation Mechanism of NiAl.* Solid State Ionics, 1985. **16**: p. 39-46.
58. Doychak, J.K. and Mitchell, T.E. *High Temperature Oxidation of beta-NiAl*. in *Materials Research Society Symposium*. 1985.
59. Doychak, J.K., *The Evolution and Growth of Al2O3 Scales on beta-NiAl*, in *Department of Metallurgy and Materials Science*. 1986, Case Western Reserve University: Cleveland, OH. p. 242.
60. Doychak, J. and Ruhle, M., *TEM Studies of Oxidized NiAl and Ni3Al Cross Sections.* Oxidation of Metals, 1989. **31**(5/6): p. 431-452.
61. Hou, P.Y., Paulikas, A.P., and Veal, B.W., *Stress development and relaxation in Al2O3 during early stage oxidation of B-NiAl.* Materials at High Temperatures, 2005. **22**(3/4): p. 535-543.
62. Choi, H.J., et al., *Transmission electron microscopy observations on the phase composition and microstructure of the oxidation scale grown on as-polished and yttrium-implanted B-NiAl.* Surface and Coatings Technology, 2010. **205**: p. 1206-1210.
63. Evans, A.G., Clarke, D.R., and Levi, C.G., *The influence of oxides on the performance of advanced gas turbines.* Journal of the European Ceramic Society, 2008. **28**: p. 1405-1419.
64. Pint, B.A., More, K.L., and Wright, I.G., *Effect of Quaternary Additions on the Oxidation Behavior of Hf-Doped NiAl.* Oxidation of Metals, 2003. **59**(3/4): p. 257-283.
65. Poquillon, D., et al., *High-temperature oxidation kinetics of NiAl single crystal and oxide spallation as a function of crystallographic orientation.* Materials Science and Engineering A, 2004. **281**: p. 237-248.
66. Roux, J.P., Brumm, M.W., and Grabke, H.J., *Effects of orientation and doping with platinum on the oxidation of B-NiAl.* Fresenius Journal of Analytical Chemistry, 1992. **346**: p. 265-268.
67. Uran, S., et al., *Optical Investigation of the Effects of Substrate Orientation on Oxidation of Single Crystal B-NiAl.* Oxidation of Metals, 2001. **56**(5/6): p. 551-569.
68. Burtin, P., et al., *Influence of Surface Area and Additives on the Thermal Stability of Transition Alumina Catalyst Supports. I: Kinetic Data.* Applied Catalysis, 1987. **34**: p. 225-238.
69. Tsuchida, T., et al., *The Effect of Cr3+ and Fe3+ Ions on the Transformation of Different Aluminum Hydroxides to a-Al2O3.* Thermochimic Acta, 1983. **64**: p. 337-353.
70. Bye, G.C. and Simpkin, G.T., *Influence of Cr and Fe on Formation of a-Al2O3 from gamma-Al2O3.* Journal of the American Ceramic Society, 1974. **57**(8): p. 367-371.
71. Pint, B.A., Treska, M., and Hobbs, L.W., *The Effect of Various Oxide Dispersions on the Phase Composition and Morphology of Al_2O_3 Scales Grown on B-NiAl.* Oxidation of Metals, 1997. **47**(1/2): p. 1-20.
72. Renusch, D., et al., *Strain Determination in Thermally-Grown Alumina Scales Using Fluorescence Spectroscopy.* Oxidation of Metals, 1997. **48**(5/6): p. 471-495.
73. Klumpes, R., et al., *The influence of chromium on the oxidation of B-NiAl at 1000C.* Materials and Corrosion, 1996. **47**: p. 619-624.

74. Golightly, F.A., Stott, F.H., and Wood, G.C., *The Influence of Yttrium Additions on the Oxide-Scale Adhesion to an Iron-Chromium-Aluminum Alloy.* Oxidation of Metals, 1976. **10**(3): p. 163-187.
75. Jedlinski, J. and Borchardt, G., *On the Oxidation Mechanism of Alumina Formers.* Oxidation of Metals 1991. **36**(3/4): p. 317-337.
76. Jedlinski, J., *Comments on the Effect of Yttrium on the Early Stages of Oxidation of Alumina Formers.* Oxidation of Metals, 1993. **39**(1/2): p. 55-60.
77. Smialek, J., *Oxide Morphology and Spalling Model for NiAl.* Metallurgical Transactions A, 1978. **9A**: p. 309-320.
78. Hu, L., Hovis, D.B., and Heuer, A.H., *Transient Oxidation of a gamma-Ni-28Cr-11Al Alloy.* Oxidation of Metals, 2010. **73**: p. 275-288.
79. Josefsson, H., et al., *Oxidation of FeCrAl alloys at 500-900C in dry O2.* Materials and Corrosion, 2005. **56**(11): p. 801-805.
80. Tolpygo, V.K. and Clarke, D.R., *Microstructural evidence for counter-diffusion of aluminum and oxygen during the growth of alumina scales.* Materials at High Temperatures, 2003. **20**(3): p. 261-271.
81. Brumm, M.W. and Grabke, H.J., *Oxidation Behavior of NiAl-- II. Cavity Formation Beneath the Oxide Scale on NiAl of Different Stoichiometries.* Corrosion Science, 1993. **34**(4): p. 547-561.
82. Yang, S., Wang, F., and Wu, W., *Effect of microcrystallization on the cyclic oxidation behavior of B-NiAl intermetallics at 1000C in air.* Intermetallics, 2001. **9**: p. 741-744.
83. Oquab, D. and Monceau, D., *In-Situ SEM Study of Cavity Growth During High Temperature Oxidation of B-(Ni,Pd)Al.* Scripta Materialia, 2001. **44**: p. 2741-2746.
84. Hu, L., Hovis, D., and Heuer, A., *The effect of substrate orientation on oxidation-induced void formation in B-Ni-40Al-5Cr-0.03Y.* Scripta Materialia, 2009. **61**: p. 157-160.
85. Svensson, H., Knutsson, P., and Stiller, K., *Formation and Healing of Voids at the Metal-Oxide Interface in NiAl Alloys.* Oxidation of Metals, 2009. **71**: p. 143-156.
86. Gesmundo, F. and Hou, P.Y., *Analysis of Pore Formation at Oxide-Alloy Interfaces-- II. Theoretical Treatment of Vacancy Condensation for Immobile Interfaces.* Oxidation of Metals, 2003. **59**(1/2): p. 63-81.
87. Pint, B.A., *On the Formation of Interfacial and Internal Voids in a-Al2O3 Scales.* Oxidation of Metals, 1997. **48**(3/4): p. 303-328.
88. Gleeson, B., et al., *Effects of Platinum on the Interdiffusion and Oxidation Behavior of Ni-Al-Based Alloys.* Materials Science Forum, 2004. **461-464**: p. 213-222.
89. Cadoret, Y., et al., *Effect of Pt Additions on the Sulfur Segregation, Void Formation and Oxide Scale Growth of Cast Nickel Aluminides.* Materials Science Forum, 2004. **461-464**: p. 247-254.
90. Svensson, H., et al., *Influence of Pt on the metal-oxide interface during high temperature oxidation of NiAl bulk materials.* Corrosion Science, 2009. **51**: p. 539-546.
91. Grabke, H.J., Wiemer, D., and Viefhaus, H., *Segregation of sulfur during growth of oxide scales.* Applied Surface Science, 1991. **47**: p. 243-250.
92. Smialek, J., *Effect of Sulfur Removal on Al2O3 Scale Adhesion.* Metallurgical Transactions A, 1991. **22A**(739-752).
93. Hou, P.Y. and Priimak, K., *Interfacial Segregation, Pore Formation, and Scale Adhesion on NiAl Alloys.* Oxidation of Metals, 2005. **63**(1/2): p. 113-130.

94. Rivoaland, L., et al., *The Effect of Sulfur Segregation on the Adherence of the Thermally-Grown Oxide on NiAl-- II. The Oxidation Behavior at 900C of Standard, Desulfurized or Sulfur-Doped NiAl(001) Single-Crystals.* Oxidation of Metals, 2003. **60**(1/2): p. 159-178.
95. Lees, D.G., *On the reasons for the effects of dispersions of stable oxides and additions of reactive elements to the adhesion and growth-mechanisms of chromia and alumina scales-the "sulfur effect".* Oxidation of Metals, 1987. **27**: p. 75-81.
96. Golightly, F.A., Stott, F.H., and Wood, G.C., *The Relationship Between Oxide Grain Morphology and Growth Mechanisms for Fe-Cr-Al and Fe-Cr-Al-Y Alloys.* Journal of the Electrochemical Society, 1979. **126**(6): p. 1035-1042.
97. Pint, B.A. and Alexander, K.B., *Grain Boundary Segregation of Cation Dopants in a-Al2O3 Scales.* Journal of the Electrochemical Society, 1998. **145**(6): p. 1819-1829.
98. Mennicke, C., et al., *The Effect of Yttrium on the Growth Process and Microstructure of a-Al2O3 on FeCrAl.* Oxidation of Metals, 1998. **49**(5/6): p. 455-466.
99. Nychka, J.A. and Clarke, D.R., *Quantification of Aluminum Outward Diffusion During Oxidation of FeCrAl Alloys.* Oxidation of Metals, 2005. **63**(5/6): p. 325-352.
100. Naumenko, D., et al., *Correlation between the Microstructure, Growth Mechanism, and Growth Kinetics of Alumina Scales on a FeCrAlY Alloy.* Mechanical and Materials Transactions A, 2007. **38A**: p. 2974-2983.
101. Al-Badairy, H., Prior, D.J., and Tatlock, G.J., *FEG-SEM examination of alumina scales formed on FeCrAl alloys.* Materials at High Temperatures, 2014. **22**(3-4): p. 453-460.
102. Pint, B.A., *The Oxidation Behavior of Oxide-Dispersed B-NiAl: I. Short-Term Performance at 1200C.* Oxidation of Metals, 1997. **49**(5/6): p. 531-559.
103. Li, D., et al., *Cyclic oxidation of B-NiAl with various reactive element dopants at 1200C.* Corrosion Science, 2013. **66**: p. 125-135.
104. Guo, H., et al., *Effect of co-doping of two reactive elements on alumina scale growth of B-NiAl at 1200C.* Corrosion Science, 2014. **88**: p. 197-208.
105. Blachere, J.R., et al., *Textures of alumina scales on FeCrAl alloys.* Scripta Materialia, 2003. **49**: p. 909-912.
106. White, R. and Weaver, M., *Microstructural Investigation of the Thermally Grown Oxide on Grain-Refined Overdoped NiAl-Zr.* Oxidation of Metals, 2019. **92**: p. 227-242.
107. Karadge, M., et al., *Microtexture of the thermally grown alumina in commercial thermal barrier coatings.* Scripta Materialia, 2006. **54**: p. 639-644.
108. Smialek, J.L., et al., *Oxygen Permeability and Grain-Boundary Diffusion Applied to Alumina Scales.* NASA Technical Memorandum, 2013.
109. Geers, C. and Panas, I., *Impact of Grain Boundary Density on Oxide Scaling Revisited.* Oxidation of Metals, 2018. **91**(1-2): p. 55-75.
110. Mocellin, A. and Kingery, W.D., *Microstructural Changes During Heat Treatment of Sintered Al2O3.* Journal of the American Ceramic Society, 1973. **56**(6): p. 309-314.
111. Shaw, N.J. and Brook, R.J., *Structure and Grain Coarsening During the Sintering of Alumina.* Journal of the American Ceramic Society, 1986. **69**(2): p. 107-110.
112. Smothers, W.J. and Reynolds, H.J., *Sintering and Grain Growth of Alumina.* Journal of the American Ceramic Society, 1954. **37**(12): p. 588-595.
113. Choquet, P. and Mevrel, R., *Microstructure of Alumina Scales Formed on NiCoCrAl Alloys with and without Yttrium.* Materials Science and Engineering, 1989. **A120**: p. 153-159.
114. Quadakkers, W.J., *Growth mechanisms of oxide scales on ODS alloys in the temperature range 1000-1100C.* Werkstoffe und Korrosion, 1990. **41**: p. 659-668.

115. Young, D.J., et al., *Oxidation kinetics of Y-doped FeCrAl-alloys in low and high pO2 gases.* Materials and Corrosion, 2010. **61**(10): p. 838-844.
116. Stringer, J., *The Reactive Element Effect in High-Temperature Corrosion.* Materials Science and Engineering, 1989. **A120**: p. 129-137.
117. Reddy, K.P.R., Smialek, J.L., and Cooper, A.R., *18O Tracer Studies of Al2O3 Scale Formation on NiCrAl Alloys.* Oxidation of Metals, 1982. **17**(5/6): p. 429-449.
118. Pint, B.A., Martin, J.R., and Hobbs, L.W., *18O/SIMS Characterization of the Growth Mechanism of Doped and Undoped a-Al2O3.* Oxidation of Metals, 1993. **39**(3/4): p. 167-195.
119. Young, E.W.A. and Wit, J.H.W.d., *An 18O Tracer Study on the Growth Mechanism of Alumina Scales on NiAl and NiAlY Alloys.* Oxidation of Metals, 1986. **26**(5/6): p. 351-361.
120. Quadakkers, W.J., *Composition and growth mechanisms of alumina scales on FeCrAl-based alloys determined by SIMS.* Applied Surface Science, 1991. **52**: p. 271-287.
121. Clemens, D., et al., *Analysis and modelling of transport processes in alumina scales on high temperature alloys.* Fresenius Journal of Analytical Chemistry, 1993. **346**: p. 318-322.
122. Prescott, R., Mitchell, D.F., and Graham, M.J., *A Study of the Growth of a-Al2O3 Scales Using High-Resolution Imaging Secondary Mass Spectrometry.* Corrosion Science, 1994. **50**(1): p. 62-71.
123. Schumann, E., et al., *High-Resolution SIMS and Analytical TEM Evaluation of Alumina Scales on B-NiAl Containing Zr or Y.* Oxidation of Metals, 1996. **46**(1/2): p. 37-49.
124. Jedlinski, J., et al., *On the application of SIMS to study the oxidation mechanisms of alumina formers.* Materials at High Temperatures, 2005. **22**(3-4): p. 505-519.
125. Ooi, T.N., et al., *Isotope exchange studies of oxidation mechanisms in nickel-base superalloys using FIB-SIMS techniques.* Surface and Coatings Technology, 2006. **201**: p. 3885-3888.
126. Ramanarayanan, T.A., Raghavan, M., and Petkovic-Lutan, R., *The Characteristics of Alumina Scales Formed on Fe-Based Yttria-Dispersed Alloys.* Journal of the Electrochemical Society, 1984. **131**(4): p. 923-931.
127. Cotell, C.M., et al., *The Influence of Grain-Boundary Segregation of Y in Cr2O3 on the Oxidation of Cr Metal.* Oxidation of Metals, 1990. **34**(3/4): p. 173-200.
128. Pint, B.A., *Experimental Observations in Support of the Dynamic-Segregation Theory to Explain the Reactive-Element Effect.* Oxidation of Metals, 1996. **45**(1/2): p. 1-37.
129. Pint, B.A., More, K.L., and Wright, I.G., *The use of two reactive elements to optimize oxidation performance of alumina-forming alloys.* Materials at High Temperatures, 2003. **20**(3): p. 375-386.
130. Prot, D., et al., *Self-diffusion in a-Al2O3. IV. Oxygen grain-boundary self-diffusion in undoped and yttria-doped alumina polycrystals.* Philosophical Magazine A, 1996. **73**(4): p. 935-949.
131. Nakagawa, T., et al., *Yttrium doping effect on oxygen grain boundary diffusion in a-Al2O3.* Acta Materialia, 2007. **55**: p. 6627-6633.
132. Gall, M.L., et al., *Self-diffusion in a-Al2O3 and growth rate of alumina scales formed by oxidation: effect of Y2O3 doping.* Journal of Materials Science, 1995. **30**: p. 201-211.
133. Nakagawa, T., et al., *Grain boundary character dependence of oxygen grain boundary diffusion in a-Al2O3 bicrystals.* Scripta Materialia, 2011. **65**: p. 544-547.
134. Heuer, A.H., et al., *The Band Structure of Polycrystalline Al2O3 and Its Influence on Transport Phenomena.* Journal of the American Ceramic Society, 2016. **99**(3): p. 733-747.

135. Sakaguchi, I., et al., *Grain Boundary Diffusion of Oxygen in Alumina Ceramics.* Journal of the American Ceramic Society, 1995. **78**(9): p. 2557-2559.
136. Buban, J.P., et al., *Grain Boundary Strengthening in Alumina by Rare Earth Impurities.* Science, 2006. **311**(5758): p. 212-215.
137. Shang, S.-L., et al., *Understanding slow-growing alumina scale mediated by reactive elements: Perspective via local metal-oxygen bonding strength.* Scripta Materialia, 2018. **150**: p. 139-142.
138. Yoshida, H., Ikuhara, Y., and Sakuma, T., *High-temperature creep resistance in rare-earth-doped, fine-grained Al2O3.* Journal of Materials Research, 1997. **13**(9): p. 2597-2601.
139. Cho, J., et al., *Role of Segregating Dopants on the Improved Creep Resistance of Aluminum Oxide.* Acta Materialia, 1999. **47**(15): p. 4197-4207.
140. Cannon, R.M. and Coble, R.L., *Review of Diffusional Creep of Al2O3*, in *Deformation of Ceramic Materials*, R.E.T. R. C. Bradt, Editor. 1975, Springer: Boston, MA.
141. Fielitz, P., et al., *Aluminum-26 grain boundary diffusion in pure and Y-doped polycrystalline a-Al2O3.* Acta Materialia, 2017. **127**: p. 302-311.
142. Pint, B.A., Garratt-Reed, A.J., and Hobbs, L.W., *Possible Role of the Oxygen Potential Gradient in Enhancing Diffusion of Foreign Ions on alpha-Al2O3 Grain Boundaries.* Journal of the American Ceramic Society, 1998. **81**(2): p. 305-314.
143. Guo, H., et al., *Effect of Sm, Gd, Yb, Sc, and Nd as reactive elements on oxidation behaviour of B-NiAl at 1200C.* Corrosion Science, 2014. **78**: p. 369-377.
144. Pint, B.A., *Optimization of Reactive-Element Additions to Improve Oxidation Performance of Alumina-Forming Alloys.* Journal of American Ceramic Society, 2003. **86**(4): p. 686-695.
145. Haynes, J.A., et al., *Influence of Sulfur, Platinum, and Hafnium on the Oxidation Behavior of CVD NiAl Bond Coatings.* Oxidation of Metals, 2002. **58**(5/6): p. 513-544.
146. Heuer, A.H., et al., *On the growth of Al2O3 scales.* Acta Materialia, 2013. **61**: p. 6670-6683.
147. Tautschnig, M.P., Harrison, N.M., and Finnis, M.W., *A model for time-dependent grain boundary diffusion of ions and electrons through a film or scale, with an application to alumina.* Acta Materialia, 2017. **132**: p. 503-516.
148. Huang, L., et al., *Oxidation behavior of a single-crystal Ni-base superalloy in air at 900, 1000 and 1100C.* Tribology Letters, 2006. **23**(1): p. 15-22.
149. Gheno, T., et al., *A Thermodynamic Approach to Guid Reactive Element Doping: Hf Additions to NiCrAl.* Oxidation of Metals, 2017. **87**: p. 297-310.
150. Kochubey, V., et al., *Effects of minor additions and impurities on oxidation behaviour of FeCrAl alloys. Development of novel surface coatings compositions.* Materials and Corrosion, 2005. **56**(12): p. 848-853.
151. Quadakkers, W.J., et al., *Batch to batch variations in the oxidation behaviour of alumina forming Fe-based alloys.* Materials and Corrosion, 2000. **51**: p. 350-357.
152. Clemens, D., Quadakkers, W.J., and Singheiser, L., *Effect of Si and Ti Additions on Alumina Scale Formation on NiCrAlY-Alloys.* Electrochemical Society Proceedings 1998. **98-9**: p. 134-145.
153. Wei, L., et al., *Cyclic oxidation behavior of Hf/Zr co-doped EB-PVD B-NiAl coatings at 1200C.* Surface and Coatings Technology, 2015. **276**: p. 721-725.

154. Suo, Z., *Wrinkling of the Oxide Scale on an Aluminum-Containing Ally at High Temperatures.* Journal of the Mechanics and Physics of Solids, 1995. **43**(6): p. 829-846.
155. Tolpygo, V.K. and Clarke, D.R., *Wrinkling of a-Alumina Films Grown by Thermal Oxidation--I. Quantitative Studies on Single Crystals of Fe-Cr-Al Alloy.* Acta Materialia, 1998. **46**(14): p. 5153-5166.
156. Rhines, F.N. and Wolf, J.S., *The Role of Oxide Microstructure and Growth Stresses in the High-Temperature Scaling of Nickel.* Metallurgical Transactions, 1970. **1**: p. 1701-1710.
157. Tolpygo, V.K. and Clarke, D.R., *Competition Between Stress Generation and Relaxation During Oxidation of an Fe-Cr-Al-Y Alloy.* Oxidation of Metals, 1998. **49**(1/2): p. 187-212.
158. Tortorelli, P.F., et al., *Growth stress-microstructure relationships for alumina scales.* Materials at High Temperatures, 2003. **20**(3): p. 303-310.
159. Lipkin, D.M., et al., *Stress Development in Alumina Scales Formed Upon Oxidation of (111) NiAl Single Crystals.* Corrosion Science, 1997. **39**(2): p. 231-242.
160. Schumann, E., et al., *High-Temperature Stress Measurements During the Oxidation of NiAl.* Oxidation of Metals, 2000. **53**(3/4): p. 259-272.
161. Reddy, A., et al., *In Situ Study of Oxidation-Induced Growth Strains In a Model NiCrAlY Bond-Coat Alloy.* Oxidation of Metals, 2007. **67**(3/4): p. 153-177.
162. Evans, A.G. and Cannon, R.M., *Stresses in Oxide Films and Relationships with Cracking and Spalling.* Materials Science Forum, 1989. **43**: p. 243-297.
163. Sarioglu, C., et al., *X-ray determination of stresses in alumina scales on high temperature alloys.* Materials at High Temperatures, 2000. **17**(1): p. 109-115.
164. Christensen, R.J., Tolpygo, V.K., and Clarke, D.R., *The Influence of the Reactive Element Yttrium on the Stress in Alumina Scales Formed by Oxidation.* Acta Materialia, 1997. **45**(4): p. 1761-1766.
165. French, J.D., et al., *Creep of Duplex Microstructures.* Journal of the American Ceramic Society, 1994. **77**(11): p. 2857-2865.
166. Sharma, S.K., Ko, G.D., and Kang, K.J., *High temperature creep and tensile properties of alumina formed on Fecralloy foils doped with yttrium.* Journal of the European Ceramic Society, 2009. **29**: p. 355-362.
167. Veal, B.W. and Paulikas, A.P., *Growth strains and creep in thermally grown alumina: Oxide growth mechanisms.* Journal of Applied Physics, 2008. **104**: p. 1-15.
168. He, J., et al., *The role of Cr and Si in affecting high-temperature oxidation behaviour of minor Dy doped NiAl alloys.* Corrosion Science, 2013. **77**: p. 322-333.
169. Dai, P., et al., *The effect of silicon on the oxidation behavior of NiAlHf coating system.* Applied Surface Science, 2013. **271**: p. 311-316.
170. Clemens, D., et al., *TEM and SNMS studies of protective alumina scales on NiCrAlY-alloys.* Fresenius Journal of Analytical Chemistry, 1996. **355**: p. 703-706.
171. Long, H., et al., *Microstructural and compositional design of Ni-based single crystalline superalloys-- A review.* Journal of Alloys and Compounds, 2018. **743**: p. 203-220.
172. Angerman, C.L., *Long-Term Oxidation of Superalloys.* Oxidation of Metals, 1972. **5**(2): p. 149-167.
173. Ragan, D.D., Mates, T., and Clarke, D.R., *Effect of Ytrium and Erbium Ions on Epitaxial Phase Transformations in Alumina.* Journal of the American Ceramic Society, 2003. **86**(4): p. 541-545.

174. Fei, W., Kuiry, S.C., and Seal, S., *Inhibition of Metastable Alumina Formation on Fe-Cr-Al-Y Alloy Fibers at High Temperature using Titania Coating* Oxidation of Metals, 2004. **62**(1/2): p. 29-44.
175. N'Dah, E., et al., *Metastable alumina formation during oxidation of FeCrAl and its suppression by surface treatments.* Materials and Corrosion, 2005. **56**(12): p. 843-847.
176. Munoz-Arroyo, R., et al., *Influence of Composition and Phase Distribution on the Oxidation Behaviour of NiCoCrAlY Alloys.* Materials Science Forum, 2001. **369-372**: p. 165-172.
177. Zhao, W., Li, Z., and Gleeson, B., *A New Kinetics-Based Approach to Quantifying the Extent of Metastable-Stable Phase Transformation in Thermally-Grown Al2O3 Scales.* Oxidation of Metals, 2013. **79**: p. 361-381.
178. Liang, X. and Wang, X., *Modeling of theta-alpha alumina lateral phase transformation with applications to oxidation kinetics of NiAl-based alloys.* Materials and Design, 2016. **112**: p. 519-529.
179. Jedlinski, J., et al., *Oxide phases and residual stresses in scales formed at early stages of oxidation of B-NiAl at 1473K and the effect of implanted yttrium.* Materials and Corrosion, 2017. **68**(2): p. 235-248.
180. Lipkin, D.M. and Clarke, D.R., *Measurement of the Stress in Oxide Scales Formed by Oxidation of Alumina-Forming Alloys.* Oxidation of Metals, 1996. **45**(3/4): p. 267-280.
181. Wen, Q., Lipkin, D.M., and Clarke, D.R., *Luminescence Characterization of Chromium-Containing theta-Alumina.* Journal of the American Ceramic Society, 1998. **81**(12): p. 3345-3348.
182. Wallin, E., et al., *Effects of additives in alpha and theta-alumina: an ab initio study.* Journal of Physics: Condensed Matter, 2004. **16**: p. 8971-8980.
183. Bolvardi, H., et al., *Effect of Si additions on the thermal stability and the phase transition sequence of sputtered amorphous alumina thin films.* Journal of Applied Physics, 2015. **117**: p. 1-22.
184. Lagerlof, K.P.D. and Grimes, R.W., *The Defect Chemistry of Sapphire (a-Al2O3).* Acta Materialia, 1998. **46**(16): p. 5689-5700.
185. Mohapatra, S.K. and Kroger, F.A., *Defect Structure of a-Al2O3 Doped with Titanium.* Journal of the American Ceramic Society, 1977. **60**(9-10): p. 381-387.
186. Matsunaga, K. and Nakamura, A., *First-principles study of defect energetics in titanium-doped alumina.* Physical Review B, 2003. **68**: p. 1-8.
187. Andersson, J.M., et al., *Microstructure of a-alumina thin films deposited at low temperatures on chromia template layers.* Journal of Vacuum Science and Technology, 2004. **22**(1): p. 117-121.
188. Shankar, S. and Seigle, L.L., *Interdiffusion and Intrinsic Diffusion in the NiAl Phase of the Al-Ni System.* Metallurgical Transactions A, 1978. **9A**: p. 1467-1476.
189. Xu, B., et al., *Structures, preparation and applications of titanium suboxides.* RSC Advances, 2016. **6**: p. 79706-79722.
190. Rahimi, N., Pax, R.A., and Gray, E.M., *Review of functional titanium oxides.* Progress in Solid State Chemistry, 2016. **44**: p. 86-105.
191. Quadakkers, W.J., et al., *Differences in Growth Mechanisms of Oxide Scales Formed on ODS and Conventional Wrought Alloys.* Oxidation of Metals, 1989. **32**(1/2): p. 67-88.

192. Haynes, J.A., et al., *Influences of Superalloy Composition and Pt Content on the Oxidation Behavior of Gamma-Gamma Prime NiPtAl Bond Coatings.* Oxidation of Metals, 2016. **86**: p. 453-481.
193. Tawancy, H.M., Mohamed, A.I., and Abbas, N.M., *Effect of superalloy substrate composition on the performance of a thermal barrier coating system.* Journal of Materials Science, 2003. **38**: p. 3797-3807.
194. Schumann, E., et al., *Segregation studies of oxidized Y and Zr doped NiAl.* Materials and Corrosion, 1995. **46**: p. 218-222.
195. Pint, B.A. and Unocic, K.A., *Ionic segregation on grain boundaries in thermally grown alumina scales.* Materials at High Temperatures, 2012. **29**(3): p. 257-263.
196. Przybylski, K., et al., *Segregation of Y to Grain Boundaries in the Al2O3 Scale Formed on an ODS Alloy.* J. Electrochem. Soc., 1987: p. 3207-3208.
197. Tawancy, H.M. and Sridhar, N., *High-Temperature Oxidation Behavior of a Ni-Cr-Al-Fe-Y Alloy.* Oxidation of Metals, 1992. **37**(3/4): p. 143-166.
198. Dickey, E.C., et al., *Oxidation behavior of platinum-aluminum alloys and the effect of Zr doping.* Journal of Materials Research, 1999. **14**(12): p. 4531-4540.
199. Hiramatsu, N. and Stott, F.H., *The Effect of Lanthanum on the Scales Developed on Thin Foils of Fe-20Cr-5Al at Very High Temperatures.* Oxidation of Metals, 1999. **51**(5/6): p. 479-494.
200. Voytovych, R., et al., *The effect of yttrium on densification and grain growth in a-alumina.* Acta Materialia, 2002. **50**: p. 3453-3463.
201. Cueff, R., et al., *Influence of Yttrium-Alloying Addition on the Oxidation of Alumina Formers at 1173K.* Oxidation of Metals, 2002. **58**(5/6): p. 439-455.
202. Kvernes, I.A., *The Role of Yttrium in High-Temperature Oxidation Behavior of Ni-Cr-Al Alloys.* Oxidation of Metals, 1973. **6**(1): p. 45-64.
203. Santoro, G.J., Deadmore, D.L., and Lowell, C.E., *Oxidation of Alloys in Nickel-Aluminum System with Third-Element Additions of Chromium, Silicon, and Titanium at 1100C.* NASA Technical Note, 1971. **D-6414**: p. 1-28.
204. Lowell, C.E. and Santoro, G.J., *The 1200C Cyclic Oxidation Behavior of Two Nickel-Aluminum Alloys (Ni3Al and NiAl) with Additions of Chromium, Silicon, and Titanium.* Nasa Technical Note, 1972(D-6838): p. 1-17.
205. Lagrange, M.H., Huntz, A.M., and Davidson, J.H., *The Influence of Y, Zr or Ti Additions on the High Temperature Oxidation Resistance of Fe-Ni-Cr-Al Alloys of Variable Purity.* Corrosion Science, 1984. **24**(7): p. 613-627.
206. Naumenko, D., et al., *Modification of alumina scale formation on FeCrAlY alloys by minor additions of group IVa elements.* Journal of Materials Science, 2008. **43**: p. 4550-4560.
207. Boll, T., et al., *Grain Boundary Chemistry and Transport Through Alumina Scales on NiAl Alloys.* Oxidation of Metals, 2017.
208. Lee, W.E. and Lagerlof, K.P.D., *Structural and Electron Diffraction Data for Sapphire (a-Al2O3).* Journal of Electron Microscopy Technique, 1985. **2**: p. 247-258.
209. Pett-Ridge, J. and Weber, P.K., *NanoSIP: NanoSIMS Applications for Microbial Biology*, in *Microbial Systems Biology: Methods and Protocols*, A. Navid, Editor. 2012, Humana Press: Totowa, NJ. p. 375-408.
210. Unocic, K.A., Parish, C.M., and Pint, B.A., *Characterization of the alumina scale formed on coated and uncoated doped superalloys.* Surface and Coatings Technology, 2011. **206**: p. 1522-1528.

211. Huang, T., et al., *Effect of Titanium Addition on Alumina Growth Mechanism on Yttria-Containing FeCrAl-Base Alloy.* Oxidation of Metals, 2018. **90**: p. 671-690.
212. Cheng, H., et al., *The Effect of Yttrium on Oxygen Grain-Boundary Transport in Polycrystalline Alumina Measured Using Ni Marker Particles.* Journal of the American Ceramic Society, 2008. **91**(6): p. 2002-2008.
213. Reddy, K.P.R. and Cooper, A.R., *Oxygen Diffusion in Sapphire.* Journal of the American Ceramic Society, 1982. **65**(12): p. 634-638.
214. Kuenzly, J.D. and Douglass, D.L., *The Oxidation Mechanism of Ni3Al Containing Yttrium.* Oxidation of Metals, 1974. **8**(3): p. 139-178.
215. Cho, J., et al., *Influence of Yttrium Doping on Grain Misorientation in Aluminum Oxide.* Journal of the American Ceramic Society, 1998. **81**(11): p. 3001-3004.
216. Bae, S.I. and Baik, S., *Sintering and grain growth of ultrapure alumina.* Journal of Materials Science, 1993. **28**: p. 4197-4204.
217. Veal, B.W., et al., *Creep in a-Al2O3 thermally grown on B-NiAl and NiAlPt alloys.* Surface and Coatings Technology, 2007. **202**: p. 608-612.
218. Liu, H., Stack, M.M., and Lyon, S.B., *Reactive element effects on the ionic transport processes in Cr2O3 scales.* Solid State Ionics, 1998. **109**: p. 247-257.
219. Stott, F.H., Wood, G.C., and Stringer, J., *The Influence of Alloying Elements on the Development and Maintenance of Protective Scales.* Oxidation of Metals, 1995. **44**(1/2): p. 113-145.
220. Reed, R.C., in *The Superalloys: Fundamentals and Applications*. 2006, Cambridge University Press: Cambridge.
221. Cruchley, S., et al., *Chromia layer growth on a Ni-based superalloy: Sub-parabolic kinetics and the role of titanium.* Corrosion Science, 2015. **75**: p. 58-66.
222. Holt, A. and Kofstad, P., *Electrical conductivity of Cr2O3 doped with TiO2.* Solid State Ionics, 1999. **117**: p. 21-25.
223. Blacklocks, A.N., et al., *An XAS study of the defect structure of Ti-doped a-Cr2O3.* Solid State Ionics, 2006. **177**(2939-2944).
224. Nijdam, T.J., Jeurgens, L.P.H., and Sloof, W.G., *Effect of partial oxygen pressure on the initial stages of high-temperature oxidation of gamma-NiCrAl alloys.* Materials at High Temperatures, 2003. **20**(3): p. 311-318.
225. Nijdam, T.J., Jeurgens, L.P.H., and Sloof, W.G., *Promoting exclusive alpha-Al2O3 growth upon high-temperature oxidation of NiCrAl alloys: experiment versus model predictions.* Acta Materialia, 2005. **53**: p. 1643-1653.
226. Rapp, R.A., *Kinetics, Microstructures and Mechanism of Internal Oxidation- Its Effect and Prevention in High Temperature Alloy Oxidation*, in *21st Conference, National Association of Corrosion Engineers*. 1965: St. Louis, Mo.
227. Yi, H.C., et al., *Internal oxidation of Ni Al and Ni Al Si alloys at the dissociation pressure of NiO.* Acta Metallurgica et Materialia, 1994. **42**(3): p. 981-990.
228. Stott, F.H. and Wood, G.C., *Internal Oxidation.* Materials Science and Technology, 1988. **4**(12): p. 1072-1078.
229. Kale, G.M. and Fray, D.J., *Oxygen Potentials in Ni+NiO and Ni+Cr2O3+NiCr2O4 Systems.* Metallurgical and Materials Transactions B, 1994. **25B**: p. 373-378.
230. Litz, J., Rahmel, A., and Schorr, M., *Selective Carbide Oxidation and Internal Nitridation of the Ni-Base Superalloys IN 738 LC and IN 939 in Air.* Oxidation of Metals, 1988. **30**(1/2): p. 95-105.

231. Chen, J.H., Rogers, P.M., and Little, J.A., *Oxidation Behavior of Several Chromia-Forming Commercial Nickel-Base Superalloys.* Oxidation of Metals, 1997. **47**(5/6): p. 381-410.
232. Bennett, R.J., et al., *On the oxidation behavior of titanium within coated nickel-based superalloys.* Acta Materialia, 2015. **92**: p. 278-289.
233. Harris, K.E., Ebrahimi, F., and Garmestani, H., *Texture evolution in NiAl.* Materials Science and Engineering A, 1998. **247**(1-2): p. 187-194.